UC Riverside

UC Riverside Electronic Theses and Dissertations

Title

Low Energy Alkali Ion Scattering From Au Nanoclusters on Oxide Substrates

Permalink

https://escholarship.org/uc/item/2q9927s1

Author

Salvo, Christopher

Publication Date

2018

Copyright Information

Peer reviewed|Thesis/dissertation

UNIVERSITY OF CALIFORNIA
RIVERSIDE

Low Energy Alkali Ion Scattering From Au Nanoclusters on Oxide Substrates

A Dissertation submitted in partial satisfaction
of the requirements for the degree of

Doctor of Philosophy

in

Physics

by

Christopher Ross Salvo

June 2018

Dissertation Committee:
    Dr. Jory A. Yarmoff, Chairperson
    Dr. Shan-Wen Tsai
    Dr. Jing Shi

The Dissertation of Christopher Ross Salvo is approved by:

_____

_____

_____
<div align="right">Committee Chairperson</div>

University of California, Riverside

Acknowledgments

To my wife Brittany, you have been here for me through it all. I am eternally grateful for you. You are truly a special person in this world and I am so fortunate to know you and call you my wife. Your patients, kindness, and love have made it easier for me to do class work, research, and writing as I have pursued and obtained this doctoral degree. Thank you for believing in me even when I did not believe in myself.

To my daughter Emilia, I have spent a lot of time and effort realizing an old saying is true. You can do anything you put your mind to. I hope you always trust and know that. Thank you for being an inspiration of possibility and brilliance for me.

I greatly appreciate my parents, Faith and Frank Salvo, for all their wonderful wishes for my life and unconditional love and support. I will always remember the encouragement and support they gave me throughout my schooling.

I also want to acknowledge the people that were in the trenches with me starting with the person I turned to the most, Haoshan Zhu. As well as Josiah Keagy, Bradley Erwin, Joshua Raimist, Dr. Weimin Zhu, Dr. Tianbai Li, and Dr. Alex Arjad. On top of this were my fellow graduate students who supported me both through my classes and morally, Dr. Blake Pollard, Robert Schafer, Adrian Nosek, Petr Stepanov, Maxwell Grossnickle, Sean Nelson, Dr. Mostafa Khezri, Dr. Michael Beaumier, Dr. Andrew DeGroot, Dr. Alexander Natale, Dr. Oleg Martynov, and more. In addition, special thanks are given to a good friend, David Fox for his help with graphics.

I appreciate the professors who have taken the time to instruct me in the practice of theoretical physics, Dr. Vivek Aji, Dr. Kirill Shtengel, Dr. Shan-Wen Tsai, Dr. Ernest

ABSTRACT OF THE DISSERTATION

Low Energy Alkali Ion Scattering From Au Nanoclusters on Oxide Substrates

by

Christopher Ross Salvo

Doctor of Philosophy, Graduate Program in Physics
University of California, Riverside June 2018
Dr. Jory A. Yarmoff, Chairperson

Surface science techniques are used to probe Au nanoclusters in an attempt to understand fundamental properties that are related to their unusually high catalytic activity. The main technique used is the neutralization probability of low energy alkali ion scattering. This is performed on Au nanoclusters supported on either $TiO_2(110)$ or SiO_2.

Au Nanoclusters are deposited onto $TiO_2(110)$ via buffer layer assisted growth in ultra-high vacuum, which is a novel process to grow clusters. A thin amorphous solid water buffer layer is condensed onto a $TiO_2(110)$ single crystal cooled to 100 K. Au atoms deposited onto this layer arrange themselves into nanoclusters. The sample is then annealed to 320 K to desorb the ASW and enable the clusters to soft-land onto the substrate. Time-of-flight low energy ion scattering, using Li^+, Na^+ and K^+ projectiles, probes the materials during each step of the procedure to measure the surface composition and reveal the details of how the clusters form. The neutralization probability of Na^+ ions singly scattered from the Au nanoclusters indicates that they increase in size after annealing and that the magnitude of the increase is a function of the

buffer layer thickness. The adsorption of a thin, incomplete water layer prior to Au deposition forms nanoclusters that are possibly even smaller than those produced by direct deposition onto the clean substrate.

The neutralization of low energy Na^+ and Li^+ ions scattered from Au nanoclusters formed by deposition onto oxide surfaces decreases as the cluster size increases. An explanation for this behavior is provided, which is based on the notion that the atoms in the clusters are not uniformly charged, but that the edge atoms are positively charged while the center atoms are nearly neutral, as reported in the literature. This leads to upward pointing dipoles at the edge atoms that increase the neutralization probability of alkali ions scattered from those atoms. As the clusters increase in size, the number of edge atoms relative to the number of center atoms decreases, so that that the average neutralization also decreases. Calculations employing this model are compared to experimental data and indicate good agreement if the strength of the dipoles at the edge atoms are assumed to decrease with cluster size. This model also explains differences in the neutralization probabilities of scattered Na^+ and Li^+.

Catalytically active Au nanoclusters on SiO_2 are exposed to Br_2 and then measured using 1.5 keV Na^+ low energy ion scattering. It is found that Br_2 adsorbs on the nanoclusters, but not on the substrate nor on bulk Au. These results show that the clusters are able to dissociate the Br_2 and then adsorb the individual Br atoms. Results from the literature indicate that the catalytic activity of nanoclusters occurs at the edges and the work from this dissertation confirms that the edge atoms are positively charged. This leads to the conclusion that the outer shells of the

electronegative Br atoms become filled so that they ionically bond to the edge atoms of the clusters. Furthermore, Br_2 is a known catalytic poison and this work shows how its adsorption blocks sites that would otherwise be involved in a surface chemical reaction.

Contents

Figures

Table

[1] X. Lai, T.P.S. Clair, M. Valden, D.W. Goodman, Prog. Surf. Sci., **59** (1998) 25-52.

Chapter 1 Introduction

1.1   Surface Science

Surfaces are of scientific interest due to the different environment that surface atoms experience as compared to those in the bulk [1]. This leads to particular atomic structures and electronic states that only exist at the surface. At the beginning of fundamental surface science research, the most important discoveries involved relaxation, reconstruction, and surface states of single crystal materials. Relaxation and reconstruction are structural changes that occur for many surfaces due to the abrupt ending of the periodic crystal. Relaxation is a movement of the surface atoms from their bulk positions in a direction perpendicular to the surface plane, and it occurs generally with metal surfaces. Reconstructions are a change of the crystal structure at a surface that involves movement parallel to the surface plane and is more prevalent with semiconducting materials. One of the most important examples is Si(111), which has a reconstruction that produces a two-dimensional unit cell that is 7x7 times larger than the bulk unit cell [2]. Surface states are electronic states found on surfaces that do not exist in the bulk. For example, this occurs for topological insulator materials in which the surface is electrically conductive through two-dimensional surface states while the bulk material is an insulator [3].

A large driving force behind the field of surface science is technological applications. Electronic materials and catalysis are two huge areas that rely on surface properties. Catalysis has applications in environmental remediation using photocatalysts [4] or supported metal nanoclusters [5]. Areas of importance to electronic materials

include etching, deposition and plasma processing in semiconductor device manufacture. Tribology, colloquially known as lubrication, has technological impact in many areas including space vessels and nanomechanical devices. Battery research is an area where lots of charge must be stored at a relatively high potential while taking up the smallest volume possible. One way to store charge is on the surface and there is a large surface area contained in a relatively small volume for nano-sized transition-metal oxides [6].

It was with the award of the Nobel Prize in chemistry in 1932 to Irving Langmuir for his studies in surface chemistry that surface science was initially acknowledged on a grand stage. Langmuir may even be referred to as the father of surface science. In addition, Gerhard Ertl was awarded the Nobel Prize in Chemistry in 2007 for his studies of chemical processes on solid surfaces.

Studies of surfaces differ from those of bulk materials largely because of the difference in number of atoms at a surface. For laboratory experiments investigating the bulk, there are commonly on the order of 10^{23} particles available, whereas roughly only 10^{15} particles are present in a square centimeter of a surface, thereby requiring that surface techniques be highly precise.

Surface science experiments are most often conducted in ultra-high vacuum (UHV) since the production of surfaces without contamination is vital. To keep surfaces free from contamination caused by molecular adsorption of background gasses, a vacuum of roughly 1×10^{-10} Torr is needed. At this pressure, it takes about 10^4 seconds (2.75 hours) for each surface atom to interact with one gas molecule. Specialized techniques have been developed, however, to monitor surfaces near atmospheric pressure, such as

ambient pressure x-ray photoelectron spectroscopy (XPS) [7], which is useful for directly monitoring surface chemical reactions that are important in areas such as catalysis and environmental science.

When a sample is placed in an UHV chamber, it needs to be cleaned *in situ* to remove oxidation, water, hydrocarbons, and other contaminants to produce the natural surface structure. A common method to remove impurities is ion bombardment, also known as sputtering [8]. Inert noble gas atoms are ionized, accelerated to 500-1000 eV and targeted at the sample, which removes atoms from the surface through kinematic interactions. This technique has the side effects of disordering the near-surface region and imbedding some of the inert atoms in the sample. To restore the crystallinity of the surface, it is usually heated for a fixed time in UHV at a temperature that allows the atoms to move into their lowest energy configuration, which is referred to as annealing, which simultaneously desorbs the embedded insert atoms into the gas phase.

Surface sensitive experimental techniques began to be developed during Langmuir's time and have continued through today. These techniques allow for the elemental composition of surfaces to be ascertained, surface atomic structures to be determined, adsorbate-bonding strengths to be identified, and the general comprehension of what occurs at the surfaces of materials to be understood at the atomic level. In general, multiple techniques must be applied to a given system to generate such a full understanding.

Most of these surface spectroscopies are indirect as they involve scattering of various particles from the surfaces, with an analysis of the data used to infer information

about the surface. A few such surface science techniques are low energy ion scattering (LEIS) which provides the elemental composition of the first few layers of the sample and can be used for surface structure analysis [9]. Auger electron spectroscopy (AES) provides elemental information of roughly the first 5-10 layers [10]. XPS gives chemical bonding information as well as elemental composition with a similar depth sensitivity [11]. Low energy electron diffraction (LEED) shows the symmetry of the two-dimensional crystal structure of the surface in reciprocal space [12]. Temperature programmed desorption (TPD) provides adsorbate binding strengths and the products of surface chemical reactions [13]. Electron stimulated desorption (ESD) gives information about the binding strength of adsorbates and can also determine the bond direction [14]. Vacuum is needed to conduct most of these spectroscopies, as they involve the collection of neutral or charged particles that would collide with atmospheric gasses.

A huge advance in surface science occurred when scanning tunneling microscopy (STM) came to fruition. In STM, electrons quantum mechanically tunnel between the surface and a very sharp tip over distances shorter than the atomic spacings. The number of electrons that tunnel, i.e., the tunneling current, is related to the distance of the tip from electronic states in the surface. This makes it possible to produce three-dimensional images of surfaces on the atomic scale by scanning the tip across the surface while keeping the tunneling current constant. The images provide the density of filled or empty electronic states, which follow the atomic structure in many cases. STM was developed by Binnig and Rohrer [15], for which they were awarded the Nobel Prize in Physics in 1986. This technique made the field of surface science more popular because it

effectively makes atoms visible, which directly plays into the human mentality of "seeing is believing". STM and other scanning probe microscopies [16, 17] are fundamentally distinct from scattering methods, and are an important class of experimental tools used to investigate surfaces.

1.2 Au Nanoclusters

Au nanoclusters supported on oxides have been known to be active catalysts for roughly the last 30 years [18]. They were initially observed to behave as catalysts by Haruta in an exploration for a means to oxidize H_2 [18]. Au clusters ranging from a few to 1000s of atoms supported on oxide substrates catalyze reactions such as water splitting and CO oxidation with high activity [19-21]. Au nanoclusters on an oxide substrate have been reported to have catalytic rates that rival those of enzymes [22], contrary to the inert nature of bulk Au which does not easily oxidize and can maintain a shiny appearance in atmosphere.

Because of the many imaginable applications of Au nanoclusters, a large amount of scientific research has ensued. Many variations of the original Au cluster-oxide system, for example Ag, Pt, Ir, Ru, and Rb supported on oxides such as TiO_2, SiO_2, MgO, and Al_2O_3, also exhibit catalytic activity [5, 22-24]. It has also been found that bimetallic clusters [25-27], metals on a substrate other than an oxide, such as graphene [28-30], and swapping the materials by growing oxide clusters on a metal substrate [31] can work as nanocatalysts. In addition, DNA can bond to Au nanoclusters for gene regulation [32],

Au nanoclusters can be used to detect dopamine in fluids [33], and nanoclusters have applications in optoelectronics and chemical sensors [34, 35].

There are many ways to prepare nanoclusters. They can be grown by physical vapor deposition (PVD) [36, 37], chemical vapor deposition (CVD) [38], size selected deposition from molecular beams [39], buffer layer assisted growth (BLAG) [40], through chemical synthesis [20, 38, 41, 42], lithography [43] or other methods. Chemical synthesis is performed in solution without a vacuum, lithography can be performed in a clean room, whereas the other methods require UHV.

The surface science tools commonly used for catalysis studies are well applied to nanoclusters, and there has been a vast array of techniques used to study nanoclusters. For example, XPS was used to learn about the binding of Ag nanoclusters to a CeO_2 substrate [44]. AES measured the thickness of Au deposited on TiO_2 [45]. LEIS determined the growth mode of Au on TiO_2 [37]. TPD found that the binding strength of O on Au nanoclusters is stronger for smaller clusters [46]. Fourier-transform infrared spectroscopy (FTIR) found that the reason Cl poisons Pt nanoclusters is because it blocks the sites where the catalysis reactions would occur [47]. STM observed the average diameter of Au nanoclusters as a function of Au deposition [36, 48]. Atomic force microscopy (AFM) monitored the shapes of clusters when depositing multiple metals with different stoichiometries [49]. Aberration corrected-high resolution transmission electron microscopy (AC-HRTEM) made a measurement of the atomic structure of colloidal Au nanoclusters deposited on amorphous carbon. The image is taken before and after heating, finding that initially the same crystal structure exists in a cluster but with

6

multiple mirror planes and then after heating to 600° C it forms a (111) structure, however there is a lack of information as to which layer of the nanocluster is being observed [50]. Effectively the importance of this measurement is to monitor the edge of the cluster and not the center atoms, making a connection between the deactivation of nanoclusters when the cluster has been heated and a reduction in under coordinated atoms. Scanning electron microscopy (SEM) observed Au nanocluster size and placement when grown with electron beam lithography [43]. Density functional theory (DFT) determined the charge state of each atom in a Au nanocluster supported on TiO_2 [51]. Many of the techniques applied to the study of nanoclusters can be found in review articles [22, 23, 52, 53]. Overall, many different surface science techniques have been applied to nanoclusters, and they form a body of work that together generates an understanding of what is occurring at the atomic level.

Despite all the research done to this point, however, the reason that small clusters are such efficient catalysts is not yet completely understood, although there have been many characteristics of the system that have been shown to influence the activity. The main characteristics discussed in the literature are quantum-size effects, substrate effects, low coordinated atoms, size and shape, and charge state [5, 54]. Some of these properties are correlated, such as quantum-size effects and the actual size of the cluster.

Since the clusters are so small compared to bulk materials, their electrons do not create continuous bands, but instead form discrete levels that depend on the cluster size, which is referred to as a quantum size effect [55]. Scanning tunneling spectroscopy (STS) observed a band gap for specific cluster sizes and that the highest catalytic activity is

correlated with the presence of this band gap [56]. The band gap was interpreted to be an indicator of the presence of discrete levels and it was therefore concluded that the filled quantum levels are largely responsible for the catalytic activity of the nanoclusters and causes them to be negatively charged [56]. It was later found through infrared reflection adsorption spectroscopy, TPD [57, 58], and DFT [59] that these quantized levels are present for both small and large nanoclusters and, since the large nanoclusters are not nearly as catalytically active as the small clusters, this quantum size effect is likely unrelated to the catalytic activity.

An optimal cluster diameter of 3.2 nm produces the highest catalytic activity for CO oxidation for Au nanoclusters supported on $TiO_2(110)$, thus indicating the importance of the size of the nanocluster [60]. It was later shown that Pd nanoclusters supported on SiO_2 also oxidize CO, but optimization of the oxidation performance was correlated with facets of the nanocluster [61]. Although it was not specifically reported, this could be related to the low coordination of the edge atoms.

The field is coming to a consensus that the catalytic reactions occur at the edges of the clusters, which is where the lowest coordinated atoms are located [50, 51, 62-64]. A confirmation of this idea involved monitoring the deactivation of nanoclusters with electron microscopy after they are annealed to remove the low coordination sites [50]. There are also theoretical papers that point to the catalytic activity occurring at edges of the nanocluster [51, 62]. It has also been reported using XPS that there is a synergetic effect between the substrate and the nanoclusters that is responsible for the activity, implying that the substrate is involved in the reaction at the edge of the nanocluster [63].

The charge of the nanocluster may also be related to the high catalytic activity of the nanoclusters. Although reports of negatively charged clusters dominated early nanocluster research [56, 65-68], it is becoming more agreed upon that they are positively charged, or at least contain positively charged atoms [51, 69-73]. Multiple DFT studies identify catalytic sites at the edge of the nanocluster and calculate that the edge atoms are positively charged, whereas the center atoms are near neutral [51, 74]. In addition, a calculation shows that positively charged individual Au atoms on TiO_2 are catalytically active for CO oxidation [62], which agrees with the findings of an experimental paper that showed that single Au atoms on TiO_2 are positively charged [70]. These findings imply that the charge of the edge atoms may be related to the catalytic activity [51].

Despite all the research conducted to date, there still exists a need for consistent experimental and theoretical work to provide a full understanding of the catalytic mechanism for oxide supported metal nanoclusters. For example, the relationship between the charge of the nanocluster and the catalytic activity and how changing the substrate changes the catalytic performance of the clusters are still open questions.

1.3   Electron Spectroscopy

Electron spectroscopies are some of the most powerful surface analysis tools for a number of reasons. Low energy electrons (~10-3000 eV) only travel short distances in a material so that those that escape to be measured have emanated from the near-surface region [11]. The kinetic energy of emitted electrons can provide information about the

electronic states and chemical composition of a surface. Diffraction of electrons can be used to obtain information about the crystallinity and atomic structure of the surface [75].

As electrons travel through a material, there is a probability that they will have an inelastic collision and lose some of their energy [76]. The average distance that an electron travels in a solid material without suffering an inelastic collision is known as the inelastic mean free path (IMFP), λ. The IMFP is plotted as a function of the electron kinetic energy in Fig. 1.1, which shows a minimum at around 40 eV, corresponding to an IMFP of ~0.5 nm. The shape of the curve is similar for most materials, but the actual values can vary with material.

The plotted equation is:
$$\lambda = \frac{143}{E^2} + 0.054 \cdot \sqrt{E}$$
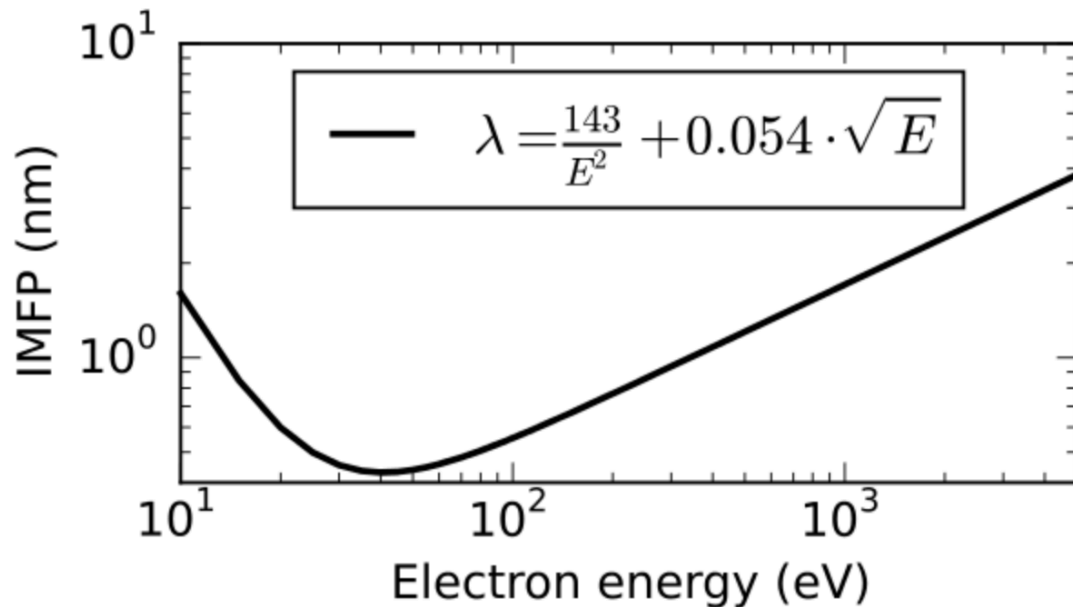
Figure 1.1 Inelastic mean free path (IMFP) of electrons traveling in a solid as a function of their kinetic energy [14].

The probability that an electron suffers an inelastic collision is dependent exponentially on the distance traveled through the solid. The following equation is used

to determine the probability that an electron travels a distance d through a material and escapes without losing any energy due to inelastic collisions

$$I(d) = I_0 e^{-d/\lambda(E)} \qquad (1.1)$$

where I is the final intensity of electrons and I_0 is the initial electron intensity. For electron spectroscopy in surface science, this equation is commonly used to find the probability that an electron will escape from a material without any loss of energy. To get an idea of how surface sensitive electrons with roughly 40 eV of energy are, the distance d that an electron will travel with a 1% probability of not having an inelastic loss is about 2.6 nm. In comparison, a 1000 eV electron traveling through the same material will travel an average distance of about 10 nm. Thus, this effect allows the majority of the observed electrons to emanate from the surface region of a material.

There are many types of electron spectroscopies; only the ones used in this dissertation are introduced here.

1.3.1 X-ray Photoelectron Spectroscopy

X-ray photoelectron spectroscopy (XPS) [11] is arguably the most powerful and widely used electron spectroscopy technique. In 1981, Kai Siegbahn was awarded the Nobel Prize in Physics for developing x-ray photoelectron spectroscopy (XPS), which has also been referred to as electron spectroscopy for chemical analysis (ESCA). X-ray photons are incident on the sample, causing electrons to be ejected by the photoelectric effect. Core-level XPS is the most common type of XPS, which involves measuring the

electrons emitted from inner shell electronic states. These electrons have a kinetic energy (*KE*) of

$$KE = h\nu - BE - \phi, \tag{1.2}$$

where *BE* is binding energy of the electron, *hv* is the photon energy, and ϕ is the work function. The binding energy is the energy needed to excite the bound electron to the Fermi energy. Each element has a unique set of inner shell electrons with binding energies that allow XPS spectra to provide an elemental distribution of the sample.

One powerful aspect of this technique is being able to observe a difference in the binding energy of any particular core level, which is directly related to the chemical environment of the atom(s). A classic example is the Si 2p peak. Pure Si has a 2p binding energy of 99.15 eV, while for SiO_2 it is 103.4 eV [11]. In general, an electronegative atom attached to a metal atom shifts the binding energy up because it removes charge surrounding that atom thus causing the core electrons to be more strongly bound. Thus, a higher binding energy occurs when an oxide layer is formed.

The experimental setup for XPS involves an x-ray source and an electron energy analyzer. The three most common methods for x-ray generation are standard sources, monochromatic sources, and synchrotron radiation [11]. Standard sources are most commonly used as they are on the size scale of most other UHV equipment. They produce x-ray radiation by bombarding electrons into an anode with a specific metal coated on it. Monochromatic sources use a standard source but have an x-ray monochromator that filters out unwanted photon energies to produce a sharper, monochromatic x-ray beam. Synchrotrons are large scale particle accelerators that radiate

x-rays. These have the highest intensity of photons and the ability to adjust photon energy.

To observe the electrons emitted from a sample after x-ray bombardment as a function of energy, either a cylindrical mirror analyzer (CMA) or a hemispherical electrostatic analyzer (ESA) are commonly used [11]. Both analyzers create a potential difference across the components in the analyzer that allow only a narrow range of energies through to the electron multiplier detector, while particles with different energies are deflected away. Figure 1.2 is a schematic diagram of a CMA where the curved dashed lines represent the path that charged particles with a narrow range of energies will follow from the sample (S) to the focus point (F) where the detector is located. This enables a spectrum of the number of photoelectrons as a function of energy to be collected by ramping the voltage on the elements in the CMA [76]. Similarly, in Fig. 1.3 there is a schematic diagram of a hemispherical ESA where the curved lines with arrows represent the direction that charged particles of a narrow energy range will take from the entrance of the analyzer to the detector, with that energy being dependent on the voltage difference between the inner and outer hemispheres [76].
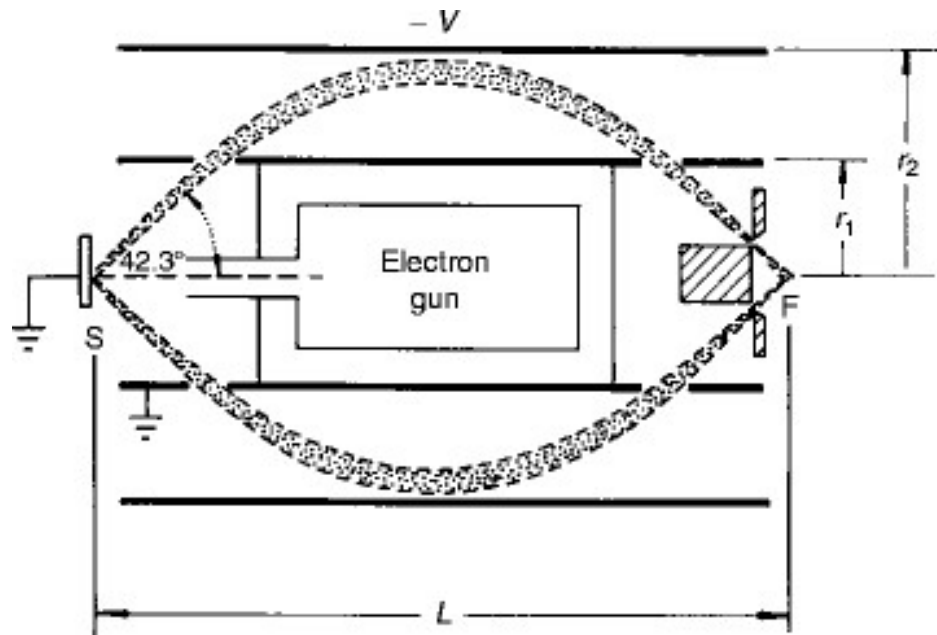
Figure 1.2 The CMA is composed of two coaxial cylinders, one within the other, with a voltage difference across them as indicated. Note that the indicated electron gun is not needed for XPS but will be discussed in section 1.2.2. The figure is a two-dimensional cross section along an axis of symmetry.
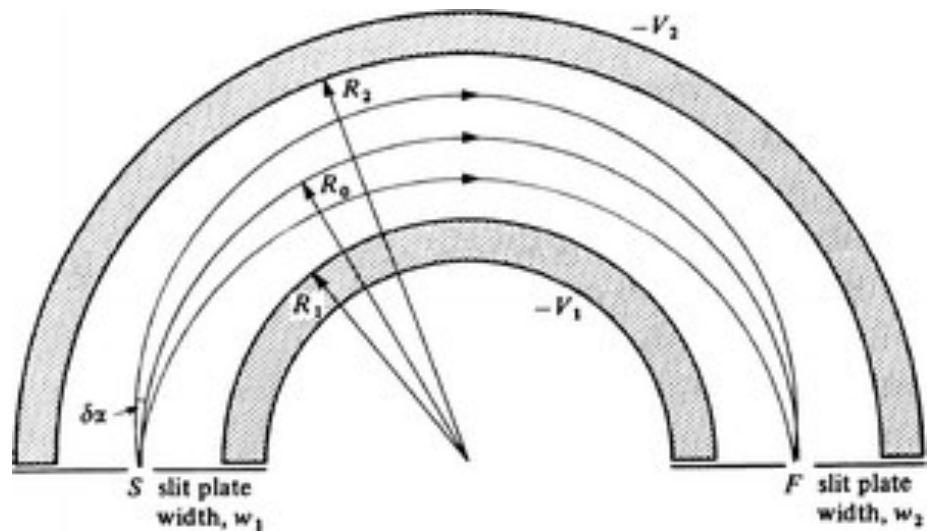
Figure 1.3 The hemispherical analyzer is composed of two half spheres, one within the other, with a difference of voltage across them as indicated. The figure is a two-dimensional cross section along an axis of symmetry.

14

1.3.2 Auger Electron Spectroscopy

Another technique used to identify the elemental composition of a sample's surface is Auger electron spectroscopy (AES) [77-81]. The Auger process involves 4 electrons: The incoming electron that induces the ejection of a second electron, the valence electron that fills the hole, and the Auger electron that is ejected from the valence band and measured. The incoming electron typically has a kinetic energy of 3-5 keV, which can directly or indirectly induce the removal of a core electron. Once there is a vacancy in a core orbital, an electron from a valence shell decays to fill that orbital. Due to conservation of energy, the difference in energy between the valence and core level must be accounted for by emission of either a photon or an Auger electron. The Auger electron will have a kinetic energy equal to the difference in valence and core electrons minus the ionization energy. It should be noted that Auger electrons can also show up in XPS spectra.

Similar to XPS, Auger is surface sensitive and can identify elemental composition at the surface. The surface sensitivity of the technique again arises from the small IMFP of low energy electrons, as shown Fig. 1.1 and used in equation (1.1). The elemental composition is obtained because each element has a unique set of core level electrons that lead to a unique set of Auger lines.

The experimental setup for AES commonly uses a CMA with a coaxial electron gun leading to normal incidence of the electron beam, as indicated in Fig. 1.2, but AES can be performed with an ESA, as well. In addition, the electron beam can be incident onto the sample at a grazing angle to provide improved surface sensitivity. The AES

15

setup allows for electrons to be incident on the sample and for the number of electrons emitted from the sample to be measured as a function of their kinetic energy. The detected signal of Auger electrons is not large, however, due to a background of secondary electrons. To make the AES peaks easier to observe above the background, the signal is often differentiated electronically by using a sine wave generator on the analyzer and a lock-in amplifier to collect the derivative of the current of scattered electrons. Thus, AES spectra normally display the derivative of the signal and the vertical axis of an AES spectrum has units of dN/dE.

1.3.3   Low Energy Electron Diffraction

All solid materials fall into three categories: Single-crystalline, poly-crystalline, or amorphous [82]. Crystals show up in nature as a lowest energy state for the arrangement of a large number of atoms (on the scale of 10^{23}). There are 14 possible arrangements in 3 dimensions, which are referred to as the Bravais lattices. Poly-crystalline materials simply have multiple crystallites oriented in random directions within the sample. Amorphous materials have no repeating pattern in their structure.

In the case of single crystals, a uniform structure is created that can be labeled by Miller indices that indicate directions with respect to the lattice [82]. The surfaces of single crystals are notated by the Miller index of the surface normal, followed by notation that specifies the symmetry of the surface reconstruction, if any exists. If the crystal has cubic symmetry, then the (100) face will be square, the (110) will be rectangular, and the (111) face will be have three-fold symmetry.

LEED can be used to observe the symmetry of crystalline surfaces in UHV [75]. The physics behind this technique comes from the wave nature of electrons, as given by

$$\lambda = \frac{h}{mv} \tag{1.3}$$

where λ is the wavelength, h is Planck's constant, m is the mass of the particle, and v is its velocity. For electrons, the wavelength as a function of energy (E, given in eV) is

$$\lambda = \sqrt{\frac{150 \text{Å}^2 eV}{E}}. \tag{1.4}$$

For 100 eV electrons, the wavelength is 1.2 Å, which corresponds roughly to the atomic spacings in most materials. This allows scattered electrons to interfere with each other and create spatial electron diffraction coherencies. Similar to the other electron spectroscopies, the IMFP limits the electrons to those that emanate from the near-surface region to exit the material and be observed.

The experimental set up involves an electron gun and some sort of electron-fluorescent screen or imaging detector that is large enough to capture the spatial electron coherencies. Because this is a diffraction technique, LEED patterns consist of spots at certain angles in reciprocal space. A LEED pattern can be visually analyzed to obtain the symmetry and orientation of the crystal surface. In addition, quantitative measurements of the spot intensity vs. electron energy, called LEED I-V curves, can be used to quantitatively obtain the detailed surface atomic structure to high accuracy by comparison to calculations for particular structures [75].

1.4   Ion Scattering Spectroscopy

There are three main types of ion scattering spectroscopies in which ions scatter from a target and their kinetic energy and/or angular distribution is measured. These types of ion spectroscopies are categorized by the kinetic energy of the incoming particle into the low (LEIS) [83], medium [84] and high [85] energy regimes. Low energy is roughly defined to be in the ~1 keV range, medium energy is in the ~10-100 keV range and high energy is ~1 MeV. Rutherford backscattering spectroscopy (RBS) is also conducted with use of high-energy ion beams [85]. A further description of low energy alkali ion scattering is provided below, as that is the particular technique used in this dissertation.

When a projectile is incident onto a sample, there are a few possible outcomes [9]. The primary one of interest for LEIS is when the projectile elastically scatters from a single surface atom. During the scattering process, the surface atom with which it collides will recoil, sometimes leaving the sample, therefore disturbing the surface. For this reason, ion scattering is a destructive process. It is also possible that the projectile undergo multiple collisions with atoms in the solid and either scatter or embed itself in the material. The scattered projectile can also exchange charge with the surface and become neutralized or form a negative ion during the scattering event. The scattering process can also induce excitations in the sample that lead to electron or photon emission.

1.4.1 Binary Collision Approximation

The projectile in LEIS is assumed to interact with only one target atom at a time, which is referred to as the binary collision approximation (BCA) [9]. In addition, these interactions are primarily elastic which allows for the use of classic mechanics to treat each individual collision. Conservation of energy and momentum is used to derive the following equation that indicates the kinetic of a projectile after scattering from a given target atom,

$$E_1 = E_0 \left[\frac{\cos\theta \pm \sqrt{(m_t/m_p)^2 - \sin^2\theta}}{1 + m_t/m_p} \right]^2 \tag{1.5}$$

where E_0 is the initial energy of the projectile, E_1 is the final energy of the projectile, m_p is the mass of the projectile, m_t is the mass of the target, and θ is the scattering angle. A more in-depth derivation of this equation and more information related to ion scattering can be found in Gann's dissertation [86].

When a projectile undergoes just one collision and is then detected, it is referred to as single scattering, which generates a single scattering peak (SSP) in the energy spectrum. Since the energy of the scattered particle is a function of the ratio of the target to the projectile mass, the elemental composition of the surface can be determined from analysis of the SSPs in a LEIS energy spectrum.

A projectile can also undergo a series of scattering events and then escape the sample and be detected. There are many such scenarios that can take place which causes multiply scattered particles to have a wide range of energies. In addition, inelastic interactions, such as plasmon excitation, reduce the final energy of the scattered particles

[83], but those are typically on the order of 100-200 eV and can be ignored for many analyses.

Low energy ion scattering (LEIS) is an extremely surface sensitive technique that probes the top few layers of the surface, the specifics of which depend on the surface structure of the material and geometry of the ion scattering setup. The reason that ions only interact with the top layer(s) is because of shadowing and blocking [87]. Shadowing occurs when the upper few layer atoms are physically in the way of the projectile reaching deeper layers, analogous to objects creating shadows in light. Blocking occurs when a projectile backscatters from an atom below the outermost surface layer and then interacts with an atom closer to the surface, thereby being unable to reach the detector. Because of shadowing and blocking, a detailed analysis of the angular distribution of scattered ions can be used to determine the surface atomic structure [88].

1.4.2 Ion Neutralization

There are two primary mechanism responsible for ion neutralization during LEIS, Auger neutralization (AN) and resonant charge transfer (RCT). Auger neutralization occurs with projectiles that have a large ionization potential which lies below the surface conduction band, such as noble gas ions [10]. AN is a generally irreversible process that leads to extreme surface sensitivity when using a charged particle analyzer. In contrast, RCT occurs for elements with low ionization potentials (such as alkalis or halogens). Since alkali ions are used throughout this dissertation, a further explanation of RCT is provided.

20

Figure 1.4 is used to graphically describe what occurs electronically when a low energy alkali ion scatters from a metal. The horizontal axis is the distance from the surface and the vertical axis is energy. The metal target has a work function ϕ defined as the amount of energy needed to excite an electron from the top of the Fermi level to the vacuum level.

When the projectile is far from the sample, its ionization energy is below the Fermi level of most metals and the vacant *s* level is sharp, as indicated in Fig. 1.4. As the projectile approaches the sample, its *s* level shifts up in energy because it sees its image charge and broadens due to hybridization with other levels in the surface, bringing it into resonance with bands in the metal [89].

As shown in Fig. 1.4, when an alkali projectile is sufficiently close to the metal surface, electrons will quantum mechanically tunnel between the vacant ionization level and the surface bands. The scattering event occurs on a shorter time scale than the tunneling of the electrons, causing the neutralization process to be non-adiabatic. This means an equilibrium state of the level is not reached during the scattering process so that the charge distribution of the scattered projectiles is frozen in close to the surface. If the process were to occur adiabatically, which would be in the limit of low velocity, equilibrium would be maintained along the entire trajectory and the level would be 100% filled after scattering. Note that for medium and high energy ion scattering, the velocity is so fast that no charge is exchanged and the scattered particles retain their initial charge state.

The freezing distance is considered to be the point at which the overlap of the filled states and the broadened and shifted ionization level match what is measured experimentally as the neutral fraction (NF). The probability that tunneling occurs is, however, actually a decaying exponential function of the distance between the projectile and the target [90], so that there is not really a fixed freezing distance. Thus, from a very simple point of view, the effective freezing distance can be considered the distance of the projectile above the scattering site at which the electrons can no longer tunnel. Since the charge transfer is non-adiabatic, the charge state is frozen in along the exit trajectory at this point. This distance is commonly on the scale of a few Angstroms and is graphically represented in Fig. 1.4 as the distance between the black curve and the surface of the metal. Once electrons begin to tunnel in and out of the level, memory of the previous charge state of the projectile is lost [91]. Thus, incoming neutral atoms or ions will have the same charge distribution after scattering. Further details of these quantum mechanical interactions are provided in the calculations of Brako and Newns as well as those of Nordlander and Tully [90, 92].
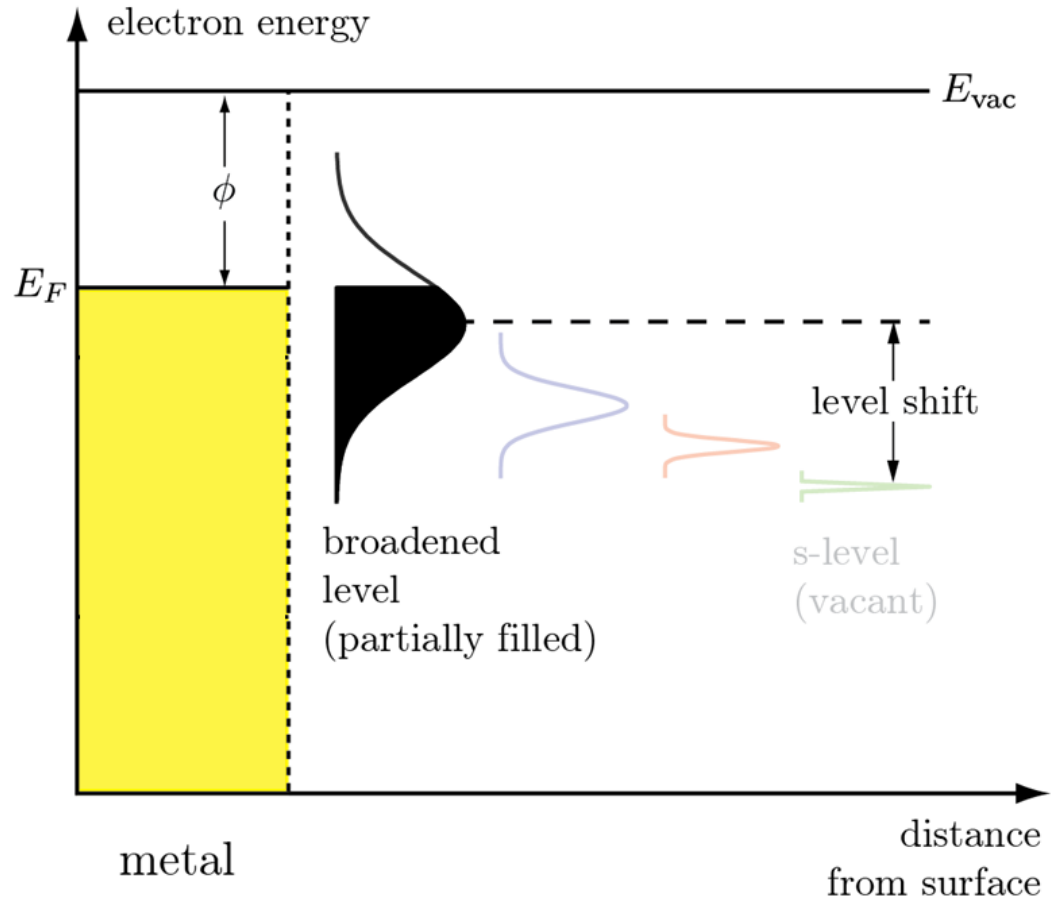
Figure 1.4 RCT model represented graphically.

Figure 1.4 shows that the NF depends directly on the ϕ at the freezing distance. If the ϕ gets larger, then the NF goes down and vice versa. The local electrostatic potential (LEP) at the freezing distance above the scattering site, which is sometimes referred to as the local work function, is what actually determines the NF when the potential is inhomogeneous.

1.4.3 LEIS Experimental Setup

To collect charged and neutral particles with equal sensitivity as a function of energy, a time-of-flight (TOF) setup is used for LEIS. As the name implies, the flight time of the particle is measured, which is related to the energy of the particle.

The ion beam is generated by a thermo-ionic source (Kimball Physics). The ion gun contains two sets of deflection plates perpendicular to each other and a 1 mm diameter aperture in front of the plates. Voltage pulses are applied to the plates to raster the beam in a square pattern. The geometry is such that one side of the square goes through the aperture during each cycle, thereby generating a pulse of ions. This means that in the time it takes the pulser to go from -200 to +200 V (one of the sides of the square), the beam briefly passes across the aperture and ions are emitted. A graphical depiction of this is shown in Liu's dissertation [93]. The pulser is operated between 40 and 80 kHz, providing a period of 25 to 12.5 µs. The pulse width of the ion beam is typically on the order of 50-100 ns.

This pulse width is much smaller than the projectile travel time, so that all the projectiles in a given pulse can be considered as reaching the target at effectively the same time, which is defined as time zero. The recorded flight time of a given particle is arbitrary, however, as the signal from the pulser does not necessarily correlate with the pulse of ions. To determine the actual time zero and produce spectra with accurate flight times, an electron or photon peak in the spectrum can be used or a calculation of the flight time for a given feature can be made if the TOF leg length is known.

After the particles scatter from the sample, they travel down the TOF tube and are detected by a triple microchannel plate (MCP) array, which is an 18 mm diameter electron multiplier, with the entrance grounded. One advantage of these detectors is that they are not sensitive to the charge of the particle, although they are sensitive to the energy of the particle, and begin to lose sensitivity as the scattered energies fall below about 1 keV [94, 95].

The arrival times are histogrammed by a TDC (Stanford). The flight time is measured by sending a start pulse when a particle is detected and a stop pulse from the pulsing electronics that correlates with the next pulse of the ion gun. This is in reverse order to not miss any counts because the TDC creates a "dead" period directly following the flight time measurement of a detected particle. The beam current is low enough and the efficiency of ion scattering is such that a particle is detected roughly once every 10 cycles so that there is sufficient time for the electronics to recover before the next scattered projectile arrives. Note that this causes the raw data to be in units of the period minus the flight time, but the data is always corrected before plotting a TOF spectrum.

A set of deflection plates mounted in the TOF leg are used to differentiate between charged and neutral particles. When both plates are grounded, all of the scattered particles get through and are detected, generating the total yield. By placing a large enough voltage across the plates, however, causes the charged particles to be deflected so that only neutral particles are detected, generating the neutral yield. These plates are switched on and off once per minute while simultaneously collecting total and neutral spectra. This compensates for beam current drifts over long periods of times.

Since single scattering generates a SSP at a kinetic energy as calculated by equation (6). An example is shown in Fig. 1.5 for Na$^+$ scattered from Au nanoclusters at 135°, which displays the SSP for Na scattered from Au along with a small multiple scattering background. In this figure, the number of particles detected are on the y-axis and the energy of those particles is on the x-axis. Although the spectrum is collected as a function of time, the axis is converted into energy using the known the distance that the particle travels through the TOF leg. Although the sample contains three elements, Au, Ti, and O, the backscattering geometry only allows Na to singly scattered from Au to be detected. This is because Na is more massive than Ti or O and thus has insufficient energy to be detected by the MCP after backscattering at this angle [9].
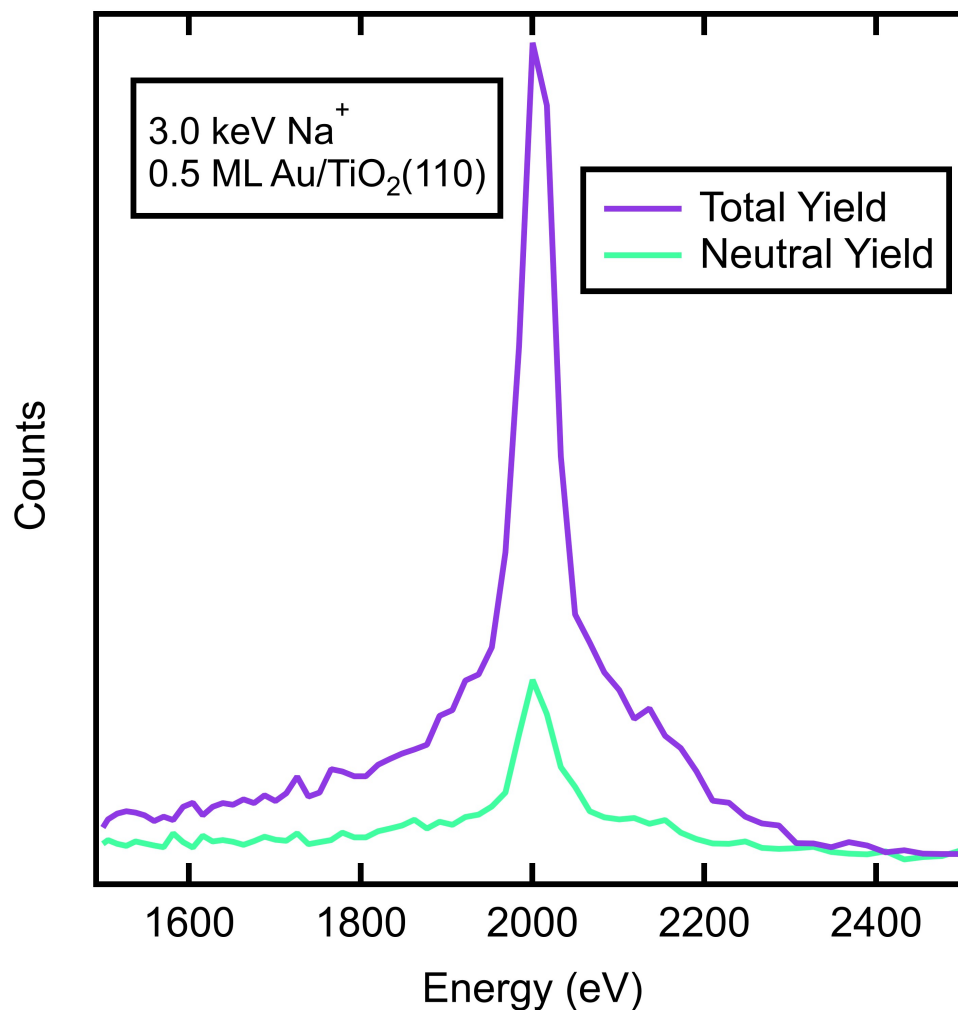
Figure 1.5 A TOF energy spectrum for Na$^+$ scattered from 0.5 ML of Au on TiO$_2$ at a 135° scattering angle.

1.5   Outline of the Dissertation

This original work in the field of nanoclusters attempts to understand the physical properties of Au metal nanoclusters that act as catalysts. This is done using a novel form of LEIS where the charge of the scattered particles is analyzed along with their energies, as explained in section 1.4. From the experimental data, information about the LEP around the nanocluster is determined in a way that other experimental techniques are not

able to provide. For example, scanning probe techniques such as STS and STM do not have the lateral resolution to distinguish between atoms in a cluster. Although differences in the LEP has seen at the center and edge of certain nanostructures using Kelvin probe force microscopy (KPFM) [96], its spatial resolution is even larger than that of STM which limits its ability to probe individual atoms. In addition, these scanning probe techniques do not have the elemental resolution of LEIS.

The work done in this dissertation is fundamental research about the physics of nanoclusters. Thus, no actual chemical activity measurements are performed. The research largely consists of using alkali LEIS spectra and neutralization probabilities to explore various aspects of the nanoclusters. Au nanoclusters are grown by PVD and BLAG on either TiO_2 or SiO_2. The growth mode for all of these systems is Volmer-Webber, which means that the deposited Au spontaneously forms nanoclusters [36].

The neutralization probability of low energy alkali ion scattering is used to probe the deposition of nanoclusters onto a solid surface via buffer layer assisted growth (BLAG) in Chapter 2. A thin amorphous solid water (ASW) buffer layer is grown on a $TiO_2(110)$ single crystal cooled to 100 K. Au atoms deposited onto this layer arrange themselves into nanoclusters. The sample is then annealed to 320 K to desorb the ASW and enable the clusters to soft-land onto the substrate. Time-of-flight LEIS, using Li^+, Na^+ and K^+ projectiles, probes the materials during each step of the BLAG process to measure the surface composition and reveal the details of how the clusters form. The neutralization probability of Na^+ ions singly scattered from the Au nanoclusters indicates that they increase in size after annealing and that the magnitude of the increase is a

28

function of the buffer layer thickness. The adsorption of a thin, incomplete water layer prior to Au deposition forms nanoclusters that are possibly even smaller than those produced by direct deposition onto the clean substrate.

In Chapter 3, an explanation is provided for the decrease in neutralization of low energy Na^+ and Li^+ ions scattered from Au nanoclusters as the cluster size increases. This model is based on the notion that the atoms in the clusters are not uniformly charged, with the edge atoms being positively charged while the center atoms are neutral. This leads to upward pointing dipoles above the edge atoms that increase the neutralization probability of scattered alkali ions from those that scatter from a neutral atom. As the clusters increase in size, the number of edge atoms relative to the number of center atoms decreases, so that that the average neutralization also decreases. Calculations employing this model are compared to experimental data and indicate good agreement if the strength of the dipoles at the edge atoms are assumed to decrease with cluster size. An explanation is also given as to the unexpected neutralization probability of Na^+ compared to Li^+.

In Chapter 4, catalytically active Au nanoclusters on SiO_2 are exposed to Br_2 and then measured using 1.5 keV Na^+ low energy ion scattering. It is found that Br_2 adsorbs on the nanoclusters, but not on the substrate nor on bulk Au. The presence of adsorbed Br reduces the NF of Na scattered from Au. These results show that the clusters are able to dissociate the Br_2 molecules so that they adsorb as individual Br adatoms. With many reports of catalytic reactions occurring at the edges of nanoclusters and the edge atoms being positively charged, this work suggests that the filled shell electronegative Br atom is ionically bonded to the positive edge atoms. Furthermore, Br_2 is a known catalytic

29

poison and this result shows how its adsorption blocks sites and changes the electronic

structure that would otherwise be involved in a surface chemical reaction.

Bibliography

[1] A. Zangwill, *Physics at Surfaces*, Cambridge University Press, Cambridge, 1988.

[2] K. Takayanagi, Y. Tanishiro, M. Takahashi, S. Takahashi, J. Vac. Sci. Technol. A, **3** (1985) 1502.

[3] M.Z. Hasan, C.L. Kane, Rev. Mod. Phys., **82** (2010) 3045-3067.

[4] M.R. Hoffmann, S.T. Martin, W.Y. Choi, D.W. Bahnemann, Chem. Rev., **95** (1995) 69-96.

[5] B. Roldan Cuenya, F. Behafarid, Surf. Sci. Rep., **70** (2015) 135-187.

[6] P. Poizot, S. Laruelle, S. Grugeon, L. Dupont, J.M. Tarascon, Nature, **407** (2000) 496-499.

[7] M. Salmeron, R. Schlögl, Surf. Sci. Rep., **63** (2008) 169-199.

[8] P. Sigmund, Phys. Rev., **184** (1969) 383-416.

[9] W.J. Rabalais, P*rinciples and applications of ion scattering spectrometry : surface chemical and structural analysis*, Wiley, New York, 2003.

[10] H.D. Hagstrum, Phys. Rev., **104** (1956) 672-683.

[11] P. van der Heide, *X-Ray Photoelectron Spectroscopy: An Introduction to Principles and Practices*, Wiley, New Jersey, 2011.

[12] J.J. Lander, J. Morrison, J. Chem. Phys., **37** (1962) 729-&.

[13] R.J. Cvetanović, Y. Amenomiya, Cat. Rev., **6** (1972) 21-48.

[14] M.P. Seah, W.A. Dench, Surf. Interface Anal., **1** (1979) 2-11.

[15] G. Binnig, H. Rohrer, Helvetica Physica Acta, **55** (1982) 726-735.

[16] W. Melitz, J. Shen, A.C. Kummel, S. Lee, Surf. Sci. Rep., **66** (2011) 1-27.

[17] H.-J. Butt, B. Cappella, M. Kappl, Surf. Sci. Rep., **59** (2005) 1-152.

[18] M. Haruta, N. Yamada, T. Kobayashi, S. Iijima, J. Catal., **115** (1989) 301-309.

[19] K. Fukushima, G.H. Takaoka, J. Matsuo, I. Yamada, Jpn. J. Appl. Phys., **36** (1997) 813-818.

[20] M.G. Mendez-Medrano, E. Kowalska, A. Lehoux, A. Herissan, B. Ohtani, S. Rau, C. Colbeau-Justin, J.L. Rodriguez-Lopez, H. Remita, J. Phys. Chem. C, **120** (2016) 25010-25022.

[21] M. Flytzani-Stephanopoulos, Acc. Chem. Res., **47** (2014) 783-792.

[22] A.S.K. Hashmi, G.J. Hutchings, Angew. Chem. Int. Ed., **45** (2006) 7896-7936.

[23] P.L.J. Gunter, J.W. Niemantsverdriet, F.H. Ribeiro, G.A. Somorjai, Cat. Rev., **39** (1997) 77-168.

[24] A.A. Herzing, C.J. Kiely, A.F. Carley, P. Landon, G.J. Hutchings, Science, **321** (2008) 1331-1335.

[25] J. Zhang, L. Wan, L. Liu, Y. Deng, C. Zhong, W. Hu, Nanoscale, **8** (2015) 11.

[26] J.R. Renzas, W. Huang, Y. Zhang, M.E. Grass, D.T. Hoang, S. Alayoglu, D.R. Butcher, F. Tao, Z. Liu, G.A. Somorjai, Phys. Chem. Chem. Phys., **13** (2011) 2556-2562.

[27] E. Gross, M. Asscher, Langmuir, **26** (2010) 16226-16231.

[28] P. Sharma, G. Darabdhara, T.M. Reddy, A. Borah, P. Bezboruah, P. Gogoi, N. Hussain, P. Sengupta, M.R. Das, Catal. Commun., **40** (2013) 139-144.

[29] Z.H. Zhou, F. Gao, D.W. Goodman, Surf. Sci., **604** (2010) L31-L38.

[30] R. Varns, P. Strange, J. Phys.: Condens. Matter, **20** (2008) 225005.

[31] E. Farfan-Arribas, J. Biener, C.M. Friend, R.J. Madix, Surf. Sci., **591** (2005) 1-12.

[32] N.L. Rosi, D.A. Giljohann, C.S. Thaxton, A.K.R. Lytton-Jean, M.S. Han, C.A. Mirkin, Science, **312** (2006) 1027-1030.

[33] S. Govindaraju, S.R. Ankireddy, B. Viswanath, J. Kim, K. Yun, Sci. Rep., **7** (2017) 40298.

[34] F.B. de Mongeot, U. Valbusa, J. Phys.: Condens. Matter, **21** (2009) 224022.

[35] S.A. Geetha, M. Abhishek, V.D. Albert, P.O. Vladimir, A.B. Kris, A.S. Norman, V.M. Rao, Nanotechnology, **23** (2012) 175501.

[36] X. Lai, T.P.S. Clair, M. Valden, D.W. Goodman, Prog. Surf. Sci., **59** (1998) 25-52.

[37] L. Zhang, R. Persaud, T.E. Madey, Phys. Rev. B, **56** (1997) 10549-10557.

[38] S. Schimpf, M. Lucas, C. Mohr, U. Rodemerck, A. Brückner, J. Radnik, H. Hofmeister, P. Claus, Catal. Today, **72** (2002) 63-78.

[39] L. Sungsik, F. Chaoyang, T. Wu, S.L. Anderson, Surf. Sci., **578** (2005) 5-19.

[40] L. Huang, S.J. Chey, J.H. Weaver, Phys. Rev. Lett., **80** (1998) 4095-4098.

[41] J. Radnik, C. Mohr, P. Claus, Phys. Chem. Chem. Phys., **5** (2003) 172-177.

[42] D.G. Duff, A. Baiker, P.P. Edwards, Langmuir, **9** (1993) 2301-2309.

[43] E. Kadossov, S. Cabrini, U. Burghaus, J. Mol. Catal. A: Chem., **321** (2010) 101-109.

[44] D. Kong, G. Wang, Y. Pan, S. Hu, J. Hou, H. Pan, C.T. Campbell, J. Zhu, Phys. Chem. C, **115** (2011) 6715-6725.

[45] Z.M. Liu, M.A. Vannice, Catal. Lett., **43** (1997) 51-54.

[46] V.A. Bondzie, S.C. Parker, C.T. Campbell, Catal. Lett., **63** (1999) 143–151.

[47] F.J. Gracia, J.T. Miller, A.J. Kropf, E.E. Wolf, J. Catal., **209** (2002) 341-354.

[48] D. Eom, C.S. Jiang, H.B. Yu, J. Shi, Q. Niu, P. Ebert, C.K. Shih, Phys. Rev. Lett., **97** (2006).

[49] T.Y. Morante-Catacora, Y. Ishikawa, C.R. Cabrera, J. Electroanal. Chem., **621** (2008) 103-112.

[50] M.J. Walsh, P.L. Gai, E.E. Boyes, J. Phys. Conf. Ser., **371** (2012) 1-4.

[51] L.B. Vilhelmsen, B. Hammer, ACS Catal., **4** (2014) 1626-1631.

[52] B. Roldan Cuenya, F. Behafarid, Surf. Sci. Rep., **70** (2015) 135-187.

[53] F. Cosandey, T.E. Madey, Surf. Rev. Lett., **8** (2001) 73-93.

[54] T. Risse, S. Shaikhutdinov, N. Nilius, M. Sterrer, H.J. Freund, Acc. Chem. Res., **41** (2008) 8.

[55] G.C. Bond, Surf. Sci., **156** (1985) 966-981.

[56] M. Valden, X. Lai, D.W. Goodman, Science, **281** (1998) 1647-1650.

[57] C. Lemire, R. Meyer, S.K. Shaikhutdinov, H.J. Freund, Surf. Sci., **552** (2004) 27-34.

[58] C. Lemire, R. Meyer, S. Shaikhutdinov, H.J. Freund, Angew. Chem. Int. Ed., **43** (2004) 118-121.

[59] J. Kleis, J. Greeley, N.A. Romero, V.A. Morozov, H. Falsig, A.H. Larsen, J. Lu, J.J. Mortensen, M. Dułak, K.S. Thygesen, J.K. Nørskov, K.W. Jacobsen, Catal. Lett., **141** (2011) 1067-1071.

[60] T.V. Choudhary, D.W. Goodman, Topics in Catalysis, **21** (2002) 25-34.

[61] R. Wang, H. He, L.-C. Liu, H.-X. Dai, Z. Zhao, Catal. Sci. Technology, **2** (2012) 575-580.

[62] Y.-G. Wang, D.C. Cantu, M.-S. Lee, J. Li, V.-A. Glezakou, R. Rousseau, J. Am. Chem. Soc., **138** (2016) 10467-10476.

[63] S. Arrii, F. Morfin, A.J. Renouprez, J.L. Rousset, J. Am. Chem. Soc., **126** (2004) 1199-1205.

[64] C. Lemire, R. Meyer, S.K. Shaikhutdinov, H.J. Freund, Surf. Sci., **552** (2004) 27-34.

[65] W. Zhong, D. Zhang, Prog. React. Kinet. Mech., **38** (2013) 86-94.

[66] M. Gao, A. Lyalin, T. Taketsugu, J. Phys. Chem. C, **116** (2012) 9.

[67] X. Yu, L. Xu, W. Zhang, Z. Jiang, J. Zhu, W. Huang, Chin. J. Chem. Phys., **22** (2009) 339-345.

[68] A. Sanchez, S. Abbet, U. Heiz, W.D. Schneider, H. Hakkinen, R.N. Barnett, U. Landman, J. Phys. Chem. A, **103** (1999) 9573-9578.

[69] L.B. Vilhelmsen, B. Hammer, J. Chem. Phys., **139** (2013) 204701.

[70] Z. Zhang, W. Tang, M. Neurock, J.T. Yates Jr., J. Phys. Chem. C, **115** (2011) 23848-23853.

[71] A. Visikovskiy, H. Matsumoto, K. Mitsuhara, T. Nakada, T. Akita, Y. Kido, Phys. Rev. B, **83** (2011) 165428.

[72] C. Zhang, A. Michaelides, D.A. King, S.J. Jenkins, J. Am. Chem. Soc., **132** (2010) 2175-2182.

[73] T. Okazawa, M. Fujiwara, T. Nishimura, T. Akita, M. Kohyama, Y. Kido, Surf. Sci., **600** (2006) 1331-1338.

[74] S. Hong, T.S. Rahman, J. Am. Chem. Soc., **135** (2013) 7629-7635.

[75] M.A. VanHove, W.H. Weinberg, C.-M. Chan, *Low Energy Electron Diffraction*, Springer-Verlag Berlin Heidelberg, (1986) 604.

[76] S. Hofmann, *Auger- and X-Ray Photoelectron Spectroscopy in Materials Science*, Springer-Verlag Berlin Heidelberg, (2013).

[77] G.A. Sawatzky, 5 - Auger Photoelectron Coincidence Spectroscopy, in: C.L. Briant, R.P. Messmer (Eds.) Treatise on Materials Science & Technology, Elsevier, (1988), 167-243.

[78] D.F. Stein, 1 - The Historical Development of Auger Electron Spectroscopy, in: C.L. Briant, R.P. Messmer (Eds.) Treatise on Materials Science & Technology, Elsevier, (1988), 1-15.

[79] G. Luckman, 2 - Studies of Surface Segregation Kinetics by Auger Electron Spectroscopy, in: C.L. Briant, R.P. Messmer (Eds.) Treatise on Materials Science & Technology, Elsevier, (1988), 17-63.

[80] J.E. Houston, R.R. Rye, 3 - Local Electronic Structure Information in Auger Electron Spectroscopy: Solid Surfaces, in: C.L. Briant, R.P. Messmer (Eds.) Treatise on Materials Science & Technology, Elsevier, (1988), 65-110.

[81] C.L. Briant, 4 - Metallurgical Applications of Auger Electron Spectroscopy, in: C.L. Briant, R.P. Messmer (Eds.) Treatise on Materials Science & Technology, Elsevier, (1988), 111-166.

[82] N.W. Ashcroft, N.D. Mermin, *Solid State Physics*, Cengage Learning, (2011).

[83] D.P. Smith, J. Appl. Phys., **38** (1967) 340-347.

[84] E.S. Mashkova, V.A. Molchanov, Radiat Eff., **23** (1974) 215-270.

[85] I. Stensgaard, Rep. Prog. Phys., **55** (1992) 989.

[86] R.D. Gann, Ph.D. thesis, University of California Riverside, (2011).

[87] O.S. Oen, Surf. Sci., **131** (1983) 407-411.

[88] H. Niehus, W. Heiland, E. Taglauer, Surf. Sci. Rep., **17** (1993) 91.

[89] J. Los, J.J.C. Geerlings, Phys. Rep., **190** (1990) 133-190.

[90] P. Nordlander, J.C. Tully, Phys. Rev. B, **42** (1990) 5564-5578.

[91] A.G. Borisov, D. Teillet-Billy, J.P. Gauyacq, H. Winter, G. Dierkes, Phys. Rev. B, **54** (1996) 17166-17174.

[92] R. Brako, D.M. Newns, Surf. Sci., **108** (1981) 253-270.

[93] G. Liu, Ph.D. thesis, University of California Riverside, (2006).

[94] B.L. Peko, T.M. Stephen, Nucl. Instrum. Methods B, **171** (2000) 597-604.

[95] R.S. Gao, P.S. Gibner, J.H. Newman, K.A. Smith, R.F. Stebbings, Rev. Sci. Instrum., **55** (1984) 1756-1759.

[96] L. Sangyeob, S. Aniketa, R. Regina, Nanotechnology, **20** (2009) 035701.

Chapter 2 A Low Energy Ion Scattering Approach for Studying Au Nanoclusters Grown on an H₂O Buffer Layer

2.1 Introduction

Buffer layer assisted growth (BLAG), initially developed by Weaver and coworkers, is a novel method for growing nanoclusters onto nearly any substrate [1, 2]. BLAG has been used to produce gold (Au), silver (Ag) and germanium (Ge) clusters, Au and palladium (Pd) bimetallic clusters, as well as II-VI quantum dots on various substrates [1-10]. Although direct deposition of metal atoms spontaneously forms nanoclusters on many oxides and other stable surfaces through a Volmer–Weber growth mode, only certain combinations of metals and substrates can be used. The materials that do not work have either a high surface free energy that favors the formation of a dispersed film or they chemically react with the substrate material. An advantage of BLAG is that it can be used to synthesize nanomaterials for many systems that would not otherwise form such clusters.

BLAG involves the deposition of metal atoms onto an inert frozen gas buffer layer (BL) condensed atop a substrate at cryogenic temperatures. Because the interactions between metal atoms are stronger than those between the metal and the BL, they combine to form clusters rather than a dispersed film. After metal atom deposition, the sample is warmed to desorb the BL while the clusters remain intact and soft-land onto the substrate. Nanoclusters produced by BLAG are generally more three-dimensional (3D) in shape and larger than those produced by direct deposition onto a clean substrate at room

temperature [2, 5]. Xe has most commonly been used as the BL material because it is inert and solidifies at a higher temperature than then other noble gasses [2, 8, 10]. Molecules, such as CO, CO_2, and H_2O, have also been used for BLs [4, 6, 11]. The ultimate size distribution of the clusters depends on many parameters, including the diffusion rate of the newly deposited metal atoms, the quantity of atoms deposited, the thickness of the BL and any agglomeration that occurs as the BL is removed.

It is believed that agglomeration during the warming process often alters the size distribution and shapes of the clusters from what they were when originally deposited onto the cold BL. Most of the tools previously used to investigate BLAG, such as scanning tunneling microscopy (STM) or scanning electron microscopy (SEM), can only measure the nanoclusters after the BL is removed and the clusters have landed on the substrate. It has been inferred from studies of the cluster sizes and shapes as a function of the BL thickness that the nanoclusters can increase in size and change shape as the layer is removed by annealing [1-6, 11, 12].

In previous work, our group used a novel method of low energy ion scattering (LEIS) to investigate Au and other metal nanoclusters spontaneously formed by direct deposition onto oxide substrates [13-15]. LEIS is an effective technique for investigation of nanomaterials as it has excellent surface sensitivity and can easily differentiate between the metal nanoclusters and the substrate. The presence of quantum size behavior was demonstrated using the neutralization probability of backscattered alkali ions, which is dependent on the local electrostatic potential (LEP) above the surface. The LEP above

a nanocluster changes as a function of size, which is then reflected in the measured neutral fraction (NF).

The work presented here uses LEIS to interrogate Au nanoclusters grown via BLAG onto a TiO$_2$(110) substrate employing an amorphous solid water (ASW) BL. Gross *et al.* used an ASW BL on SiO$_2$ and found that 3D nanoclusters are produced by BLAG [5]. LEIS is used here to delineate the details of the BLAG process, including monitoring the coverage of the substrate by the BL and the changes in the size distributions of the nanoclusters with Au coverage and as the clusters move from atop the condensed BL to the TiO$_2$ substrate. It is also shown that pre-adsorption of a sub-monolayer amount of water may produce nanoclusters that are even smaller than those formed by direct deposition. When enough water is adsorbed to create an ASW film, the nanoclusters increase in size with BL thickness for a fixed amount of deposited Au, which supports the assertion that they agglomerate during the warming process [2, 5]. It is demonstrated here that the BLAG protocol provides good control over the size distribution of the nanoclusters.

2.2 Experimental Procedure

The experiments are performed in an ultra-high vacuum (UHV) chamber with a base pressure on the order of 1x10^{-10} Torr. The sample is mounted on a XYZ rotary manipulator that enables the sample to access multiple instruments mounted on various ports in the chamber. The manipulator includes a cryostat that allows the sample to be cooled to 100 K via flowing liquid nitrogen. The instruments available include an ion

sputter gun for sample cleaning, a cylindrical mirror analyzer (CMA) for Auger electron spectroscopy (AES), and an alkali ion gun, flight tube and detector for performing charge-resolved LEIS via time-of-flight (TOF).

The sample is a polished rutile $TiO_2(110)$ single crystal ($5 \times 10 \times 1$ mm^3) purchased from the MTI Corporation. It is mounted onto a 5 mm by 15 mm rectangular 0.001" thick Ta foil that is spot welded to a sample holder attached to the cryostat at the foot of the sample manipulator. The foil is electrically isolated from ground and has contacts on each end. Current is run through the foil to heat the sample. A K-type thermocouple is mechanically held against the corner of the sample with a small Ta strap to measure the temperature of the crystal. The crystal surface is prepared via multiple cycles of sputtering and annealing (500 eV Ar^+ for 30 min and 1000 K for 2 min) [14]. AES and LEIS are used to confirm the cleanliness of the surface.

The ASW BL is formed on the 100 K $TiO_2(110)$ surface from water vapor introduced through a sapphire leak valve attached to the UHV chamber. Deionized water, stored in an ampule behind the valve, is freeze-pumped twice to ensure high purity of the H_2O vapor. The H_2O exposures are performed using a continuous flow from the leak valve into a turbomolecular pump opened to the main UHV chamber. The pressure during water exposure ranges between 5×10^{-9} and 1×10^{-7} Torr. The H_2O pressure is measured by an ion gauge, whose sensitivity is set for N_2, but the pressures are all multiplied by 0.89 in calculating the exposures to account for the sensitivity difference, in accordance with the Granville-Phillips manual. Exposures are reported in units of Langmuirs (L), where 1 L = 1×10^{-6} Torr sec [16, 17]. The actual thickness of the ASW

layer is not directly measured, but it is proportional to the exposure assuming that the sticking coefficient is constant, which is reasonable as it is expected to be near unity at 100 K [16, 18, 19].

There are a few issues that lead to some minimal systematic errors in reporting the exposures. For example, there is a rise and then a fall in pressure that occurs over tens of seconds caused by opening the leak valve slowly so as to not overshoot the desired pressure. Also, the walls of the UHV chamber act as a pump in adsorbing H_2O, which necessitates constant adjustment of the leak rate due to a changing pumping rate. Also, when the leak valve is closed at the end of each exposure, additional H_2O can desorb from the chamber walls.

Au atoms are deposited onto the sample by evaporation from Au wire (99.99%) wrapped around a W filament (Mathis) that is resistively heated. The rate of evaporation is approximately 0.01 ML sec^{-1} and is calibrated bi-weekly using a quartz crystal microbalance (QCM). One monolayer (ML) of Au represents the number of Au atoms needed to cover the surface with a closed packed arrangement that is one atom thick.[13]

The main technique used here is a specialized form of LEIS that measures the neutralization probability of scattered alkali ions. There are three Kimball Physics thermionic emitter ion guns that generate Li^+, Na^+ and K^+, two of which can be mounted in the main chamber at the same time. The ion beams are pulsed by deflection across a 1 mm diameter aperture using a custom square wave function generator (Avtech) whose two outputs oscillate from -100 to +100 V and 0 to +100 V at a rate of 80 kHz. The outputs are applied to two perpendicular sets of deflection plates, which allows for a

41

square pattern to be produced where one side of the square passes across the aperture during each cycle to produce uniform pulses with widths on the order of 100 ns. The scattered particles are analyzed using TOF to determine their velocity distributions. A dual microchannelplate (MCP) array located at the end of a 0.62 m long flight tube detects the individual scattered and fast recoiled particles. There is a 3 mm aperture at the entrance to the flight tube, which leads to an angular acceptance of 0.34°. The flight tube is positioned between the two ion guns at an angle of 45° relative to each, which corresponds to a 135° scattering angle. The sample faces the flight tube during experiments so that the emission is normal to the detector. The sensitivity of the MCP detector is independent of the charge state of the particles, but there is a steep drop off in absolute sensitivity as the kinetic energy falls below about 1 keV [20].

TOF spectroscopy allows not only for the collection of the kinetic energy distribution of the emitted fast particles, but also for an analysis of the fraction of projectiles that neutralize during scattering. A pair of deflection plates mounted in the flight tube is used to differentiate between charged and neutral scattered particles. When both deflection plates are grounded, all particles reach the detector and the total yield of charged and neutral species is measured. When the deflection plates have a 400 V potential difference across them, the charged particles are deflected away and only the fast neutrals are detected. The deflection plates are automatically switched on and off once per minute during data collection, which allows for separate spectra to be collected simultaneously and to thus avoid errors caused by long term drifts in the beam current.

Ion scattering is a destructive process. It can be assumed that every ion that interacts with the surface will knock off on average one surface atom and cause up to about 10 other atoms to be displaced [21]. To minimize beam damage, each spectrum is collected before 1% of the surface atoms are exposed to the beam. After exposure to a fluence beyond 1% of a ML, the sample is re-prepared.

2.3 Results and Discussion

2.3.1 Surface Composition

The BLAG process involves three primary steps [2]: (1) The sample is cooled to a cryogenic temperature and a BL is condensed onto the substrate. (2) Nanoclusters are generated by depositing metal atoms onto the BL. Due to the weak interaction of the metal atoms with the BL, the atoms coalesce into clusters rather than forming a dispersed film. (3) The BL is desorbed by heating the sample, causing the nanoclusters to soft-land onto the substrate where they remain intact although their size and shape may change during the BL removal process.

The experiments reported here use LEIS to ascertain the surface composition during all three steps as Au nanoclusters are grown onto rutile $TiO_2(110)$ using an ASW BL [18]. ASW has been used previously as a BL with a SiO_2 substrate [5, 11]. After depositing Au on the BL, the sample is heated to 320 K to remove the layer and soft-land the nanoclusters onto the TiO_2 substrate. This choice of annealing temperature is based on temperature programmed desorption (TPD) data for H_2O on $TiO_2(110)$, which shows

a multilayer peak at 170 K followed by a monolayer peak that indicates complete removal of H_2O by 320 K [22].

Figure 2.1 shows 3.0 keV Li^+ total yield TOF spectra collected following each of the three steps in the BLAG process. The spectra are displayed in units of time, rather than being converted to an energy scale, as multiple masses are often collected within a single spectrum. The spectra are plotted in reverse flight time, as shorter flight times correspond to larger kinetic energies. All three spectra contain a broad feature from approximately 5 to 3 μs. This feature primarily represents projectiles that have scattered from multiple target atoms, but may also include some recoiled surface atoms, as discussed below. Multiple scattering occurs when the projectile undergoes a series of collisions with several target atoms, which leads to a range of scattered projectile energies. Rather than increasing in intensity as the kinetic energy decreases, as would be expected for such a cascade-like process, this multiple scattering background has a "mound-like" shape caused by the reduction in MCP sensitivity as the kinetic energy falls below 1 keV [20]. A scattered Li^+ projectile with energy of 1 keV corresponds to a flight time of 3.7 μs, beyond which is approximately where the measured yield starts to decrease.
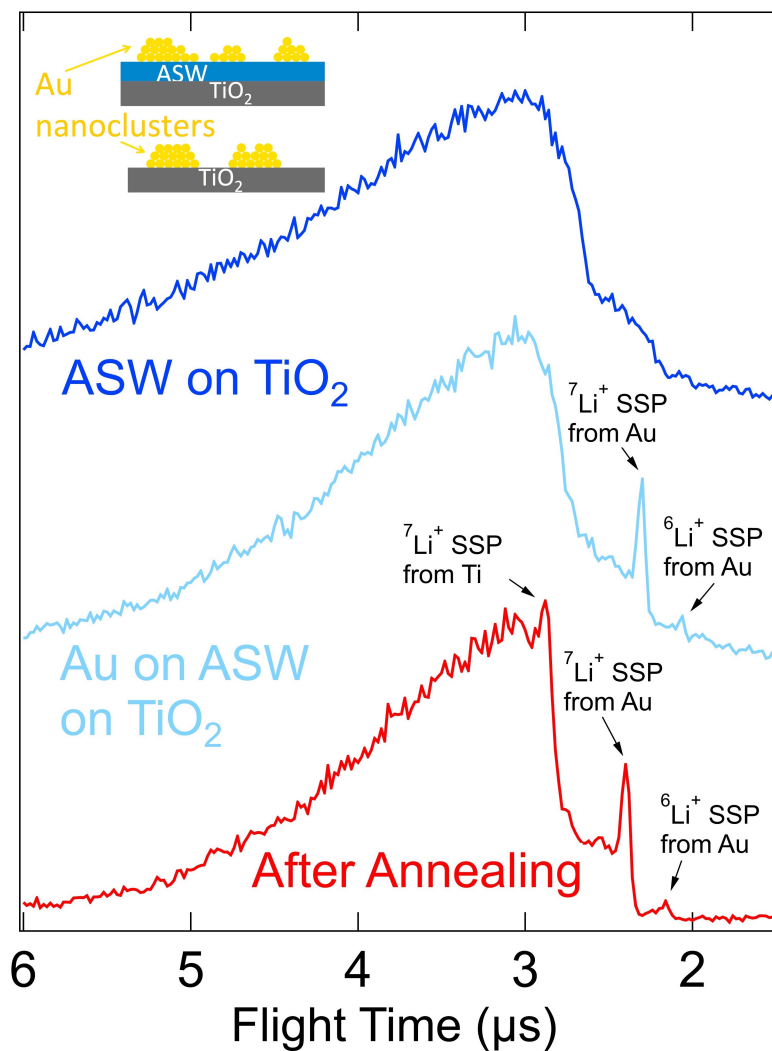
Figure 2.1 Typical Total Yield TOF spectra of scattered 3.0 keV Li^+. The sample probed in the upper spectrum was prepared by exposing $TiO_2(110)$ at 100 K to 9 L of H_2O (step 1). The middle spectrum was collected after deposition of 0.23 ML Au (step 2). The bottom spectrum was collected after the ASW layer was removed by heating to 320 K for 2 minutes (step 3). The graphic in the upper left is an illustration of Au clusters being grown on ASW (step 2) and then deposited onto the substrate (step 3).

In addition to the broad background, the middle and lower spectra in Fig. 2.1 show sharp peaks that result from single scattering. Single scattering occurs when a projectile experiences an elastic collision with one target atom such that it backscatters

directly into the detector. The energy of a singly scattered projectile can be calculated classically from conservation of energy and momentum, and is dependent on the ratio of the target atom mass to that of the projectile [21]. LEIS spectra thus reveal a sharp single scattering peak (SSP) for each elemental species at the surface that is directly visible to both the incident ion beam and the detector, provided that the energy of the scattered projectile is sufficient to trigger the MCP. At these large scattering angles, this implies that the target atom must be significantly more massive than the projectile. These conditions are met for Li scattering from Au and Ti, but not from O. The sharp peaks at 2.4 and 2.1 µs in the middle and lower spectra result from the scattering of Li projectiles from the surface atoms of the Au nanoclusters. The two SSPs represent the two stable isotopes of Li in the primary beam. ^{6}Li and ^{7}Li have naturally occurring abundances of 7.5% and 92.5%, respectively, and the peaks' relative sizes follow. There are two additional SSP's at 2.9 and 2.6 µs in the bottom spectrum that result from the two Li isotopes scattering from Ti atoms that are revealed after the BL desorbs, although the Ti SSP due to ^{6}Li is not easily visible above the background. Note that the presence of sharp peaks whose flight time does not change with water coverage provides a clear indication that sample charging is not a factor in these ion scattering measurements despite ice being an insulator.

The upper panel in Fig. 2.2 displays typical TOF spectra collected with 3.0 keV ^{23}Na$^+$ projectiles. The sample was grown by depositing 0.10 ML of Au atop an ASW layer that was produced via a 45 L H$_2$O exposure at 100 K. The upper spectrum in the top panel was collected after the Au was first deposited onto the BL (Au on ASW). The

bottom spectrum was collected after the sample was annealed to 320 K. Only one sharp feature is observed in these spectra, the Au SSP, as Na has only a single stable isotope. Although Na is lighter than Ti, there is no Ti SSP present in the spectrum after removing the BL as the energy of 3.0 keV Na scattered from Ti at 135° is too low to be detected by the MCP. There is also a broad feature to the right of the SSP in the spectrum collected in the presence of the ASW BL before annealing. Although some multiply scattered projectiles may contribute, this feature is primarily attributed to direct recoiling (DR).
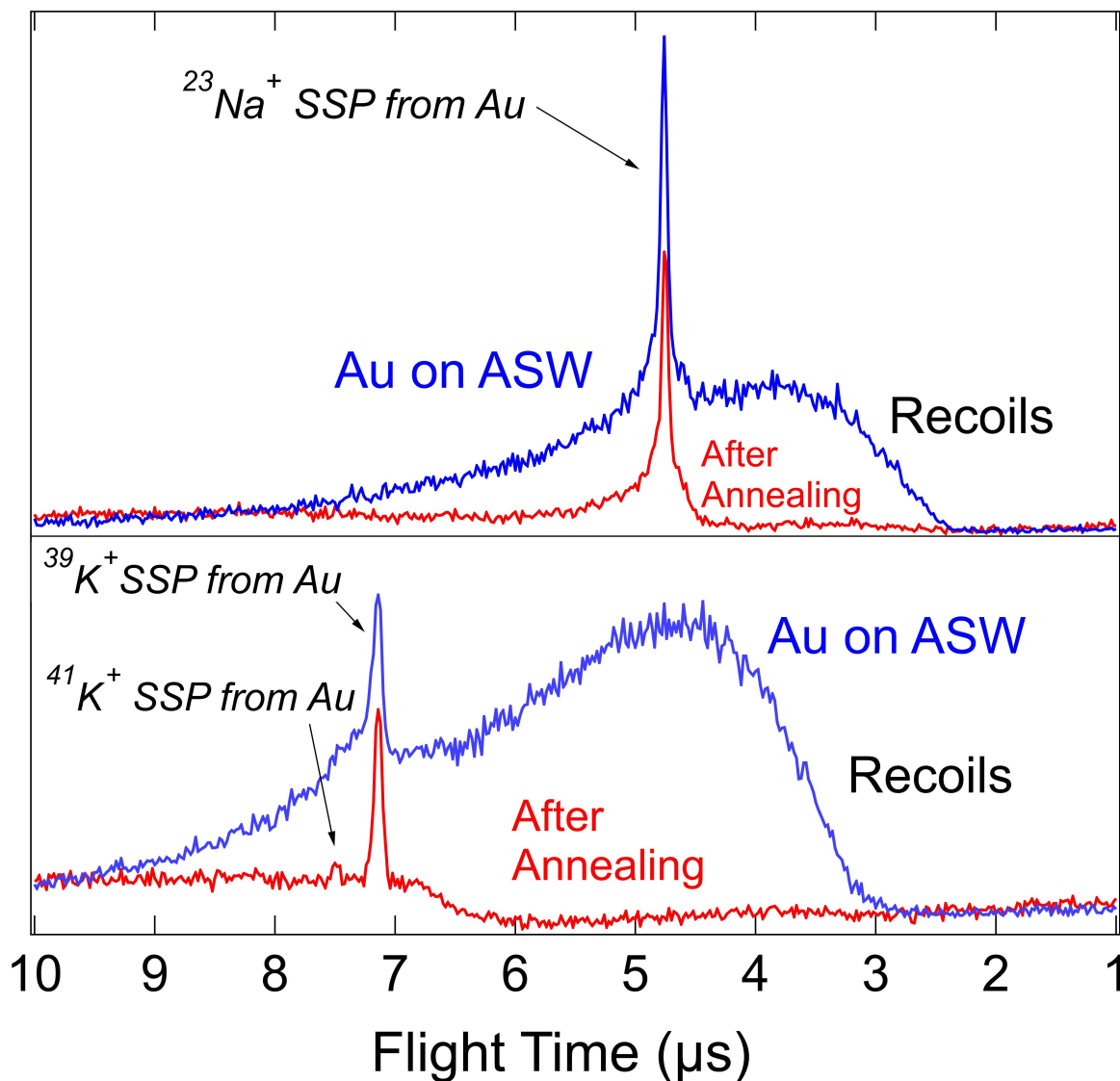
Figure 2.2 Upper panel: Typical total yield TOF spectra for 3.0 keV Na$^+$ scattered from 0.10 ML of Au deposited on ASW produced by a 45 L H$_2$O exposure at 100 K (step 2) and after annealing to 320 K for 2 minutes (step 3). Lower panel: TOF spectra for 3.0 keV K$^+$ scattered from 0.23 ML of Au deposited on ASW produced by a 90 L H$_2$O exposure before (step 2) and after annealing to 320 K for 2 minutes (step 3).

DR occurs when the projectile knocks light target atoms off the surface through simple collisions that impart a large amount of kinetic energy to the emitted atomic particles [23]. Recoils can be produced through a single collision in a forward scattering

geometry, which forms a distinct peak in the spectrum. When using a backscattering geometry as in the present case, however, multiple collisions are needed to remove a surface adsorbate via recoiling, which leads to a large range of kinetic energies and a broad DR peak. For example, the target atom can be hit by the projectile in such a way that it collides with another surface atom and then backscatters into the detector. Alternatively, the projectile can backscatter from a second layer atom, and then collide with a surface atom to produce a DR. Thus, the recoils measured under backscattering conditions result from a plethora of trajectories with the common thread being the emission of a fast surface atom. The yield of DR increases when the mass ratio of projectile to the recoiled particle increases. Thus, K projectiles produce more recoils than Na, which is verified by the data in Fig. 2.2. Note that Li projectiles produce very little DR, so that there is no prominent feature attributed to them in Fig. 2.1.

The bottom panel of Fig. 2.2 displays TOF spectra collected using 3.0 keV K^+ after Au was deposited onto the BL and after the sample was annealed to remove the layer. As with the Li, there are two Au SSPs present because K has two stable isotopes. The natural abundances of ^{39}K and ^{41}K are 93.26% and 6.73%, respectively, and are reflected in the relative sizes of the SSP's. The smaller SSP at around 7.5 μs is more easily seen after the BL is removed. Because K is heavier than Na, the singly scattered projectiles travel at a lower velocity, thus taking longer to reach the detector, while the heavier K also creates more recoils. Thus, the DR feature is larger and better resolved from the SSP when using K projectiles.

The composition of the surface throughout the BLAG process is determined by analysis of data such as that shown in Figs. 2.1 and 2.2. The absence of a Ti SSP in the upper spectrum of Fig. 2.1 verifies that the TiO_2 substrate is completely covered by the ASW BL. When Au is deposited on the BL, the middle spectrum shows a Au SSP but no Ti SSP, which indicates that there is Au atop the ASW and that the deposition did not displace a significant amount of water. After annealing, the presence of the Ti SSP in the Li^+ spectra (Fig. 2.1) and the absence of DR in the Na^+ and K^+ spectra (Fig. 2.2) confirm that the ASW layer is fully removed and the nanoclusters are resident directly on the TiO_2 substrate.

2.3.2 Electronic Properties of the Nanoclusters

The neutralization of a scattered alkali ion is dependent on the local electrostatic potential (LEP), sometimes referred to as the local work function, directly above the target atom. Previous investigations of low energy alkali ions scattered from nanoclusters have shown that there is a correlation between the NF and the nanocluster size [13, 24], which enables LEIS to provide an indication of the size distribution. This method is applied here to investigate the clusters during the latter two BLAG steps.

The model most often used to describe charge exchange between low energy alkali projectiles and a solid metallic surface is resonant charge transfer (RCT) [25]. As the projectile approaches the target surface, the alkali ionization level sees its image charge in the metal and shifts up in energy. At the same time, the level hybridizes with states in the solid causing it to broaden. When the projectile is close to the surface,

electrons tunnel between the ionization level and the solid. Since the projectile moves quickly on the time scale of electron tunneling, equilibrium is not achieved. Instead, a non-adiabatic charge exchange process causes the measured probability for charge transfer to be effectively frozen in along the exit trajectory as the projectile passes through a particular "freezing" distance above the surface, which is typically on the order of 1-3 Å [26, 27]. The measured neutralization probability is dependent on the relative positions of the ionization potential of the projectile and the LEP of the solid just above the scattering site at the freezing distance. In general, a smaller local work function (LEP) leads to a larger NF, and vice versa. This enables neutralization in alkali LEIS to provide unique information about the electronic structure of surfaces, such as the inhomogeneity of the LEP in the presence of adsorbates [24, 28-32].

For scattering from metal nanoclusters adsorbed on insulating substrates, it has been shown that the NF directly correlates with the size of the nanoclusters [13, 24]. Small clusters have quantum-confined electronic states and the clusters are generally thought to be negatively charged [33, 34], so that electrons from these filled states efficiently neutralize the scattered alkali ions. In contrast, solid Au has a rather large work function compared to the Na and K ionization energies, so that the neutralization probability of Na^+ and K^+ in scattering from bulk Au is near zero [13, 35]. Thus, the NF decreases as more Au is deposited and the size of the clusters increases so that the Au becomes more bulk-like.

Representative Au SSPs in total and neutral yield TOF spectra for Na^+ scattering are shown in the inset to Fig. 2.3 to illustrate how the NFs are calculated. The shape of a

SSP is determined by the kinematics of the scattering process and is thus independent of the peak size, so that the same background subtraction process can be used for both the total and neutral yield spectra. The background is modeled as a straight line with the same average slope as the regions on both sides of the peak. The shaded regions in the inset of Fig. 2.3 illustrate how the SSP is typically separated from the underlying background. After background subtraction, the area under these peaks is integrated to find the total intensity of each SSP, and the NF for a specific SSP is then determined by dividing the area of the neutral yield by that of the total yield. The error is assumed to be purely statistical so that the square root of the total number of counts under each SSP, including the background, is used to determine the maximum and minimum NF shown by the error bars in subsequent analyses.
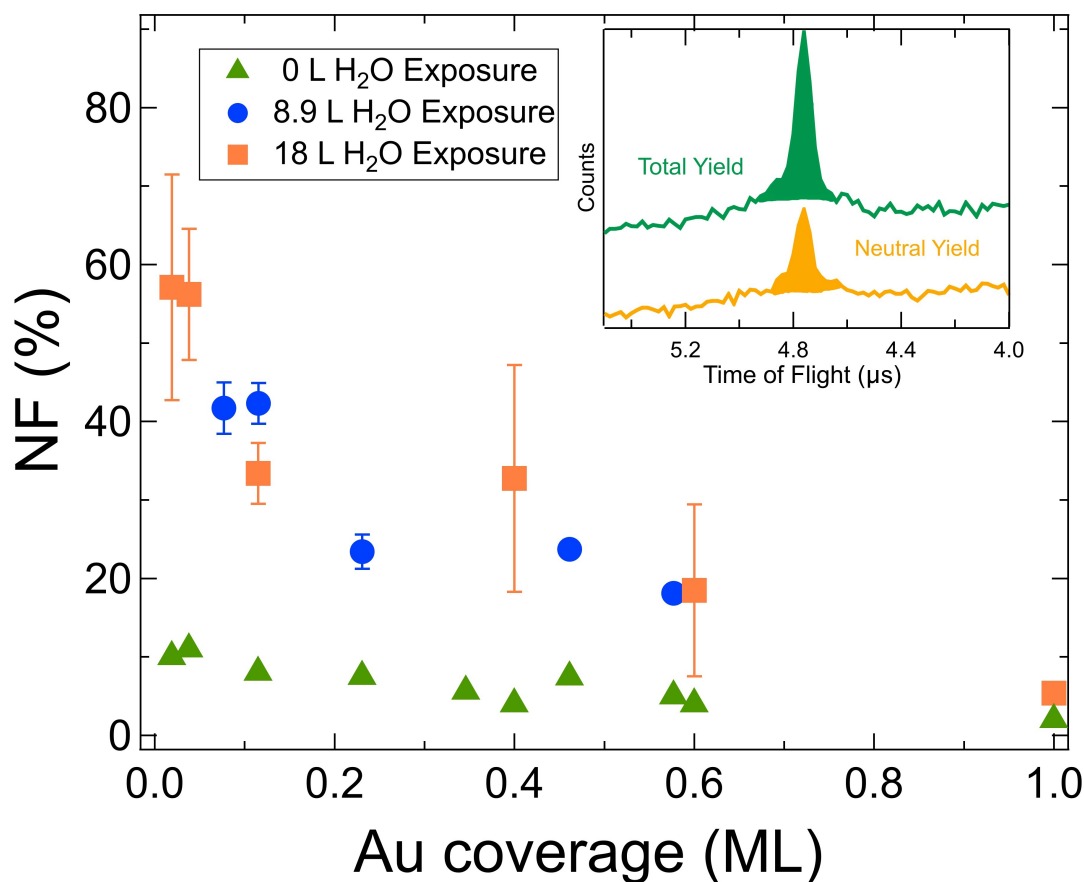
Figure 2.3 The NF of the Au SSP as a function of Au coverage for deposition onto clean TiO$_2$ and after 9 and 18 L water exposures at 100 K, using 3.0 keV ^{39}K$^+$ projectiles. Inset: A blowup of the total and neutral yield Au SSPs in TOF spectra collected using 3.0 keV Na$^+$ scattered from 0.10 ML of Au on ASW produced by a 45 L H$_2$O exposure. The shaded regions indicate typical areas used in calculating the NF.

Figure 3 shows the NF of the Au SSP for scattered 3.0 keV ^{39}K$^+$ as a function of coverage for Au deposited onto clean TiO$_2$ and for Au deposited onto an ASW BL at 100 K for two different BL thicknesses. All of the NFs decrease with increasing Au coverage, which is expected since increasing coverage corresponds to increasing cluster size [13, 35]. From STM work in the literature, the average diameter of the Au clusters formed by

direct deposition are 2.0 nm for a 0.10 ML coverage and 3.7 nm for a 1.0 ML coverage [36].

A question about the NFs obtained from nanoclusters deposited on ASW concerns the contribution of the substrate to the LEP at the surface. If there was a significant electronic interaction between the TiO_2 and the clusters, then the NF might change with BL thickness as the clusters would be positioned further from the substrate. The measured NFs are the same over the range of two ASW thicknesses shown in Fig. 3, which suggests that there is a negligible electronic interaction between the Au nanoclusters and the underlying TiO_2 so that proximity to the substrate is not important.

It is also seen that the NF after deposition onto ASW at any Au coverage is higher than for the same amount of Au directly deposited onto TiO_2 [35]. This increase in the NF is likely due to the change in work function caused by the ASW layer. As H_2O adsorbs on TiO_2, it is known from the literature that the work function decreases linearly until it plateaus at 1.1 eV below that of the clean surface [22]. While this suggests that one of the main reasons for the difference in NF between clusters on the bare surface and those atop the BL is this change in work function, it is also possible that the clusters themselves are different, since their size and shape also effect the NF. It is thus critical to separate out how the NF is affected by changes in global work function from changes in the LEP due to the cluster size.

To accomplish this, small Au depositions and small H_2O exposures up to ~8 L are performed in both possible orders to de-convolute the competing effects of work function and the size and shape of the clusters. The size of the clusters is not expected to depend

on the order for such small BL thicknesses and Au coverages, as the substrate is largely bare. In Fig. 2.4, the NF of the Au SSP for K^+ scattering from 0.23 ML of deposited Au is shown as a function of water exposure for both sequences. Data collected from Au nanoclusters deposited on clean TiO_2 and then exposed to water are shown as circles. Data collected from TiO_2 that is first exposed to water and then followed by Au deposition, which is the same sequence as step 2 in the BLAG process, are shown as squares. The NFs in both cases for small H_2O exposures are nearly equal, providing evidence that in this coverage regime the cluster sizes are independent of the order in which the water and Au are deposited. The presence of H_2O on the surfaces prepared in either way causes the work function to decrease and the NF to go up, as expected. There is a sudden stop to this NF change at around 2 L, which is assumed to correspond to the coverage at which the maximum H_2O-induced work function change is realized. Thus, the increase in NF for water exposures below 2 L must be solely due to the work function change caused by the presence of H_2O. Note that when H_2O is condensed atop the Au nanoclusters, Au is no longer visible to the ion beam after an exposure of about 12 L. Data is not shown beyond 7 L, however, as the Au signal at that point is very weak so that the error bars are extremely large.
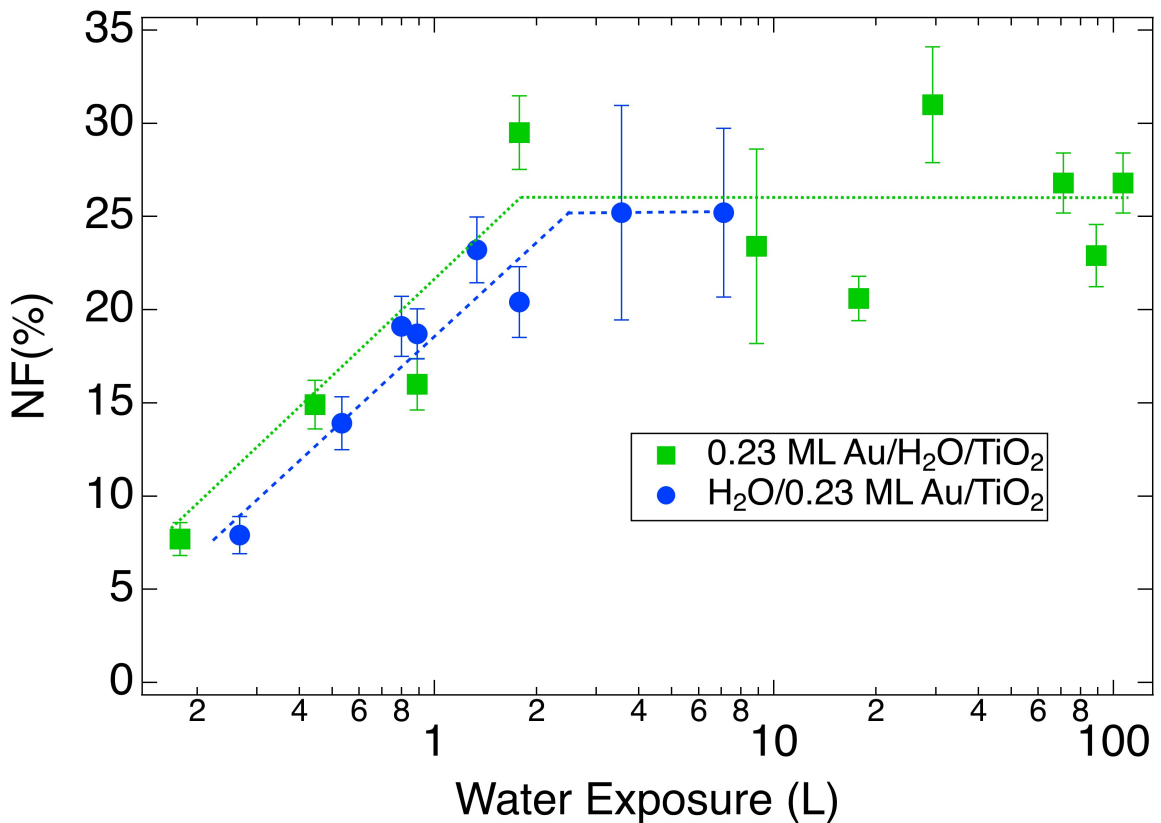
Figure 2.4 The NF of the Au SSP for 3.0 keV K^{+} scattered from 0.23 ML of Au deposited on TiO_2 shown as a function H_2O exposure. The squares indicate data collected when the Au deposition followed the water exposure, while the circles show data collected when the water exposure was performed after the Au deposition. The x-axis is plotted on a log scale and the dashed lines are guides to the eye.

Figure 2.5 shows the NF of the Au SSP before and after BL removal as a function

of water exposure for fixed Au coverages of 0.10 ML and 0.23 ML for Na^{+} (upper panel)

and K^{+} (bottom panel) projectiles, respectively. For every data point collected when the

Au was resident on the ASW BL (step 2, represented as squares) there is a corresponding

data point collected after the sample was annealed (step 3, represented as circles). The

water exposure is plotted on a log scale to aid in visualizing the data. As a reference, the

horizontal dashed line in the upper panel of Fig. 2.5 shows the Na^{+} NF for Au

56

nanoclusters grown by directly depositing 0.10 ML of Au atop TiO_2. The STM measurements of Lai *et al.* indicated that the diameter of the directly deposited clusters is 2.0 nm at this coverage [36].

Note that the relative size of the error bars depends on the local environment of the nanoclusters. In the absence of ASW, the error bars are all approximately equal in size. The data collected in the presence of ASW, however, have error bars that increase in size with water exposure, which is caused by the overlap in time of the Au SSP and the DR particles, as seen in Fig. 2.2. This trend is more apparent with Na projectiles, as the Au SSP is better resolved from the recoil signal when using K.

In order for BLAG to form nanoclusters, at least one full layer of ASW must be present on the surface. A question to be asked is what is the minimum water exposure needed to create a continuous ASW film that acts as a BL for nanocluster growth. H_2O deposits as bilayers so that ideally a 2 L exposure would be the minimum required to form a continuous ASW layer on the surface [19]. It has also been reported, however, that Au penetrates the ASW BL to some extent during deposition which can impact the ability to form clusters through BLAG even with a full bilayer of deposited H_2O.[37] Au was always clearly visible to the ion beam following step 2, however, indicating that the Au was either not buried at all or at most only partially buried in the ASW at all coverages.

Between water exposures of ~0.09 to ~5 L, the NF is slightly reduced when the BL is removed. As shown by the analysis of Fig. 4, the change in NF from step 2 to step 3 in this exposure range is mostly caused by the increase in work function due to the removal of H_2O. This suggests that the clusters are minimally disturbed and maintain

their size since such a negligible amount of H_2O is removed. Note, however, that the change in NF for Na^+ caused by the presence of H_2O is not nearly as large as that for K^+. The NF for Na^+ goes from about 45% with a minimal H_2O coverage to 60% (a factor of ~1.3 increase, Fig. 5), as compared to the NF of K^+ which goes from 7% with no H_2O to 25% (a factor of ~3.5 increase, Fig. 2.4). This is due to the ionization energy of K being smaller than that of Na making it more sensitive to work function changes in this regime.

For water exposures below 2 L, the upper panel of Fig. 2.5 shows that the Na^+ NFs are slightly higher after removal of the BL than for Au directly deposited onto TiO_2. An ASW film would not be formed following such small H_2O exposures, as instead the water would be adsorbed, possibly in small islands, leaving bare areas of the substrate. The deposited Au can then be considered more as being co-adsorbed with the water, rather than atop a BL. The increase in the NFs above those for directly deposited Au indicate that the co-adsorbed nanoclusters may be slightly smaller than for the same amount of Au deposited onto a clean surface. This could be a consequence of the adsorbed water decreasing the ability of the Au atoms to diffuse when deposited and form larger clusters. This result suggests that it may be possible to use the BLAG protocol with less than a full BL to produce smaller clusters than those formed by direct deposition.
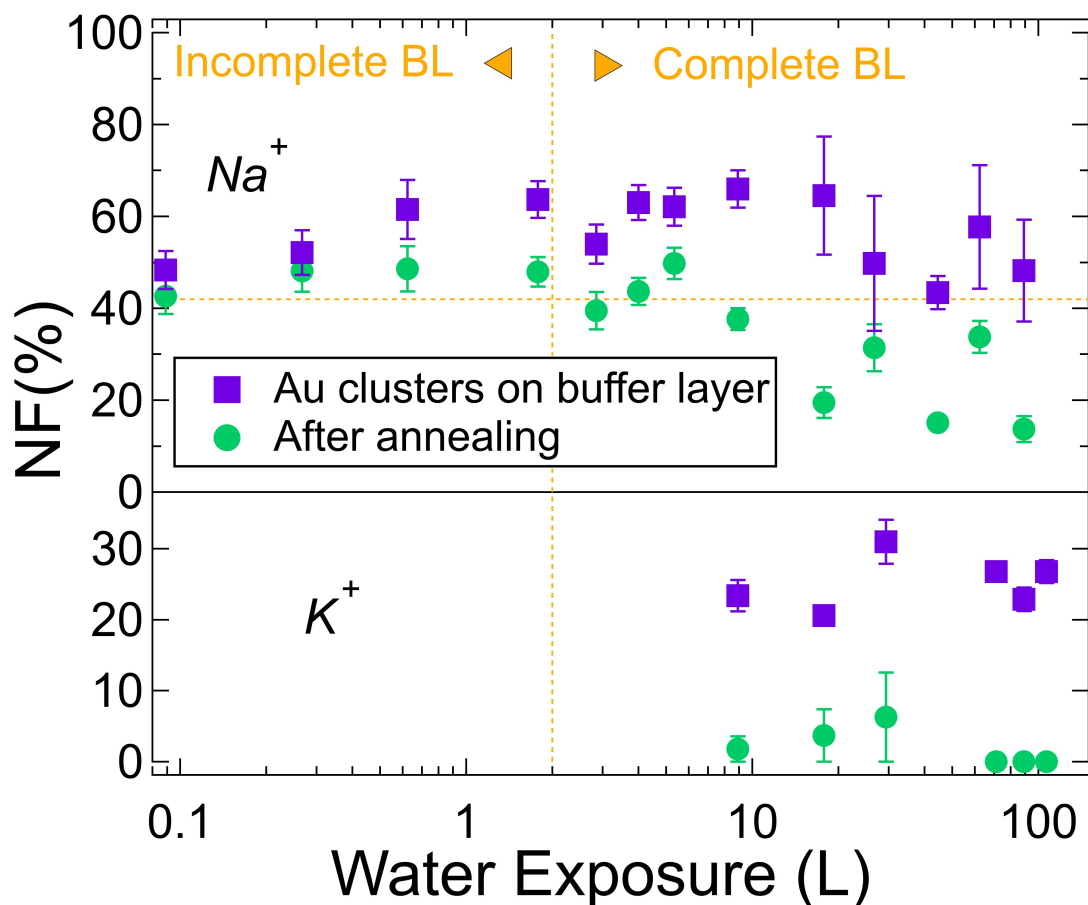
Figure 2.5. The NFs of 3.0 keV $^{23}Na^+$ and $^{39}K^+$ scattered from 0.10 ML of Au (upper panel) and 0.23 ML of Au (lower panel), respectively, plotted as a function of water exposure on a log scale. Data collected after Au deposition at 100 K (step 2) are shown by squares and data collected after annealing (step 3) are indicated by circles. The horizontal dashed line in the upper panel shows the NF of 0.10 ML of Au directly deposited onto TiO_2 at 100 K. The vertical dashed line represents a 2 L water exposure.

The Au SSP NFs decrease significantly when the BL is removed by annealing for H_2O exposures greater than 8.9 L. Since these exposures are beyond the point at which the work function contribution to the NF has saturated and the magnitude of the change is larger than the change due to water adsorption alone, this result implies that the clusters increase in size during the BL removal process. In addition, the NF values are below the

horizontal dashed line, indicating that the clusters are larger than those formed by direct deposition of the same amount of Au.

This shows that the amount of Au deposited on the BL determines the initial size distribution, but agglomeration of the nanoclusters during the warming stage occurs for BLs that are thicker than ~5 ML, increasing their size. Palmer *et al.*[12] proposed that the BL desorbs from the surface as a wave, which leads to the clusters mixing at the wave front. The utility of the present measurements is that the changes in cluster size from step 2 to step 3 are monitored as they occur and as a function of the BL thickness.

In the lower panel of Fig. 2.5, a handful of NFs using K^+ projectiles are displayed. As previously shown in Fig. 2.3, the NF for K^+ scattered from Au deposited directly on TiO_2 is relatively small, which is due to the fact that the ionization potential of K is smaller than the Au work function. Thus, the Au SSP using K^+ projectiles has an extremely low NF, particularly after removal of the BL, thereby making K less useful for observing size changes due to agglomeration [5] during the BLAG process despite the large change that results from the work function change associated with the removal of water. This suggests that Na is the preferred ion for studying Au nanoclusters despite the increased overlap of the SSP and DR.

Note that another concern about the use of ASW as a BL is the formation of pores, which are reported to have diameters between 1.5 and 2 nm and separations of 2.6 nm (from center to center), that are present even on ASW films as thick as 66 ML [38]. Au atoms are smaller than these holes and single atoms can conceivably land inside of a pore, which would leave less Au to form clusters atop the BL. This may be happening to

a small degree, but it does not appear to be significant as this would lead to an increased NF for the Au/H$_2$O/TiO$_2$ data set in Fig. 2.4. When the BL is removed, any Au atoms in the pores would have an opportunity to coalesce with the nanoclusters as they soft-land onto the substrate and slightly increase the size of the clusters.

2.4 Conclusions

Nanoclusters form when Au is deposited onto ASW, and the clusters agglomerate when the BL is removed and they soft land onto the underlying TiO$_2$ substrate. To the best of our knowledge, this is the first time that the relative sizes of the Au nanoclusters resident on top of the BL are compared to those after the BL is removed by annealing. This comparison is inferred from changes in the neutralization probability of scattered low energy alkali ions. The result agrees with previous work in the literature that the enhancement of the nanocluster size when the BL is removed increases with BL thickness [2-5]. In addition, it is shown that beyond a 2 L water exposure, the NF for a given Au deposition is independent of the BL thickness, which implies that the distance between the cluster and the oxide substrate does not affect the LEP above the clusters.

The work presented here indicates that the BLAG technique can be used to engineer specific cluster sizes and shapes with more flexibility then with direct deposition alone, as BLAG produces a different size distribution. A direct comparison of the height differences between clusters formed by direct deposition and BLAG using an ASW BL showed that BLAG produces 3D clusters, although ref. [5] did not employ very small exposures. It is shown here that for exposures below 2 L, the clusters can actually be

61

smaller than those formed by direct deposition onto TiO_2. This is due to the nature of the adsorbed water itself, as small exposures do not produce a fully-formed BL thus allowing small nanoclusters to be formed directly on the substrate. It is possible that a more porous or choppy BL material could exaggerate this behavior and produce even smaller clusters. When the H_2O exposure is sufficient to form a complete ASW film, the resultant clusters are larger than those prepared by direct deposition. Future work will include alkali LEIS along with STM or SEM measurements of clusters formed with BLs of various materials to more accurately determine the size differences as a function of co-adsorption and BL thickness and to compare the clusters to those produced by direct deposition and other methods.

Bibliography

[1] J.H. Weaver, V.N. Antonov, Surf. Sci., **557** (2004) 1-3.

[2] L. Huang, S.J. Chey, J.H. Weaver, Phys. Rev. Lett., **80** (1998) 4095-4098.

[3] C. Haley, J.H. Weaver, Surf. Sci., **518** (2002) 243-250.

[4] V.N. Antonov, J.H. Weaver, Surf. Sci., **526** (2003) 97-106.

[5] E. Gross, Y. Horowitz, M. Asscher, Langmuir, **21** (2005) 8892-8898.

[6] P.S. Waggoner, J.S. Palmer, V.N. Antonov, J.H. Weaver, Surf. Sci., **596** (2005) 12-20.

[7] E. Gross, M. Asscher, Langmuir, **26** (2010) 16226-16231.

[8] L. Wen-Chin, C. Huang-Yu, H. Yu-Tsen, K. Chien-Cheng, Jpn. J. Appl. Phys., **48** (2009) 08JB07.

[9] J. Honolka, V. Sessi, J. Zhang, S. Hertenberger, A. Enders, K. Kern, Phys. Status Solidi B, **247** (2010) 1063-1068.

[10] V.N. Antonov, P. Swaminathan, J.A.N.T. Soares, J.S. Palmer, J.H. Weaver, Appl. Phys. Lett., **88** (2006) 121906.

[11] E. Gross, M. Asscher, M. Lundwall, D.W. Goodman, J. Phys. Chem., **111** (2007) 16197-16201.

[12] J.S. Palmer, P. Swaminathan, S. Barbar, J.H. Weaver, Phys. Rev. B, **77** (2008) 195422.

[13] G.F. Liu, Z. Sroubek, J.A. Yarmoff, Phys. Rev. Lett., **92** (2004) 216801.

[14] A.B. Arjad, J.A. Yarmoff, Phys. Chem. C, **116** (2012) 23377-23382.

[15] S. Balaz, J.A. Yarmoff, Surf. Sci., **605** (2011) 675-680.

[16] D.E. Brown, S.M. George, C. Huang, E.K.L. Wong, K.B. Rider, R.S. Smith, B.D. Kay, J. Phys. Chem., **100** (1996) 4988-4995.

[17] I. Langmuir, Phys. Rev., **8** (1916) 149-176.

[18] R.S. Smith, B.D. Kay, Nature, **398** (1999) 788-791.

[19] D.J. Safarik, R.J. Meyer, C.B. Mullins, J. Vac. Sci. Technol. A, **19** (2001) 1537-1542.

[20] R.S. Gao, P.S. Gibner, J.H. Newman, K.A. Smith, R.F. Stebbings, Rev. Sci. Instrum., **55** (1984) 1756-1759.

[21] H. Niehus, W. Heiland, E. Taglauer, Surf. Sci. Rep., **17** (1993) 91.

[22] M.B. Hugenschmidt, L. Gamble, C.T. Campbell, Surf. Sci., **302** (1994) 329-340.

[23] E. Taglauer, Surf. Sci., **299–300** (1994) 64-76.

[24] A.R. Canário, V.A. Esaulov, J. Chem. Phys., **124** (2006) 224710.

[25] J. Los, J.J.C. Geerlings, Phys. Rep., **190** (1990) 133-190.

[26] G.A. Kimmel, B.H. Cooper, Phys. Rev. B, **48** (1993) 12164-12177.

[27] R.D. Gann, J.X. Cao, R.Q. Wu, J. Wen, Z. Xu, G.D. Gu, J.A. Yarmoff, Phys. Rev. B, **81** (2010) 035418.

[28] C.B. Weare, J.A. Yarmoff, Surf. Sci., **348** (1996) 359-369.

[29] J.P. Gauyacq, A.G. Borisov, J. Phys.: Condens. Matter, **10** (1998) 6585-6619.

[30] E.R. Behringer, D.R. Andersson, B.H. Cooper, J.B. Marston, Phys. Rev. B, **54** (1996) 14765-14779.

[31] C.A. Keller, C.A. DiRubio, G.A. Kimmel, B.H. Cooper, Phys. Rev. Lett., **75** (1995) 1654-1657.

[32] J. Shen, J. Jia, K. Bobrov, L. Guillemot, V.A. Esaulov, Gold Bull., **46** (2013) 343-347.

[33] T. Minato, T. Susaki, S. Shiraki, H.S. Kato, M. Kawai, K. Aika, Surf. Sci., **566–568** (2004) 1012-1017.

[34] X. Yu, L. Xu, W. Zhang, Z. Jiang, J. Zhu, W. Huang, Chin. J. Chem. Phys., **22** (2009) 339-345.

[35] G.F. Liu, P. Karmakar, J.A. Yarmoff, J. Vac. Sci. Technol. A, **25** (2007) 1133-1136.

[36] X. Lai, T.P.S. Clair, M. Valden, D.W. Goodman, Prog. Surf. Sci., **59** (1998) 25-52.

[37] X.-M. Yan, J. Ni, M. Robbins, H.J. Park, W. Zhao, J.M. White, J. Nanopart. Res., **4** (2002) 525-533.

[38] E. Vichnevetski, A.D. Bass, L. Sanche, J. Chem. Phys., **113** (2000) 3874-3881.

Chapter 3 Inhomogeneous Charge Distribution Across Gold Nanoclusters detected by Neutralization of Scattered Low Energy Alkali Ions

3.1 Introduction

Over the past 30 years, a large body of research has been conducted to explore and explain the high catalytic activity of gold (Au) nanoclusters supported on oxide substrates [1-4]. These clusters are composed of several to hundreds of Au atoms and have reaction rates that rival those of enzymes, which is in contrast to bulk Au's extremely inert character. The activity depends on cluster size, with the highest rates for the oxidation of CO being those approximately 3.2 nm in diameter [5]. Nanoclusters have also found use in other applications such as functionalization capabilities in biology [6, 7] and quantum computing [8]. Although it can be said that Au nanoclusters are the "gold standard" in nano-catalysts, there are a variety of other metals that also form catalytically active nanoclusters when deposited on an oxide support [1, 9-12]. There are many ways to fabricate nanoclusters, including physical vapor deposition (PVD), chemical vapor deposition, buffer layer assisted growth, size selected deposition, and chemical synthesis [13-16].

PVD is one of the most popular methods used to grow Au nanoclusters on surfaces in ultra-high vacuum (UHV) [3]. Au atoms are deposited randomly onto a substrate, via a thermal atomic beam, on which they diffuse to spontaneously form the clusters. Au atoms deposited onto an oxide substrate follow a Volmer-Weber growth

mode in which they initially coalesce to form flat, single atomic layer clusters and, with additional deposition, form multilayer clusters prior to a full monolayer of deposition [17]. Such clusters formed by direct deposition onto an oxide surface are flatter than gas phase nanoclusters that consist of the same number of atoms [18]. At each coverage of Au, there is a narrow distribution of nanocluster sizes on the substrate [19-21]. As more Au is deposited, the average size of that distribution increases until enough Au is present that the clusters combine into a complete thin film [17]. The detailed internal atomic structure of the supported nanoclusters is not well known, however, as techniques such as scanning electron or tunneling microscopy cannot image the individual atoms [17, 22].

Multiple explanations of the high catalytic activity of Au nanoclusters have been proposed that include the roles of quantum size effects, increase of low-coordinated atoms, cluster morphology, substrate defects, and charge state [23-26]. Much of the current consensus is that the catalytic reactions occur at the edges of the nanocluster via adsorption to the Au atoms that are directly bonded to oxygen in the substrate [27-29]. These edge atoms are presumably positively charged due to electron transfer in bonding to oxygen [30, 31]. Note that a good deal of earlier work had suggested that Au nanoclusters were overall negatively charged [4, 32-34], while other work has shown that the aggregate charge is positive [32, 35-37]. Thus, the overall charge state of deposited nanoclusters is not firmly established and may depend on the particular materials involved.

Low energy ion scattering (LEIS) was initially developed in the 1960s as a means to provide information about the elemental composition of surfaces [38, 39]. Most LEIS

experiments employ noble gas ions as projectiles due their ease of preparation and extreme surface sensitivity when using a charged particle detector, which is related to their irreversible Auger-type of neutralization [40].

In contrast, scattered alkali ions neutralize by a resonant charge exchange mechanism due to the overlap between their relatively small ionization potentials and the surface conduction bands [41]. Studies of scattered alkali ions show that the neutralization probability is dependent on the local electrostatic potential (LEP) just above the surface. There have been experimental and theoretical investigations of the neutralization probability in low energy alkali scattering from surfaces that have non-uniform local electrostatic potentials created by adsorbing small numbers of adatoms onto clean metal surfaces, which changes the overall work function, and then measuring different neutralization probabilities for scattering from each type of atom [42-46]. The results of these studies showed that the LEP close to the surface can vary leading to different neutralization probabilities for scattering from the different elements at the surface. In particular, scattering from a positively charged adatom, such as an alkali adsorbate at low coverage, has a significantly higher neutralization probability than scattering from the substrate due the upward pointing dipole that lowers the LEP above the adatom site [45-47].

Measurements of the neutralization probability of scattered low energy alkali projectiles is a useful tool for investigating deposited nanoclusters on oxides. This is because the alkali LEIS technique is adept for studying surfaces composed of multiple elements and can address questions about the charge state of those elements. Previous

results have shown that the ions scattering from Au and Ag nanoclusters on an oxide and other substrates have a much higher neutralization probability than those scattered from the bulk metal, and that neutralization decreases as the cluster size increases [48-55]. Although it is possible that the alkali LEIS neutralization rate and the Au nanocluster catalytic activity are related, a satisfactory model has not yet been developed to explain the enhanced neutralization so that such a correlation has not been confirmed.

To explain the unusually high neutralization for alkali ions scattered from small Au nanoclusters, a model is developed here based on the notion that the charge associated with each Au atom in a cluster can be different. Previously, the charge on the Au clusters had been considered in aggregate when analyzing ion neutralization [49-56], but the present model is dependent on the differences in charge between the atoms and not on the average charge. Density functional theory (DFT) calculations performed for Au nanoclusters supported on TiO_2 find that the charge associated with the edge atoms of the nanocluster are noticeably different from the center atoms [27, 31]. Coincidentally, it is those same edge atoms that are the catalytically active sites [29, 30, 57]. A parameterized model is developed here to illustrate how the neutralization of singly scattered low energy alkali ions can depend on cluster size by combining the relative charge values of the center and edge atoms in a nanocluster, as determined from DFT, with the traditional paradigm for scattered low energy alkali neutralization. Inter-nanocluster interactions that affect the strength of the dipoles on the edge atoms when the clusters are close to each other also need to be included in the model to properly reproduce the experimental data. The success of this model shows how ion scattering can implicitly discern the presence of

an inhomogeneous charge distribution within an individual deposited nanocluster. In addition, the neutralization probability differences between low energy Na^+ and Li^+ ions scattered from Au nanoclusters is provided by this model [54].

3.2 Experimental Procedure

Experiments are performed in an UHV chamber with a base pressure better than $5x10^{-10}$. The sample is mounted on the foot of an XYZ rotary manipulator that allows it to access all of the sample preparation and surface analysis tools in the chamber. The tools include low energy electron diffraction (LEED), x-ray photoelectron spectroscopy (XPS) and low energy ion scattering (LEIS).

The substrate is a polished $TiO_2(110)$ single crystal purchased commercially. It is prepared in UHV by cycles of sputtering with 500 eV Ar^+ and annealing to 975 K for 15 min [49]. LEED and XPS are used to verify the crystal order and cleanliness. The nanoclusters are formed on the crystal surface by PVD using a thermal atomic beam of Au. The atomic beam is produced by running current through a W filament (Mathis) with Au wire wrapped around it that is mounted inside a Ta case with an aperture facing the sample [17, 35]. The evaporation rate is calibrated by a quartz crystal microbalance (QCM).

LEIS is performed using time-of-flight (TOF) spectroscopy to measure both neutral and charged particles. Beams of 2.0 keV Li^+ and Na^+ ions are produced by thermionic emission guns (Kimball Physics) that are pulsed at 80 kHz, with a pulse width of roughly 100 ns. Once a projectile has scattered from the target, it travels down the 0.46

m long TOF leg where it is detected by a series of three microchannel plates (MCP). The entrance to the first MCP is grounded so that neutral and charged particles are measured with equal sensitivity, although the absolute sensitivity decreases significantly with smaller scattered kinetic energies beginning at about 1.5 keV [58-60]. Each gun is separated from the TOF leg by 30°, leading to scattering angles of 150°. A set of deflection plates in the TOF leg is used to separate the charged and neutral particles. When both plates are grounded, all of the scattered particles pass through yielding the total counts, while placing 300 V across the plates deflects the ions allowing only neutral particles to be collected. Further details of the experimental procedure are found in Liu *et al.* [54].

The use of Li^+ and Na^+ ion beams incident on the sample simultaneously enables a comparison of data collected from the same surface with different projectiles. Since the projectiles have different masses but the same incident kinetic energy, they travel at different velocities. The difference in arrival times allows for the separation of features due to scattered Na and Li within a single spectrum.

In addition, the protocol is to never allow more than 1% of the surface atoms to be impacted before re-preparing the sample to minimize beam damage so that the data always reflect the intact clusters. This is easier when using TOF methods, as opposed to electrostatic analysis, because the pulsed beams have a small duty cycle even with two ion beams impacting the sample.

3.3 Experimental Results

The LEIS technique is typically employed for the determination of the elemental composition of the first few atomic layers of a sample [39]. When TOF is used to measure all scattered particle, LEIS is surface sensitive because of shadowing and blocking. Shadowing occurs when atoms in the outermost layers prevent ions from the incident beam from reaching the deeper layers so that direct scattering cannot occur. Blocking occurs when projectiles scatter from a second or deeper layer atom but are prevented from reaching the detector because of scattering by a surface atom. Shadowing and blocking are often illustrated by calculating the shape of cones, which are the regions behind each atom from which the projectiles are excluded. Because of shadowing and blocking, the projectiles that are detected are primarily those that scatter from the outermost atomic layers, making this technique ideal for studying materials such as catalysts where the chemistry takes place on the surface [61, 62]. In analyzing LEIS data, it is assumed that the target atoms are located at specific lattice sites, but that they are unbound since the projectile energies far exceed the atomic bonding energies. It is furthermore assumed that the projectiles interact with one target atom at a time, which is the binary collision approximation (BCA).

Typical TOF-LEIS spectra for Li^+ and Na^+ scattered from Au nanoclusters are shown in Fig. 3.1 with the scattered particle yields on the y-axis and time on the x-axis. The x-axis is reversed so that higher energy scattered projectiles are to the right. The target is a well-ordered $TiO_2(110)$ substrate onto which 0.5 ML of Au is deposited, which is a small enough coverage that nanoclusters are formed rather than a Au film.
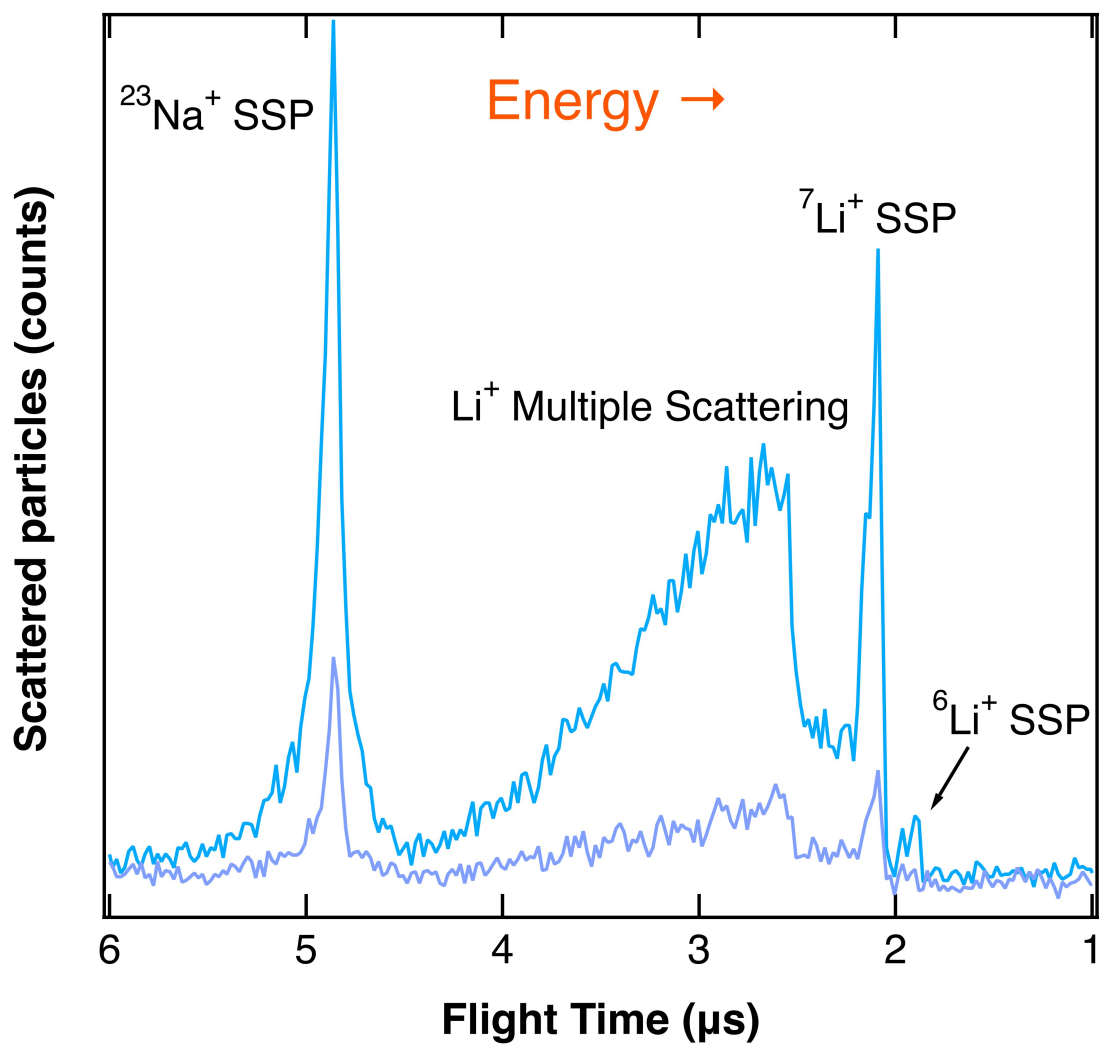
Figure 1. TOF-LEIS spectra of 2.0 keV Li^+ and Na^+ scattered from 0.5 ML of Au deposited on $TiO_2(110)$ shown as a function of the flight time from the sample to the detector. The upper spectrum (blue online) is the total yield and bottom spectrum (purple online) is the neutral yield.

A single scatting peak (SSP) occurs when a projectile elastically scatters directly into the detector after making a hard collision primarily with one surface target atom. With the beam energy (2.0 keV) and scattering angle (150°) held constant, the kinetic energy of a singly scattered projectile is dependent primarily on the ratio of the target to projectile atomic mass [63]. Note that there is also a small amount of inelastic energy loss caused by electron excitations that lower the energy of a SSP, but the magnitude of this energy loss is negligible and can be ignored in the present analysis [39]. There are three clear SSPs present in both the total and neutral yield spectra due to the single isotope of Na and two isotopes of Li scattering from Au atoms. The kinetic energy of ^{23}Na scattered from Au is 1290 eV and for ^{7}Li it is 1750 eV (ignoring any inelastic energy losses), which correspond to flight times of 4.86 and 2.09 μs, respectively. The SSP for ^{6}Li scattering from Au is also visible in the spectra, but its intensity is minimal due to its small isotopic abundance. Since Li is less massive than Na, it is scattered at a higher velocity, which leads to a shorter flight time. Fortunately, there is clear separation of the Na and Li signals so that these scattering events can be analyzed independently.

Multiple scattering occurs when a projectile interacts with more than one target atom, leading to a distribution of energies rather than to a sharply defined SSP. Multiply scattered Li particles are observed as a mound to the left of the Li SSP because Li is light enough to backscatter into the detector following multiple collisions with Au, Ti and/or O atoms and still retain enough kinetic energy to be detected. Fortunately, under the conditions of these measurements, the mound is sufficiently narrow that it is clearly

74

separated from the Na SSP. There is no multiple scattering mound for scattered Na because it has a larger mass and thus cannot backscatter from the light substrate atoms.

Although Au is not the only element present on the surface and visible to the ion beams, SSPs due to scattering from Ti and O do not appear in the spectra. Na is less massive than Ti, but the scattered energy at 150° is 280 eV which is too low to be detected by the MCP [58]. Na is more massive than O and will thus not singly scatter at a large angle. Li can scatter from O but would have an energy of 350 eV, again being too low for detection. Li scatters from Ti with a kinetic energy of 1160 eV, or at a flight time of 2.57 μs, which can be observed by the MCP. The Ti signal is not large, however, because the Au nanoclusters cover part of the TiO_2 surface, the cross section for ^7Li scattering from Ti is approximately a factor of 3.4 smaller than for scattering from Au [63], and the Ti SSP is buried underneath the Li multiple scattering background.

When alkali ions scatter from a surface, their neutralization probability depends on the local electrostatic potential (LEP) above the target atom, the energy and width of the ionization s level at a certain distance above the surface and the velocity of the projectile along its outgoing trajectory. The model most often used to describe this interaction is resonant charge transfer (RCT), which was originally developed for clean metal surfaces [41, 64]. In the RCT model, the approaching alkali's ionization level sees its image charge in the conductive metal surface and shifts up in energy. The ionization level also hybridizes with the levels in the surface, causing it to broaden. Once the projectile is close enough to the surface, charge quantum mechanically tunnels between the target conduction band and the broadened and shifted s level because they overlap

75

due to the small ionization energies of alkalis. After the projectile has scattered and is sufficiently far from the surface along its exit trajectory, tunneling can no longer occur. In the limit of small velocity, the process would be adiabatic and produce 100% neutralization since the ionization levels of Li and Na, which are the 2s and 3s, respectively, both lie below the Fermi energy. Because the projectile velocities in the low energy regime are large on the scale of the electron tunneling rates, however, the charge transfer process occurs non-adiabatically, which leads to a measured neutralization probability that is frozen in very close to the surface, typically a few Å's above the scattering site [64]. Although this freezing does not actually occur at a specific distance since the interaction weakens exponentially, the freezing distance is defined as the effective distance above the scattering site at which the overlap of the Fermi energy and the broadened and shifted ionization level leads to the measured neutralization probability.

A clean metal surface is a simple case for ion neutralization because of the uniform lateral potential that allows the global work function to determine the NF, but the process is more complex in the presence of an adsorbate. Because an adsorbate can lead to a non-uniform LEP, the neutralization would then depend on the LEP just above the scattering site, rather than on the global work function [41, 65]. In this context, the LEP is sometimes referred to as the local work function. For example, if an electropositive adatom, such as an alkali, is adsorbed on a surface, it donates most of its outer shell electron to the surface creating an upward pointing surface dipole at the adatom site [66]. The dipole is formed by the positive charge of the alkali adatom and its negative image

charge in the substrate. This upward pointing dipole reduces the LEP directly above the adsorbate which, in turn, increases the NF of a low energy alkali ion scattered from that adatom. At low alkali adatom coverages, where there are isolated non-interacting dipoles, the NF in scattering from the adatoms is larger than from bare areas of the surface, indicating that the LEP of the surface is inhomogeneous [47, 65, 67, 68].

In order to measure neutralization probability, or neutral fraction (NF), in an experiment, the neutral and total yield SSPs are integrated and divided. Before integration, the background of multiply scattered projectiles is first subtracted from the SSP. The background is estimated by fitting the region surrounding each SSP to a linear function. The error bars of each SSP area are estimated by taking the square root of the total number of counts, including the background counts, which is assuming that the error is purely statistical. This error is then propagated to determine the statistical error associated with each NF.

Figure 3.2 presents the NF of Li^+ singly scattered from Au on the TiO_2 substrate shown as a function of the average Au nanocluster size, while Fig. 3.3 shows the NF for scattered Na^+. The experimental data is shown by the solid circles. The average diameter of the nanoclusters was determined by calibration to the scanning tunneling microscopy (STM) measurements of Lai *et al.* using the amount of Au deposited as determined by the QCM [17]. It is seen that the NF is on the order of 30% for Li and 50% for Na scattered from very small Au nanoclusters, and that it decreases with cluster size until it reaches the same value as that for scattering from bulk Au, as reported previously [48, 49, 54].

Note that the figures show experimental data as well as simulations generated by the model described in the following section.
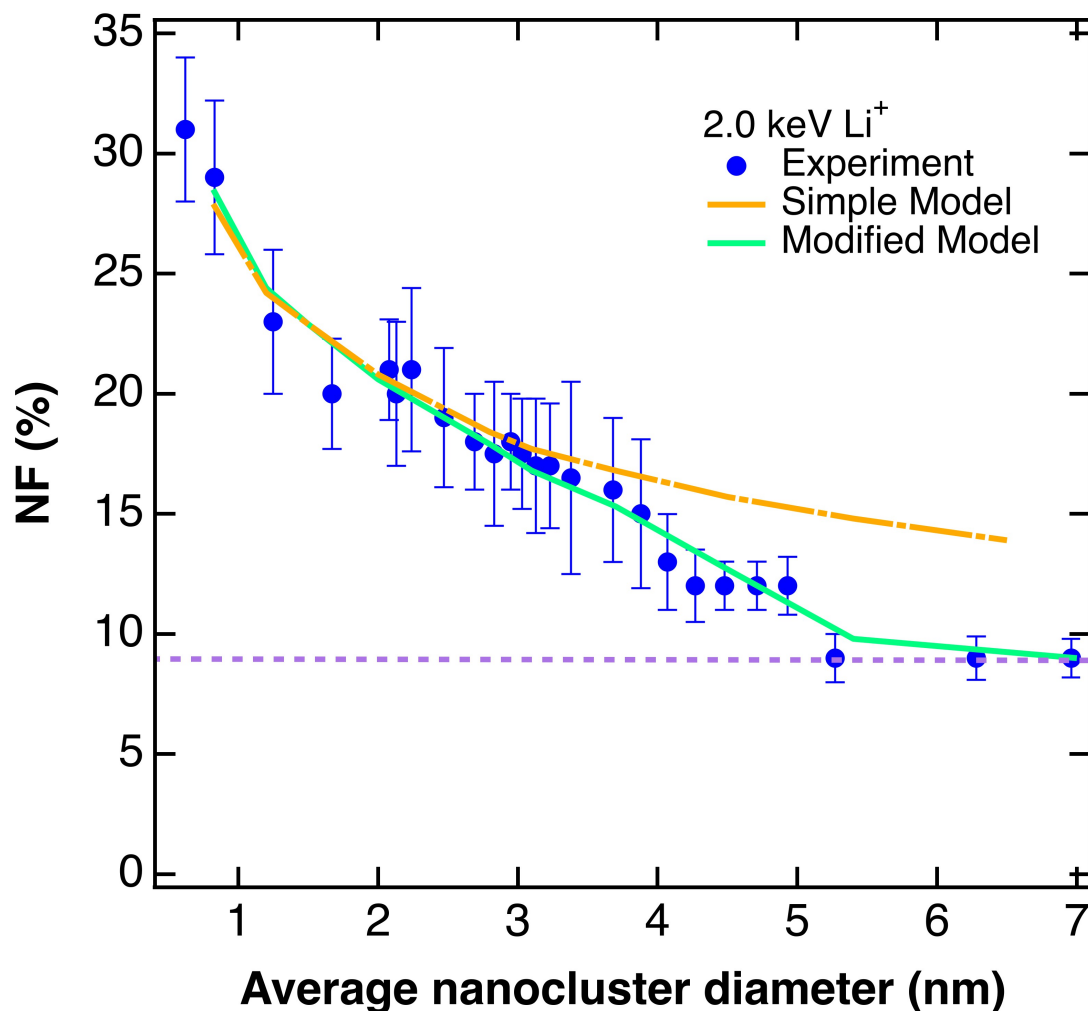
Figure 2. Experimental and simulated data of the NF of 2.0 keV Li$^+$ singly scattered from Au shown as a function of the average nanocluster diameter. The filled circles indicate the experimental data, the upper fragmented line (orange) is the simple model with NF_E = 31%, and the solid line (green) is the modified model with NF_E = 33% (see text). In all of the simulations, NF_C is set to 9%, which is the value for scattering from bulk Au as represented by the horizontal dashed line.
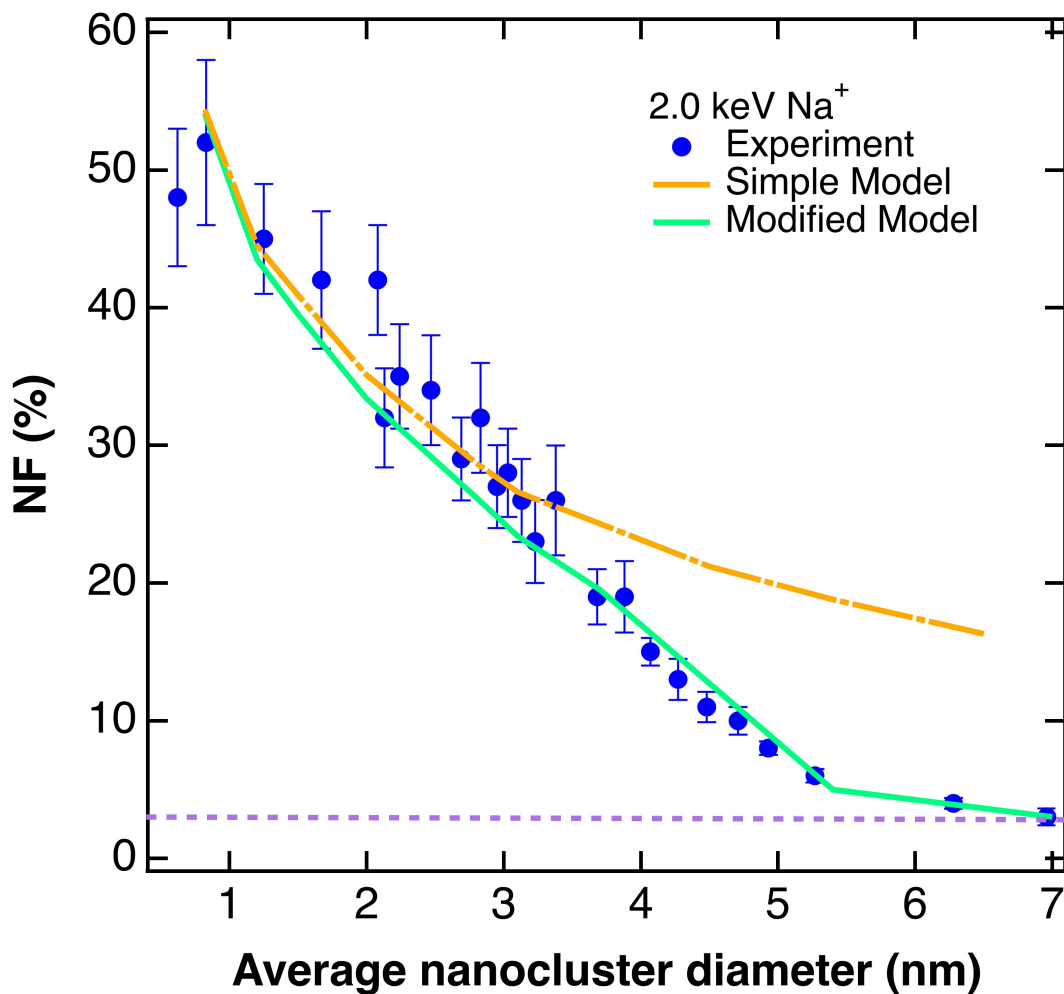
Figure 3. Experimental and simulated data of the NF of 2.0 keV Na^+ singly scattered from Au shown as a function of the average nanocluster diameter. The filled circles show the experimental data, the fragmented line (gold) is the simple model with $NF_E = 63\%$, and the solid line (green) is the modified model with $NF_E = 66\%$ (see text). In all of the simulations, NF_C is set to 3%, which is the value for scattering from bulk Au as represented by the horizontal dashed line.

3.4 Model

The model developed here to explain the change of NF as a function of cluster size is based on the notion that all of the atoms in a nanocluster are not electrostatically equivalent so that there is a difference in the neutralization probability of a scattered alkali projectile depending on the particular atom that is impacted. This assertion is supported by DFT calculations that show that the edge atoms of Au clusters deposited onto TiO_2 are positively charged, with an average charge per atom of about +.0458 e, while the center atoms are nearly neutral [27, 31]. This is illustrated schematically in the insets to Fig. 3.4, where the edge atoms are labeled with a "+" sign, while the neutral center atoms are unlabeled. Photoelectron spectroscopy measurements have suggested that Au nanoclusters have some positive charge, which supports the results of the DFT calculations, but they were not able to distinguish differences in charge across a nanocluster [32, 35]. The positively charged atoms at the edge form upwards pointing dipoles leading to a higher LEP above them than the LEP above the nearly neutral interior atoms so that alkali ions scattered from the edge atoms of the nanocluster would have a higher neutralization.
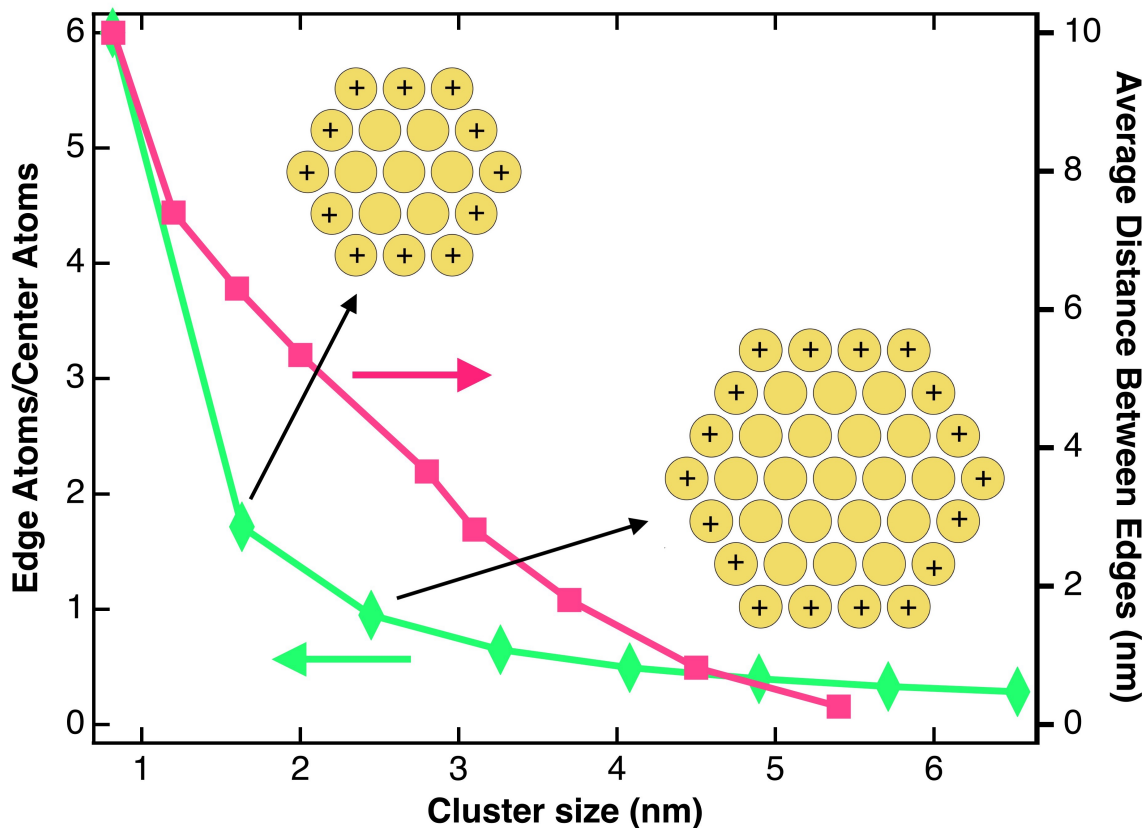
Figure 4. The ratio of edge atoms to center atoms as a function of cluster size used in the model is represented as diamonds with respect to the left axis (see text). The average distance between the edges of nanoclusters as a function of average size cluster is represented by squares with respect to the right axis. The insets show schematic diagrams of representative Au nanoclusters that correspond to two cluster sizes: 19 atoms with a diameter of 1.6 nm and 37 atoms with a diameter of 2.5 nm. The plus signs indicate the positively charged edge atoms.

The clusters are modeled here as being flat and consisting of a single atomic layer with a fcc hexagonal packing pattern and a (111) surface orientation. The distance between the Au atoms is set to 0.408 nm, which is the interatomic spacing in bulk Au metal. Single layer cluster sizes are employed that contain 7 to 217 atoms, which correspond to diameters from 0.82 through 6.5 nm. Although no crystalline structure is

observed for actual deposited Au nanoclusters, this structure is chosen for the model because the (111) face is the low energy surface of fcc metals [17]. Some examples of these model nanoclusters are shown as insets in Fig. 3.4. In reality, the nanoclusters are not hexagonal (this would have been observed with STM, high resolution scanning electron microscopy, or transmission electron microscopy [17, 69, 70]) and the actual distance between the Au atoms can change depending on the cluster size and shape and the substrate material [17, 71]. Nevertheless, the smallest Au clusters on surfaces are flat and one atomic layer thick, so that this approximation is sufficient to illustrate the basic physics of how the NF depends on cluster size.

As the size of the clusters increases, the number of edge atoms relative to center atoms decreases so that there are relatively fewer positively charged target atoms. Thus, the overall NF should decrease as the cluster size increases. Figure 3.4 shows the ratio of edge to center atoms using this approximation for the cluster atomic structure, and the ratio does go down as the clusters get larger. A numerical model is presented here to show that this idea can reproduce the observed NF vs. cluster size data.

A simple way to calculate the expected NF for Na^+ and Li^+ scattered from Au nanoclusters using this model is to assign different neutralization probabilities to the edge (NF_E) and center (NF_C) atoms in each cluster. It is further assumed that the LEP above the interior atoms is the same as that of neutral bulk Au, which leads to neutralization probabilities of $NF_C = 3\%$ for scattered Na^+ and $NF_C = 9\%$ for Li^+, as determined experimentally [49, 72]. Since the edge atoms are positively charged, scattering from them would produce larger values. NF_E, the neutralization probability in scattering from

82

the edge atoms, is thus a parameter in the model that needs to be determined. The overall NF generated by the model for a particular cluster size is calculated by averaging the individual neutralization probabilities in scattering from each of the Au atoms in the simulated clusters as

$$\overline{NF} = \frac{\left(N_E \times NF_E\right) + \left(N_C \times NF_C\right)}{N_E + N_C}$$

(3.1)

where N_E and N_C are the number of edge and center atoms, respectively, for a given nanocluster size.

Since the placement of the atoms in this model are assumed to be at fcc-like sites, while the incident ion beam is normal to the Au(111) face, the incoming ions should be able to impact the first 3 atomic layers. When this assumption is used along with allowing the clusters to be 3 atomic layers thick and assigning the highest possible value of NF_E = 100% and NF_C = 3% for all the other atoms in the top 3 layers, the overall NF at a given Au coverage is still much lower than the experimental values for a range of cluster sizes when using Na^+. Even assuming that the ions see only the top 2 layers produces NFs that are smaller than the experimental data. Assuming that scattering only occurs from the outermost Au layer, however, generates NFs that better match the experimental data over a range of sizes. This was similarly tested for using Li^+ by setting NF_C = 9% and showing that if scattering from second and third layer atoms is included, there is no value for NF_E that will fit a majority of the data. At best, with NF_E set to be near 100%, only a few mid-

83

range cluster sizes would match the data and the majority of cluster sizes would have an overall NF that is too high. If a smaller value is use for NF_E, only the smallest cluster sizes would match the data until a bulk film is formed.

For the above reasons, the model only considers single layer clusters. This could mean that either in reality the clusters are all just a single atomic layer thick, which is not consistent with STM data [9], or more likely that the actual structure of the clusters is such that the 2nd layer and deeper lying Au atoms are all shadowed or blocked by the outermost Au atoms and do not contribute to the SSP. Shadowing and blocking is likely as the structure of the actual clusters is sufficiently different from Au(111) and Au is a heavy atom that produces large cones. The shadow cone radii of 2.0 keV Li$^+$ and Na$^+$ ions scattered from Au, for example, are calculated to be 1.05 Å and 1.25 Å, respectively, at a distance of 4 Å beyond the Au atom [73], which is close to the spacing between Au atoms. Since the shadow cone radii for Li$^+$ and Na$^+$ are not too dissimilar, it is likely that both projectiles probe close to the same depth. The agreement between the model and experimental data, discussed below, shows that the use of single layer hexagonal clusters provides a reasonable approximation to the actual structures of the clusters for the purposes of the model.

One strategy to estimate the neutralization probability of Na$^+$ and Li$^+$ ions scattered from the edge atoms, NF_E, is to calculate the dipole moment and then compare it to experimental NF data from another system with a known dipole moment. The dipole at the edge atoms is calculated by multiplying the distance d, between the two charges, by the absolute charge q of one of them. The charge for the edge atom is taken from the

average of all of the edge atoms' charge as calculated in Ref. [27]. The distance is estimated to be two times the bond length of Au-O, which is determined by first principle calculations to be 2.08 Å [74]. This is the classic image charge problem, which generates an average dipole value for edge atoms directly attached to a substrate oxygen atom of 18.0±2.7 D. Reference [27] also provides values for the charge on the interior atoms and, in a similar manner, these values produce an average dipole moment of 1.4±1.6 D.

A comparison to previously published data is used to relate the dipole moment at an adatom site to the NF. Weare *et al.* determined that for very low coverages of Cs adatoms on Al(100), a dipole moment of 15.2 D is generated by the Cs adatoms [47]. Using 2.0 keV Li$^+$ projectiles (same as in the present experiment), a NF of ~70% was observed in scattering from Cs. Therefore, the value for Li scattering from the edge atoms based solely on the dipole strength would be a bit more than 70%. Although the relationship between dipole moment and NF is not linear, a simple extrapolation would predict a NF_E of 81%. Since Cs and Au are relatively close in mass, any changes in neutralization due to differences in their scattered energy are minimal. Note that experimental data for the neutralization of Na$^+$ scattered from Cs adatoms are not available, so a similar estimate cannot be made.

If a value of 81% is used for the Li$^+$ NF_E, however, the model does not numerically match the experimental data, although it does have the same general trend. The fact that such an analysis of dipole strength does not work to precisely determine a neutralization probability is either due to inaccuracies in the estimate of the dipole strength or because there is a distinct difference between edge atoms of nanoclusters on

85

TiO$_2$(110) and isolated Cs adatoms on Al(100). One of these differences could involve effects of the substrate on the broadening, shifting, and freezing distance, as these could be considerably different for a metal and insulator. Therefore, the neutralization probability in scattering from a positively charged Au adatom in a nanocluster is not necessarily the same as the NF in scattering from an alkali adatom on a metal.

Since it is not possible to estimate the neutralization probability for scattering from the edge atoms directly from the dipole strength, a simple model is first developed in which a best fit of NF_E to the experimental data is performed. The results of this simulation for Li$^+$ scattering from Au clusters using $NF_E = 31\%$ and $NF_C = 9\%$ are shown in Fig. 3.2 by the dashed-dotted line labeled "Simple Model". Correspondingly, the results of a simulation for the scattering of Na$^+$ in which $NF_E = 63\%$ and $NF_C = 3\%$ are shown in Fig. 3.3. Both of these simulations match the experimental data fairly well for cluster sizes up to about 3.7 nm, but the simulated NF for larger clusters is too high for both projectiles. The fact that the model shows a decrease in NF with cluster size and the values agree with the experimental data for both projectiles in the same nanocluster size region indicates that the underlying physics of the model is basically sound, at least for the smaller clusters.

The failure of the simulations for larger clusters sizes is likely caused by a change in dipole strength with cluster size, which would thereby affect the LEP and thus the neutralization probability in scattering from edge atoms. There are two possible ways in which this could be explained. First, the charge associated with the edge atoms could depend on the cluster size as a fundamental property of the clusters. Second, as the

nanoclusters grow in size they become more densely packed and are thus closer together. At a certain coverage, the edge atoms would be close enough to those of neighboring clusters to interact and depolarize the dipoles so that their strengths reduce, thus increasing the LEP above the edge atoms and decreasing NF_E. A similar effect is seen for high coverages of alkali adatoms on metals surfaces in which the dipole strength reduces when the alkali coverage reaches the point at which the adatoms interact with each other [47, 65, 67].

There is no simple physical reason to suggest that the edge atoms' charge would depend on the cluster size independent of neighboring clusters, but it is not impossible. The data, however, suggest otherwise since a constant value of NF_E works for projectiles scattered from nanoclusters less than about 3.0 nm in diameter. If the edge atom charge were size dependent, it would be unlikely that this dependency would not affect the dipoles at the edge atoms of the smaller clusters.

Thus, the second idea is used to develop a modified model that incorporates the effects of a reducing dipole into the simulation as a consequence of interactions between clusters. In this more complete model, the effective neutralization of alkali ions scattered from the edge atoms, NF_{EE}, is adjusted as a function of cluster size and NF_E is considered to be a constant that represents the neutralization probability in scattering from edge atoms in non-interacting clusters.

To use this idea to produce a modified mathematical model that works for any cluster size, an equation is developed that depends on the distance between clusters, specifically the distance between the edge atoms of the nearest clusters, d. The method

adjusts NF_{EE} as a function of d with the aid of a fitting parameter. The average distance between the edges is calculated by taking the square root of the inverse density of clusters and subtracting the average cluster diameter, both of which are obtained from Lai *et al.* [17]. This generates the average distance between the edges of nearest neighbor clusters d in units of nm, which is plotted by the squares in Fig. 3.4. The equation used to determine NF_{EE} is

$$NF_{EE} = (NF_E - NF_C)e^{-A/d} + NF_C, \qquad (3.2)$$

where A is the fitting parameter. An exponential dependence on distance is a reasonable approximation of the electrostatic interaction between nearby dipoles. The equation reduces to the correct values at the limits when they are infinitely spaced ($d = \infty$) and when the nanoclusters are touching ($d = 0$). For infinitely spaced nanoclusters, there is no interaction between nanoclusters so that the neutralization in scattering from the edge atoms NF_E is the same as that determined from the simple model. For clusters that are so close that their edge atoms are adjacent, they are all now essentially center atoms so that the neutralization probability would be NF_C.

The value of A that produces a best fit to the data is found to be 0.55 nm for both Li and Na, implying that this effect is related to the nanoclusters and not to the projectiles. The value of A is also relatively close to the dipole length of 0.42 nm implying that it is physically reasonable. NF_E for both projectiles are slightly adjusted from the original estimates to $NF_E = 33\%$ and $NF_E = 66\%$ for Li^+ and Na^+, respectively.

These neutralization probabilities are slightly higher than those of the simple model, which is reasonable since it did not take the inter-cluster effects into account so that the best fit resulted in lower values.

Since the dipole-dipole interactions in this modified model are similar to the behavior of alkalis adsorbed on metal surfaces, the distance at which the alkali adatoms begin to interact is compared to the value of d at which the NF in scattering from nanoclusters is no longer consistent with the simple model. Measurements of the work function as a function of coverage for alkalis deposited on metals initially decrease with coverage and show a minimum at the point at which the adatoms begin to interact, which occurs at a adatom-adatom spacing of roughly 0.91 nm for Na on Al(100) [75]. The average size of the nanoclusters beyond which the simple model no longer agrees with the experimental data is around 3.9 nm, which corresponds to an average spacing of $d = 1.4$ nm. Note that this distance between clusters was calculated for the hexagonal clusters employed in the model, but if the same calculation is performed to find the average distance between the edges of circular clusters, the distance is 0.89 nm for 3.9 nm nanoclusters, which is essentially the same as the distance at which alkali adsorbates begin to interact. The data thus support the notion that the interaction between nanoclusters is responsible for the reduction in the effective neutralization probability of projectiles scattered from the edge atoms with cluster size.

The results of this modified model are shown in Figs. 3.2 and 3.3 as solid lines labeled "Modified Model", and they reproduce the experimental data fairly well over the complete range of cluster sizes. Above a cluster size of 4.5 nm, the clusters begin to

89

agglomerate to eventually form a Au thin film [17] so that the ratio of edge atoms to center atoms and the value of *d* both go to zero, as seen in Fig. 3.4. This is the cause of the kink in the modified model at 5.4 nm, as no separated clusters remain at that point. Hence, in the limit of large clusters, the NFs of the scattered ions reach the values associated with bulk Au.

Note that the smallest clusters that are considered in the model consist of 7 Au atoms, with 6 of them being edge atoms. It is possible to have even smaller clusters in which there are no center atoms, with the limit being a single Au adatom. It was shown in Ref. [36] that the charge on a single Au adatom on TiO_2 is 0.2 e$^-$, which is less than the charge on the nanocluster edge atoms calculated by DFT [27]. Thus, the NF in scattering from a single Au adatom would be less than that of the smallest clusters considered here. This implies the possibility that the NF could drop for extremely small cluster sizes. Such a behavior has been observed in low energy alkali ion scattering from Au and Ag nanoclusters in Refs. [48, 50, 51], and a decrease of edge atom charge for clusters that are smaller than those considered here may be the reason.

3.5 Discussion

The model presented here is based on assigning different neutralization probabilities for scattering from edge and center atoms and showing that such differences can explain why the overall NF decreases with cluster size. It uses values for NF_C measured from bulk Au but does not independently determine the NF_{EE} probabilities from experiments, first principle calculations or other methods. Nevertheless, the

90

numbers that are fit to the data do provide a good match between the model and the experiment. These values are now examined to determine if they are reasonable within the context of the general RCT process.

Figure 3.5 is a schematic diagram, used as an aid in this endeavor, which graphically shows how the energy levels of the projectiles are modified in proximity to the substrate. The horizontal axis is Z, the distance between the projectile and the surface, and the vertical axis is energy, E, where E_{vac} is the vacuum level. Both the Li and Na s levels are shown on the right side at their respective ionization energies as though they are infinitely far away and thus very sharp (not drawn to scale). As the projectiles get closer to the surface, they shift up in energy and broaden; this process is represented by curved dotted lines with arrows at the end that show the sharp s levels becoming broad Gaussian functions at their respective freezing distances (numerical values discussed below) [41]. To the left of the energy axis are colored areas representing filled levels in the surface, although the diagram does not indicate the actual density of states of those levels. $E_{Fcenter}$ and E_{Fedge} are the energies of the highest occupied levels for the center and edge atoms of the nanoclusters, respectively, which are not the same because of their different LEPs. The neutralization probability for a given scattering event would be the fraction of the broadened ionization level below the highest filled level (indicated by the horizontal dashed lines) at the freezing distance. An important thing to recognize is that magnitudes of both the shifting and the broadening can alter the neutralization probability in different directions. The freezing distances, shifting and broadening are now estimated

to see if the numbers used for the neutralization of Li^+ and Na^+ scattered from edge atoms used in the model are reasonable.
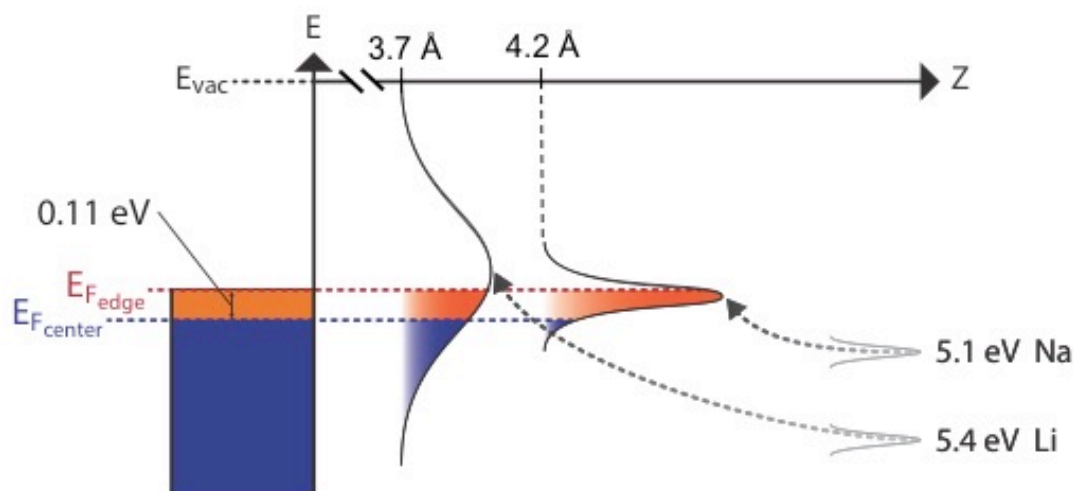
Figure 5. Schematic energy level diagram of the ion-solid system for Na and Li projectiles. Z refers to the atom-surface distance. The atomic *s* levels for Na and Li are shown at the right and labeled with their corresponding ionization energies, while the broadened and shifted ionization levels are shown at their freezing distances close to the surface (see text). The effective Fermi energies associated with the LEP above edge and center atoms are indicated by horizontal lines.

The freezing distance of the projectile is the effective maximum distance above the surface at which electrons can tunnel in and out of the ionization level. An equation from Kimmel and Cooper is used to estimate the freezing distances, which was derived by assuming that the coupling between the atom and metal decays exponentially as the atom-surface separation grows [76]. The equation contains parameters that are dependent on the particular projectile and target used. The most relevant parameter is the perpendicular component of the velocity of the scattered particle, which is calculated for Li and Na singly scattered from Au [39]. Another is the level's half width which depends

on the particular target and projectile and was determined for the Li 2*s* level in scattering from Cu(001) by Onufriev and Marston [77]. To the authors' knowledge, there are no explicit calculations for the Na 3*s* level, so that the values for Li are used to generate freezing distances for 2.0 keV Li and Na scattered from Au of 3.7 and 4.2 Å, respectively. Furthermore, it is assumed that the freezing distance for a given projectile is the same when scattering from an edge or center atom. These distances are indicated on the horizontal Z-axis in Fig. 3.5. The accuracy of these values is limited by the above-mentioned assumptions used in calculating them.

Since the freezing distance of Li is smaller than that of Na, it is possible to create a scenario that satisfies the neutralization probabilities for the two alkali ions when scattering from edge atoms in the Au nanoclusters. The purpose here, however, is not necessarily to determine the absolute value of each parameter, but to show that reasonable values can reproduce the experimental results since an inaccuracy in one number can be compensated for by changing another. For example, it is assumed in this scenario that the LEP is independent of freezing distance, as the change of LEP with Z is unknown. Although it is quite likely that the LEP is not the same at the two freezing distances, the effect of including actual LEPs can be compensated for by altering the assumed positions of E_{Fedge} and $E_{Fcenter}$ to produce the same NFs.

The Li 2*s* level is assumed to have a width of 0.14 eV at its freezing distance, while the Na 3s has a width of 0.049 eV. In addition, it is assumed that the Li 2s shifts up 0.10 eV more than Na 3s. This leads to a value of NF_E of 33% for Li and 66% for Na, which are the same as those found by fitting the model to the experimental data. The

93

neutralization values of the levels are obtained by integrating the Gaussian functions at the freezing distances down from the effective Fermi energy indicated by E_{Fedge}. Similarly, the ionization levels of Li and Na are integrated relative to the highest level for the center atoms, as defined by $E_{Fcenter}$. In order to match the NF values for ions scattered from bulk Au, which is equivalent to scattering from center atoms, $E_{Fcenter}$ must be 0.11 eV lower than E_{Fedge}. This generates NF_C = 9% and 3% for Li and Na, respectively, consistent with the experimental values for scattering from bulk Au that are used in the model.

Within the formalization of the neutralization model presented here and the standard RCT process, and using the above values for the freezing distances, the difference in the NFs of scattered Li and Na for the smaller nanoclusters are rationalized. To see if the values used for broadening and shifting of the Li and Na s levels are reasonable, they are compared to numbers obtained from theory in the literature. Nordlander and Tully calculated the shifting and broadening for Li 2s and Na 3s when scattering from a Jellium surface [78]. For Li and Na at their respective freezing distances, the calculations indicate that the broadening of the Li 2s and the Na 3s levels are 0.136 and 0.054 eV, respectively. These values are is in good agreement with the above scenario, especially considering the difference in substrates. Nordlander and Tully find that the width of the Li 2s level is a factor of 2.5 larger than the Na 3s at the freezing distances, while a Li 2s width that is a factor of 2.9 larger is needed to model the actual data. This ratio of the Li 2s and Na 3s widths is close, indicating that the model is

physically realistic, although it should be noted that the ratio of the widths is not as important as their actual magnitudes.

Nordlander and Tully coincidently calculate the same value of 4.35 eV for the level shifting at the freezing distances for both the Li $2s$ and Na $3s$, but this would not produce the observed differences in Li and Na neutralization. Therefore, there must be a small difference in the level shifting for Li and Na ions at their freezing distances. Since the Au nanocluster/oxide substrate target is much different than the Jellium surface used by Nordlander and Tully, it is not surprising that their calculations do not produce precisely correct values in this case, and the difference between the levels of 0.10 eV determined here by fitting to experimental data is relatively small. Also, considering the fact that Li has a smaller freezing distance and the shifting is modeled as an exponential, it is reasonable that the Li 2s would shift up a small amount more than Na 3s. Note that it is the difference between the levels that is important and the magnitude of that difference is implicitly set to match NF_E and NF_C for Li $2s$ and Na $3s$.

Since the Li $2s$ level in the isolated atom has a lower energy than Na $3s$, at first it may be expected that scattered Li should always have a higher NF than Na scattered from the same target. This is not the case for the small nanoclusters, however, although it is true for nanoclusters larger than 4.5 nm, as seen by comparing the experimental data in Figs. 3.2 and 3.3 and the data in Ref. [54]. Reference [54] did not, however, provide a quantitative explanation for why this is the case. To match the unexpected experimental data within the framework of the model presented here, Na must have a higher NF than Li when scattering from the edge atoms while Li must have a higher NF when scattering

from the center atoms. Such relative neutralization probabilities are produced by the model presented here.

There are other neutralization effects reported in the literature, but they would not affect the proposed model. First, a lowering of the ionization level energy is reported for projectile-target distances of less than 2.6 Å for Li scattering from HOPG [79], as opposed to the exponential upward shift used here [78]. It is calculated above that the freezing distance for Li is 3.7 Å, however, which indicates that even if such a downward level shifting did occur at those small distances, it would not affect the neutralization probability for this system. Second, the parallel component of the velocity of the exiting projectiles has been shown to have significant effects on the measured neutralization probabilities [80, 81]. Such parallel velocity effects are not important here, however, as the emission is along the surface normal.

3.6 Summary

Au nanoclusters are a nanometer-sized form of solid-state matter with a non-uniform charge distribution. Since the measured NF of alkali LEIS is the average neutralization when scattering from all of the atoms in a nanocluster, differences in the LEP above the edge and center atoms due to the charge associated with the individual atoms must be considered in interpreting the data. A parameterized model is developed here, which is based on the notions that (1) the neutralization in scattering from edge atoms is larger than for scattering from center atoms and (2) that the ratio of edge to center atoms reduces with cluster size. The modified form of the model includes inter-

nanocluster effects that act to depolarize the dipoles associated with the edge atoms when they are close to each other, and it is found to match the experimental data over all cluster sizes. This work shows how ion scattering is sensitive to the non-uniform charge distribution within a nanocluster.

With the use of the parameterized model presented here, the RCT formalization is applied to determine the level broadening, shifting, and freezing distance for Li and Na scattering from Au nanoclusters. Values for level broadening, shifting, and freezing distance are generated to verify that the neutralization probabilities calculated by the model for edge and center atoms are reasonable by comparing them to calculations [78]. These values also explain the unexpected larger neutralization probability of Na^+ compared to Li^+ when scattering from small Au nanoclusters.

A difference in the LEP between edge and center atoms in the nanoclusters is implicitly determined by experiments that measure the neutralization of scattered alkali ions as a function of cluster size. These differences are consistent with the charges on the nanoclusters atoms calculated by DFT [27, 31]. To our knowledge, no other experimental technique is able to make such a distinction. For example, STM has not been able to discern any differences in charge between atoms in a cluster partly due to the large size of the tip compared to the size of individual atoms. Kelvin force probe microscopy (KPFM) does directly measure the LEP and has seen differences at the edges of certain nanostructures [82], but its spatial resolution is even larger than that of STM. Furthermore, neither STM nor KPFM have the elemental resolution of LEIS.

Finally, this work suggests a correlation between the measured NFs and the enhanced catalytic activity of small Au nanoclusters. The measured NFs are explained by the increased positive charge of the edge atoms and how the ratio of edge to center atoms decreases with cluster size. It is also discussed above how extremely small clusters could have a reduced charge. Experiments of catalytic activity vs. cluster size show a maximum activity at a rather small cluster size [5]. Also, there is much evidence that the edge atoms that are the active sites for catalysis [27, 83-85]. Thus, it is not unreasonable to infer that both the catalytic activity and the neutralization of scattered low energy alkali ions depend on this same positive charge associated with the edge atoms.

Bibliography

[1] M. Haruta, S. Tsubota, T. Kobayashi, H. Kageyama, M.J. Genet, B. Delmon, J. Catal., **144** (1993) 175-192.

[2] M. Haruta, N. Yamada, T. Kobayashi, S. Iijima, J. Catal., **115** (1989) 301-309.

[3] A.S.K. Hashmi, G.J. Hutchings, Angew. Chem. Int. Ed., **45** (2006) 7896-7936.

[4] A. Sanchez, S. Abbet, U. Heiz, W.D. Schneider, H. Hakkinen, R.N. Barnett, U. Landman, J. Phys. Chem. A, **103** (1999) 9573-9578.

[5] T.V. Choudhary, D.W. Goodman, Top.1 Catal., **21** (2002) 25-34.

[6] A. Gupta, D.F. Moyano, A. Parnsubsakul, A. Papadopoulos, L.-S. Wang, R.F. Landis, R. Das, V.M. Rotello, ACS Appl. Mater. Interfaces, **8** (2016) 14096-14101.

[7] S.J. Kazmi, M.A. Shehzad, S. Mehmood, M. Yasar, A. Naeem, A.S. Bhatti, Sensors and Actuators A, **216** (2014) 8.

[8] V.N. Antonov, P. Swaminathan, J.A.N.T. Soares, J.S. Palmer, J.H. Weaver, Appl. Phys. Lett., **88** (2006) 121906.

[9] X. Lai, D.W. Goodman, J. Mol. Catal. A: Chem., **162** (2000) 33-50.

[10] C. Zhang, A. Michaelides, D.A. King, S.J. Jenkins, J. Am. Chem. Soc., **132** (2010) 2175-2182.

[11] U. Hejral, D. Franz, S. Volkov, S. Francoual, J. Strempfer, A. Stierle, Phys. Rev. Lett., **120** (2018) 126101.

[12] D. Kong, G. Wang, Y. Pan, S. Hu, J. Hou, H. Pan, C.T. Campbell, J. Zhu, Phys. Chem. C, **115** (2011) 6715-6725.

[13] M. Valden, X. Lai, D.W. Goodman, Science, **281** (1998) 1647-1650.

[14] L. Huang, S.J. Chey, J.H. Weaver, Phys. Rev. Lett., **80** (1998) 4095-4098.

[15] E. Gross, M. Asscher, Langmuir, **26** (2010) 16226-16231.

[16] L. Sungsik, F. Chaoyang, T. Wu, S.L. Anderson, Surf. Sci., **578** (2005) 5-19.

[17] X. Lai, T.P.S. Clair, M. Valden, D.W. Goodman, Prog. Surf. Sci., **59** (1998) 25-52.

[18] K.J. Taylor, C.L. Pettiette‑Hall, O. Cheshnovsky, R.E. Smalley, J. Chem. Phys., **96** (1992) 3319-3329.

[19] R. Galhenage, H. Yan, S.A. Tenney, N. Park, G. Henkelman, P. Albrecht, D.R. Mullins, D.A. Chen, J. Phys. Chem. C, **117** (2013) 7191−7201.

[20] E. Kadossov, S. Cabrini, U. Burghaus, J. Mol. Catal. A: Chem., **321** (2010) 101-109.

[21] C. Xu, W.S. Oh, G. Liu, D.Y. Kim, D.W. Goodman, J. Vac. Sci. Technol. A, **15** (1997) 1261-1268.

[22] E. Kadossov, J. Justin, M. Lu, D. Rosenmann, L.E. Ocola, S. Cabrini, U. Burghaus, Chem. Phys. Lett., **483** (2009) 250-253.

[23] M. Mavrikakis, P. Stoltze, J.K. Nørskov, Catal. Lett., **64** (2000) 101-106.

[24] N. Lopez, T.V.W. Janssens, B.S. Clausen, Y. Xu, M. Mavrikakis, T. Bligaard, J.K. Nørskov, J. Catal., **223** (2004) 232-235.

[25] T.V. Choudhary, D.W. Goodman, App. Cat. A: General, **291** (2005) 32-36.

[26] A. Cho, Science, **299** (2003) 1684-1685.

[27] L.B. Vilhelmsen, B. Hammer, ACS Catalysis, **4** (2014) 1626-1631.

[28] R. Narayanan, M.A. El-Sayed, Nano Lett., **4** (2004) 1343-1348.

[29] B. Roldan Cuenya, F. Behafarid, Surf. Sci. Rep., **70** (2015) 135-187.

[30] E. Farfan-Arribas, J. Biener, C.M. Friend, R.J. Madix, Surf. Sci., **591** (2005) 1-12.

[31] S. Hong, T.S. Rahman, J. Am. Chem. Soc., **135** (2013) 7629-7635.

[32] X. Yu, L. Xu, W. Zhang, Z. Jiang, J. Zhu, W. Huang, Chin. J. Chem. Phys., **22** (2009) 339-345.

[33] B.K. Min, W.T. Wallace, D.W. Goodman, Surf. Sci., **600** (2006) L7-L11.

[34] T. Minato, T. Susaki, S. Shiraki, H.S. Kato, M. Kawai, K. Aika, Surf. Sci., **566–568** (2004) 1012-1017.

[35] L. Zhang, R. Persaud, T.E. Madey, Phys. Rev. B, **56** (1997) 10549-10557.

[36] Z. Zhang, W. Tang, M. Neurock, J.T. Yates Jr., J. Phys. Chem. C, **115** (2011) 23848-23853.

[37] T. Okazawa, M. Fujiwara, T. Nishimura, T. Akita, M. Kohyama, Y. Kido, Surf. Sci., **600** (2006) 1331-1338.

[38] D.P. Smith, J. Appl. Phys., **38** (1967) 340-347.

[39] W.J. Rabalais, *Principles and applications of ion scattering spectrometry : surface chemical and structural analysis*, Wiley, New York, 2003.

[40] R. Carmina Monreal, Prog. Surf. Sci., **89** (2014) 80-125.

[41] J. Los, J.J.C. Geerlings, Phys. Rep., **190** (1990) 133-190.

[42] A.G. Borisov, J.P. Gauyacq, Surf. Sci., **445** (2000) 430-447.

[43] J.A. Yarmoff, C.B. Weare, Nucl. Instrum. Methods B, **125** (1997) 262-267.

[44] Y. Yang, Z. Sroubek, J.A. Yarmoff, Phys. Rev. B, **69** (2004) 045420.

[45] E.R. Behringer, D.R. Andersson, B.H. Cooper, J.B. Marston, Phys. Rev. B, **54** (1996) 14765-14779.

[46] L.Q. Jiang, Y.D. Li, B.E. Koel, Phys. Rev. Lett., **70** (1993) 2649-2652.

[47] C.B. Weare, J.A. Yarmoff, J. Vac. Sci. Technol. A, **13** (1995) 1421-1425.

[48] A.R. Canario, V.A. Esaulov, J. Chem. Phys., **124** (2006) 224710.

[49] G.F. Liu, Z. Sroubek, J.A. Yarmoff, Phys. Rev. Lett., **92** (2004) 216801.

[50] J. Shen, J. Jia, K. Bobrov, L. Guillemot, V.A. Esaulov, Gold Bull., **46** (2013) 343-347.

[51] J. Shen, J. Jia, K. Bobrov, L. Guillemot, V.A. Esaulov, J. Phys. Chem. C, **119** (2015) 15168-15176.

[52] S. Balaz, J.A. Yarmoff, J. Phys. Condens. Matter, **22** (2010) 084009.

[53] S. Balaz, J.A. Yarmoff, Surf. Sci., **605** (2011) 675-680.

[54] G.F. Liu, Z. Sroubek, P. Karmakar, J.A. Yarmoff, J. Chem. Phys., **125** (2006) 054715.

[55] C.R. Salvo, J.A. Yarmoff, Langmuir, **33** (2017) 5439-5445.

[56] A.R. Canário, V.A. Esaulov, J. Chem. Phys., **124** (2006) 224710.

[57] G.C. Bond, D.T. Thompson, Cat. Rev. - Sci. Eng., **41** (1999) 319-388.

[58] R.S. Gao, P.S. Gibner, J.H. Newman, K.A. Smith, R.F. Stebbings, Rev. Sci. Instrum., **55** (1984) 1756-1759.

[59] B.L. Peko, T.M. Stephen, Nucl. Instrum. Methods B, **171** (2000) 597-604.

[60] J. Oberheide, P. Wilhelms, M. Zimmer, Meas. Sci. Technol., **8** (1997) 351-354.

[61] J.C. Davies, B.E. Hayden, D.J. Pegg, M.E. Rendall, Surf. Sci., **496** (2002) 110-120.

[62] I.E. Wachs, K. Routray, ACS Catalysis, **2** (2012) 1235-1246.

[63] H. Niehus, W. Heiland, E. Taglauer, Surf. Sci. Rep., **17** (1993) 91.

[64] G.A. Kimmel, B.H. Cooper, Phys. Rev. B, **48** (1993) 12164-12177.

[65] C.B. Weare, K.A.H. German, J.A. Yarmoff, Phys. Rev. B, **52** (1995) 2066-2069.

[66] E. Kneedler, A.B. Andrews, W.-K. Choi, S.D. Kevan, Phys. Rev. B, **51** (1995) 1823-1829.

[67] C.B. Weare, J.A. Yarmoff, Surf. Sci., **348** (1996) 359-369.

[68] L.Q. Jiang, Y.D. Li, B.E. Koel, Phys. Rev. Lett., **70** (1993) 2649-2652.

[69] A. Inberg, E. Glickman, T. Asher, N. Fishelson, Y. Shacham-Diamand, Surf. Coat. Technol., **204** (2009) 520-524.

[70] J. Radnik, C. Mohr, P. Claus, Phys. Chem. Chem. Phys., **5** (2003) 172-177.

[71] T. Risse, S. Shaikhutdinov, N. Nilius, M. Sterrer, H.J. Freund, Acc. Chem. Res., **41** (2008) 8.

[72] P. Karmakar, G.F. Liu, Z. Sroubek, J.A. Yarmoff, Phys. Rev. Lett., **98** (2007) 215502.

[73] C.S. Chang, U. Knipping, I.S.T. Tsong, Nucl. Instrum. Methods B, **18** (1986) 11-15.

[74] H.Q. Shi, R. Asahi, C. Stampfl, Phys. Rev. B, **75** (2007) 205125.

[75] J. Paul, J. Vac. Sci. Technol. A, **5** (1987) 664-670.

[76] G.A. Kimmel, B.H. Cooper, Phys. Rev. B, **48** (1993) 12164-12177.

[77] A.V. Onufriev, J.B. Marston, Phys. Rev. B, **53** (1996) 13340-13356.

[78] P. Nordlander, J.C. Tully, Phys. Rev. B, **42** (1990) 5564-5578.

[79] F. Bonetto, M.A. Romero, E.A. Garcia, R.A. Vidal, J. Ferron, E.C. Goldberg, Phys. Rev. B, **78** (2008) 075422.

[80] L. Gao, Y. Zhu, Y. Shi, P. Liu, Y. Xiao, G. Li, Y. Liu, V.A. Esaulov, X. Chen, L. Chen, Y. Guo, Phys. Rev. A, **96** (2017) 052705.

[81] J.N.M. Van Wunnik, R. Brako, K. Makoshi, D.M. Newns, Surf. Sci., **126** (1983) 618-623.

[82] L. Sangyeob, S. Aniketa, R. Regina, Nanotechnology, **20** (2009) 035701.

[83] M.J. Walsh, P.L. Gai, E.E. Boyes, J. Phys. Conf. Ser., **371** (2012) 1-4.

[84] Y.-G. Wang, D.C. Cantu, M.-S. Lee, J. Li, V.-A. Glezakou, R. Rousseau, J. Am. Chem. Soc., **138** (2016) 10467-10476.

[85] S. Arrii, F. Morfin, A.J. Renouprez, J.L. Rousset, J. Am. Chem. Soc., **126** (2004) 1199-1205.

Chapter 4 Adsorption of Br$_2$ onto Small Au Nanoclusters

4.1 Introduction

The adsorption of a species onto a solid surface is a fundamental, and usually the first, step in many chemical and physical processes, particularly in applications such as catalysis [1], etching [2, 3] and chemical vapor deposition [4]. Here, the dissociative adsorption of Br2, is shown to occur strongly in the presence of small Au nanoclusters deposited on an oxide substrate, but not with bulk metal nor on the bare substrate. Small metal nanoclusters supported on oxides are extremely effective nanocatalysts, with rates that rival those of enzymes in biological systems [5]. This result thus provides a glimpse into how metal nanoclusters promote the adsorption of precursor species at the beginning of the chemical reaction process. In addition, Br2 is known to poison catalysis with nanoclusters [6], so that an understanding of its adsorption also reveals information about the inner workings of the catalysis mechanism.

The surfaces are investigated primarily with low energy ion scattering (LEIS) in two different modes. First, LEIS spectra reveal the distribution of elements at the surface [7]. Second, a novel application of LEIS in which the neutralization of scattered alkali ions is measured provides information on the surface electronic properties of the nanoclusters. The neutralization is sensitive to the local electrostatic potential (LEP) on a solid surface a few Å's above the target atom [8, 9] and has been applied to scattering

from clean metals [10-12], adsorbates on metals and semiconductors [8, 13, 14] and metal nanoclusters [15-20].

For nanoclusters deposited on oxide substrates, the neutralization probability is particularly sensitive to the size of the clusters in that it is high for the smallest clusters produced and decreases as the clusters grow larger [15-18]. In recent work, we proposed that the high neutralization is due to the fact that the low coordinated edge atoms of the nanoclusters are positively charged, while the center atoms are nearly neutral [21]. The positively charge creates upward pointing dipoles that decrease the local electrostatic potential (LEP) above the edge atoms causing a higher neutralization probability for alkali ions scattered from those atoms. In contrast, the ions that scatter from center atoms have a low neutralization probability due to the high work function of neutral Au. Since the ratio of the number of edge atoms to center atoms decreases with cluster size, the overall neutralization probability decreases with cluster size. In addition, it has been shown that the edge atoms are the active sites for chemisorption during catalytic reactions involving nanoclusters [22], so there is likely a relationship between the charge state of these edge atoms and their ability to promote catalytic surface reactions.

The adsorption of Br_2 molecules onto a solid is a dissociative process that involves the scission of the Br-Br bond and thus requires a reactive surface [23]. The fact that dissociative adsorption readily occurs on small Au nanoclusters, while it does not occur on the bare substrate nor readily on the bulk metal, indicates that the nanoclusters are directly involved in the Br-Br bond cleavage, which is related to the catalytic behavior of small Au nanoclusters. This work shows that the average LEP above the Au

atoms decreases in the presence of adsorbed Br. This leads to the conclusion that Br_2 dissociatively chemisorbs by forming ionic bonds to the positive edge atoms producing downward pointing dipoles that reduce the neutralization of ions scattered from those atoms. The fact that Br forms such bonds suggests that the charge state of the atoms in a nanocatalyst plays a role in the adsorption step of surface chemical reactions involving nanoclusters.

4.2 Experimental Procedure

The experiments are conducted with the sample held at room temperature in an ultra-high vacuum (UHV) chamber that has a base pressure less than $1x10^{-9}$ Torr. The Si(111) substrate is mounted on the foot of an XYZ rotary manipulator, and is electrically isolated so that current can be run directly through the wafer for resistive heating. There is a load-lock chamber and sample transfer system attached to the chamber so that new samples can be quickly introduced for each measurement without breaking vacuum in the main sample preparation and analysis chamber. The main chamber includes equipment for performing time-of-flight (TOF) LEIS, low energy electron diffraction (LEED) and x-ray photoelectron spectroscopy (XPS).

The substrate is $5x5x1$ mm^3 single crystal Si(111) wafer (*n*-type, 5-10 Ω cm) onto which a SiO_2 film is grown *in situ*. After insertion into the UHV chamber, the Si samples are initially degassed by running 0.5 A through them (roughly 250°C) for a minimum of 30 min to remove adsorbed water and hydrocarbons. The native oxide layer and any more strongly bound contaminants are then removed by "flashing" the sample with 9 A. This

value is chosen by systematically increasing the current and monitoring the O 1s peak with XPS after flashing until there is no longer any oxygen signal present. The surfaces cleaned in this manner show no contamination with XPS and display clear 7x7 LEED patterns [24]. The oxide layer is then grown by heating the sample to approximately 700°C under $2x10^{-5}$ Torr of flowing O_2 for 30 min, which produces a uniform thermal oxide layer [25]. Note that the sample is cooled with the O_2 still present to avoid the formation of pinholes in the film [26]. XPS is used to confirm the growth of the SiO_2 layer and provide its thickness.

Au is deposited onto the sample via evaporation from a heated tungsten filament (Mathis) with Au wire (99.99%) wrapped around it. The Au coverage is calculated by calibrating the deposition rate using a quartz crystal microbalance (QCM) with the assumption that 1 ML of Au corresponds to a single atomic layer of Au(111) with a density of 19.3 g/cm^3, which has a height of 2.6 Å [27]. The reported amounts of deposited Au correspond to what the thickness of a Au film would be if it grew in a layer-by-layer mode. Since it actually forms nanoclusters, however, the coverage values are useful as a guide to the amount of Au that is deposited, but are not directly related to the thickness of the clusters.

Br_2 molecules are produced from a solid-state electrochemical cell based on a AgBr pellet affixed to Ag foil [28, 29]. The exposures are given in units of μA-min, which refers to the integrated current run through the cell. It had been previously reported that a 10 μA-min exposure corresponds approximately to 1 molecule impacting each

surface atom [30], but that estimate is very dependent on the specific cell parameters and geometry. No detailed calibration of the exposure was possible in the present setup.

XPS measurements are made using a Riber CX 700 with a Mg K_α (1253 eV) x-ray source and line width of 1.10 eV. A cylindrical mirror analyzer (CMA) with adjustable resolution is used to measure the energy distribution of the emitted photoelectrons. The XPS spectra presented here were collected with a 3.0 eV resolution energy.

TOF-LEIS was performed with 1.5 keV Na^+ alkali ions. The Na^+ ions are generated from a thermionic emission source (Kimball Physics) and incident at 30° degrees to the surface normal. The beam is pulsed at 80 kHz by deflecting it across a 1 mm diameter aperture mounted in front of the gun. The particles emitted along the surface normal, which are scattered at a 150° angle, are collected by a triple microchannel plate (MCP) array located at the end of the 0.43 m long flight leg. Deflection plates mounted in the leg are used to distinguish between scattered neutral and charged particles. With both plates grounded, all of the particles pass through to the detector, but only the neutral particles pass when 400 V is placed across the plates. "Total" and "neutral" yield TOF spectra are collected by switching the deflection plate voltage on and off every 60 s during the approximately 15 min it takes to collect a spectrum to avoid any effects of long term drift in the ion beam current. The entrance to the MCP is held at ground potential so that they are equally sensitive to charged and neutral particles, but there is a decrease in absolute sensitivity as the kinetic energy of the scattered projectiles falls below about 1 keV [31].

4.3 Results

Figure 4.1 shows XPS spectra used to confirm the sample cleanliness and monitor the presence of Au and Br. Spectrum (a) was collected after exposing clean Si(111) to 60 μA min of Br_2, and a clear Br 3d peak is visible. This is expected since Br readily adsorbs on clean Si [23, 32]. Spectrum (b) was collected from SiO_2 grown on Si(111), which confirms the cleanliness of the sample and enables a measurement of the SiO_2 film thickness. The thickness is determined from the ratio of the SiO_2 to the bulk Si 2p component in a high-resolution Si 2p spectrum (not shown) to be approximately 0.7 nm using 2.5 nm for the photoelectron escape depth [25]. Spectrum (c) was collected after 0.30 ML of Au was deposited onto the SiO_2, which is a coverage that forms Au nanoclusters [33], and it shows no features other than those indicative of Si, O and Au. The final spectrum (d) was collected after exposure of the Au nanocluster covered-surface to 40 μA min of Br_2. Note that there is a small feature near the position of the Br 3d peak, but it is also present in the spectrum collected before Br_2 exposure and is likely a satellite feature associated with the Au 4f level that is commonly seen in XPS due to a small amount of higher energy x-rays that are emitted by the Mg K_α source. If there were any Br 3d signal, it would be negligible because there is only a submonolayer coverage of Br and XPS is not surface sensitive enough to reveal such a small amount.
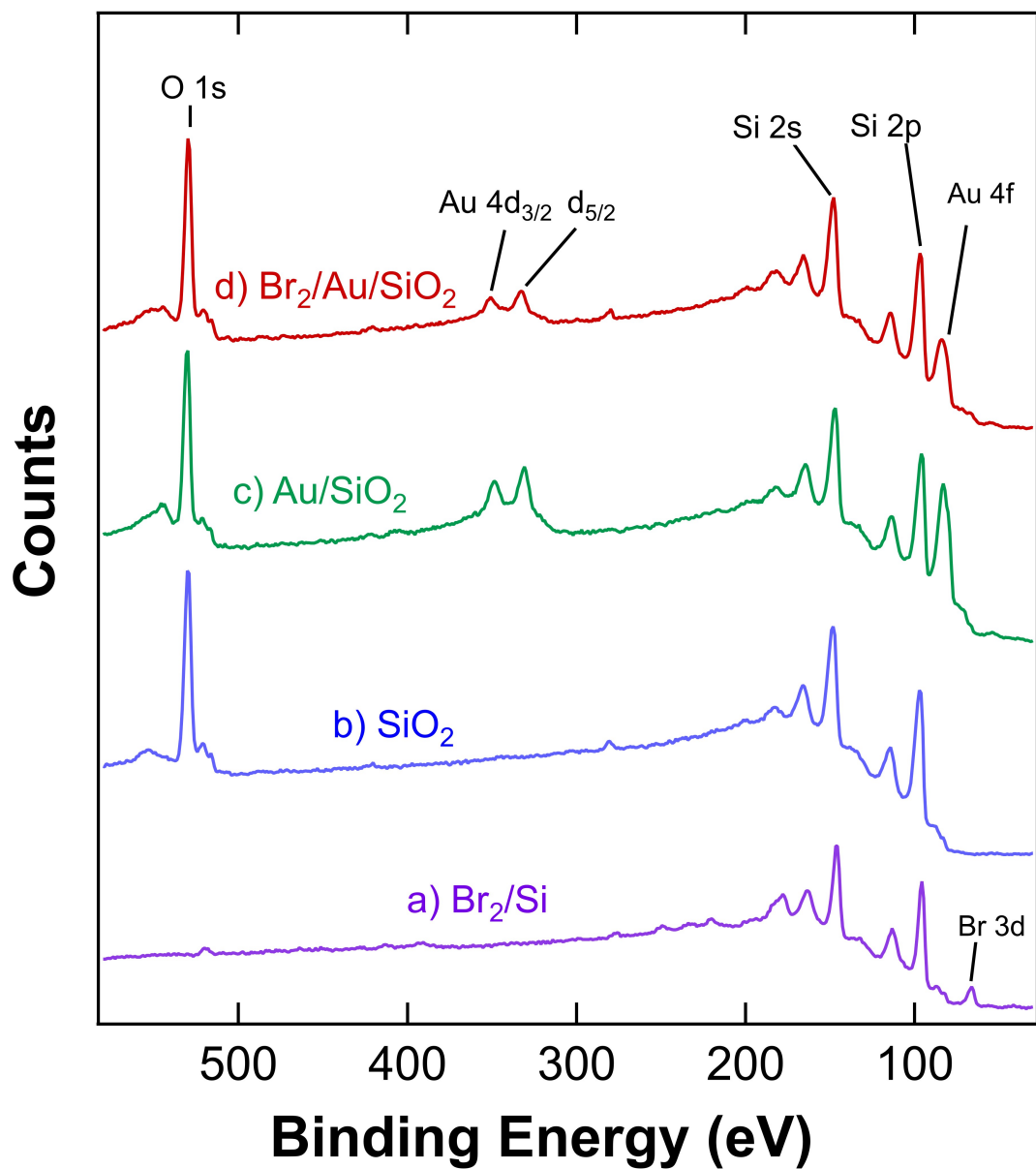
Figure 4.1 Typical XPS spectra collected from (a) Si(111) exposed to 40 μA min of Br$_2$, (b) thermally prepared SiO$_2$ (see text), (c) 0.30 ML Au deposited onto SiO$_2$, and (d) that surface exposed to 60 μA min of Br$_2$. A vertical line on the right side indicates the position of the Br 3d peak.

LEIS is an extremely surface sensitive technique [11], even more so than XPS. This is due to shadowing and blocking [34, 35], which effectively only allows projectiles that are singly scattered from the first few layers to be detected, although multiply scattered projectiles can probe deeper into the material. The role of shadowing and blocking for a particular surface depends on the geometry of the setup and the crystal structure, so that the depth sensitivity is system dependent. Specifically, when Na^+ scatters from Au nanoclusters, single scattering in LEIS is found to only probe the outermost layer of Au atoms in each cluster [21].

Figure 4.2 shows representative TOF-LEIS spectra of the total scattered yield collected from three different samples. The spectra show single scattering peaks (SSPs), which are used as an indication of the surface composition. Single scattering occurs when a projectile undergoes a hard binary collision with a surface target atom and scatters directly into the detector [11, 36]. The energy of the scattered projectile can be calculated classically considering only conservation of energy and momentum in an elastic collision with an unbound target atom, which predicts that Na will scatter from the heavier Au atoms with a higher energy than when scattered from Br. Note that there is also some energy lost to inelastic processes, but the amount is small compared to the elastic energy loss.

The bottom spectrum in Fig. 4.2 was collected following exposure of clean SiO_2 to Br_2. The absence of Si and O SSPs is expected because their masses are too small to produce singly scattered Na at a 150° angle with a large enough energy to be detected. Na scattered from Br does have enough energy to be detected, however, so that the absence

of a Br SSP in the spectrum indicates that Br_2 does not stick to SiO_2. XPS spectra collected from this sample (not shown) also had no Br signal. The inertness of SiO_2 to Br_2 adsorption is presumably because the amorphous oxide surface does not have reactive sites that can break the halogen-halogen molecular bond.

The middle spectrum in Fig. 4.2 was collected from clean Si(111) exposed to 60 μA min of Br_2. The SSP from Br is clearly seen at 496 eV, indicating that Br readily adsorbs on clean Si(111), consistent with the XPS results described above and reports in the literature [23, 32, 37]. The dangling bonds on clean Si(111)-7x7 provide the reactive sites that break the Br-Br bonds and lead to dissociative chemisorption.

The top spectrum in Fig. 4.2 was collected from Au nanoclusters on SiO_2 following Br_2 exposure. The sample was prepared by deposition of 0.19 ML Au onto SiO_2, which is a coverage that produces active nanoclusters, and then exposing it to 40 μA min of Br_2. Although the Br SSP signal is much smaller than for brominated Si, it is clearly visible. The strongest peak in the spectrum is at 968 eV, which is the Au SSP. Note that the MCP sensitivity and differential cross section must be considered when comparing the relative sizes of the SSPs to determine the absolute amount of adsorbed Br, as quantified below.
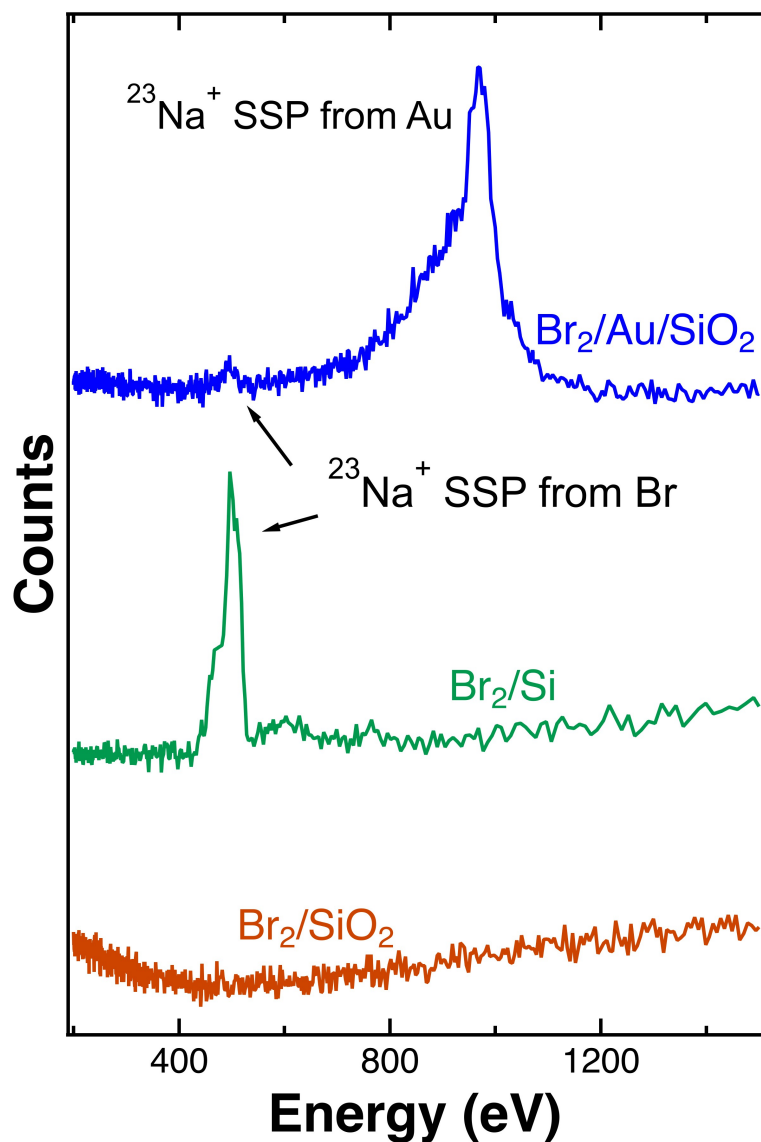
Figure 4.2 Typical TOF LEIS spectra collected using 1.5 keV Na$^+$ projectiles. The Au and Br SSPs are indicated when present. The three spectra were collected after a 30 μA min Br$_2$ exposure of a SiO$_2$ film, clean Si(111)-7x7, and 0.53 ML Au deposited on SiO$_2$.

In addition, a polycrystalline Au foil was cleaned by Ar$^+$ ion sputtering and then

exposed to Br$_2$. This foil showed no evidence of Br adsorption with XPS and a very small

Br SSP in LEIS (not shown) that indicates approximately 1 Br adatom per 200 Au surface atoms (the method used for this calculation is described below). This implies that polycrystalline Au is largely inert to reaction with Br_2. Although there are reports of Br_2 adsorption in vacuum on Au(100), which has an unusual 5x20 surface unit cell [38, 39], there are, to our knowledge, no reports of Br_2 adsorption on other signal crystal faces or on poly-crystalline Au. There are, however, reports of Cl_2 and I_2 chemisorption on Au(111) [40, 41].

The intensities of the SSPs in the total yield spectra are used to determine the surface coverages of Br and Au. Each SSP is integrated following subtraction of the multiple scattering background, as described elsewhere [8]. The uncertainty in each SSP area is assumed to be purely statistical so that the error bars are set to the square root of all the counts, including the background. When comparing the Br and Au SSPs, corrections also need to be made to account for their relative sensitivities. First, the MCP sensitivity of singly scattered Na depends on the scattered energy, which depends on the mass of the target atom. The values for the MCP efficiency at the energies used here are 0.30±0.01 and 0.50±0.01 for the Br and Au SSPs, respectively [31]. Second, Na scattered from Br and Au have different scattering cross sections, which are determined using Thomas-Fermi theory [42]. Such a calculation shows that the differential cross section for 1.5 keV Na scattered at 150° from Au is 2.15 times larger than for scattering from Br. Thus, when reporting the ratio of Br to Au, the raw ratios of the integrated SSP areas are multiplied by 3.58 to compensate for the differences in the MCP sensitivities and differential cross sections.

It is well established that Au deposited onto SiO_2 forms nanoclusters rather than a dispersed film [18, 33]. The growth of nanoclusters by direct deposition on an oxide surface produces a narrow range of cluster sizes, and the average size increases as more Au is deposited [33, 43]. The amount of Au deposited is converted to the average diameter of the nanoclusters using STM data from the literature for Au deposited on TiO_2 [43].

Figure 4.3 plots the ratio of Br to Au atoms at the surface of the nanoclusters as a function of the diameter of the clusters following exposures to 30 and 40 μA min of Br_2. The ratio is generated by dividing the integrated Br and Au SSP's from the same TOF total yield spectrum and correcting for the MCP sensitivities and scattering cross sections. The error bars are calculated by propagating the statistical error determined for each individual SSP.

The inset in Fig. 4.3 shows the ratio of surface Br to Au as a function of Br_2 exposure for a fixed Au coverage of 0.30 ML, which corresponds to a 3.0 nm average cluster diameter. The data initially increases linearly showing that the sticking coefficient is constant until Br occupies all of the adsorption sites. At this point, no more Br_2 sticks and the surface coverage saturates. For 0.30 ML of Au, this occurs around 50 μA min. Although the saturation level is likely to be dependent on the nanocluster size, a 50 uA min exposure is assumed to be sufficient to attain saturation for the range of cluster sizes studied here.
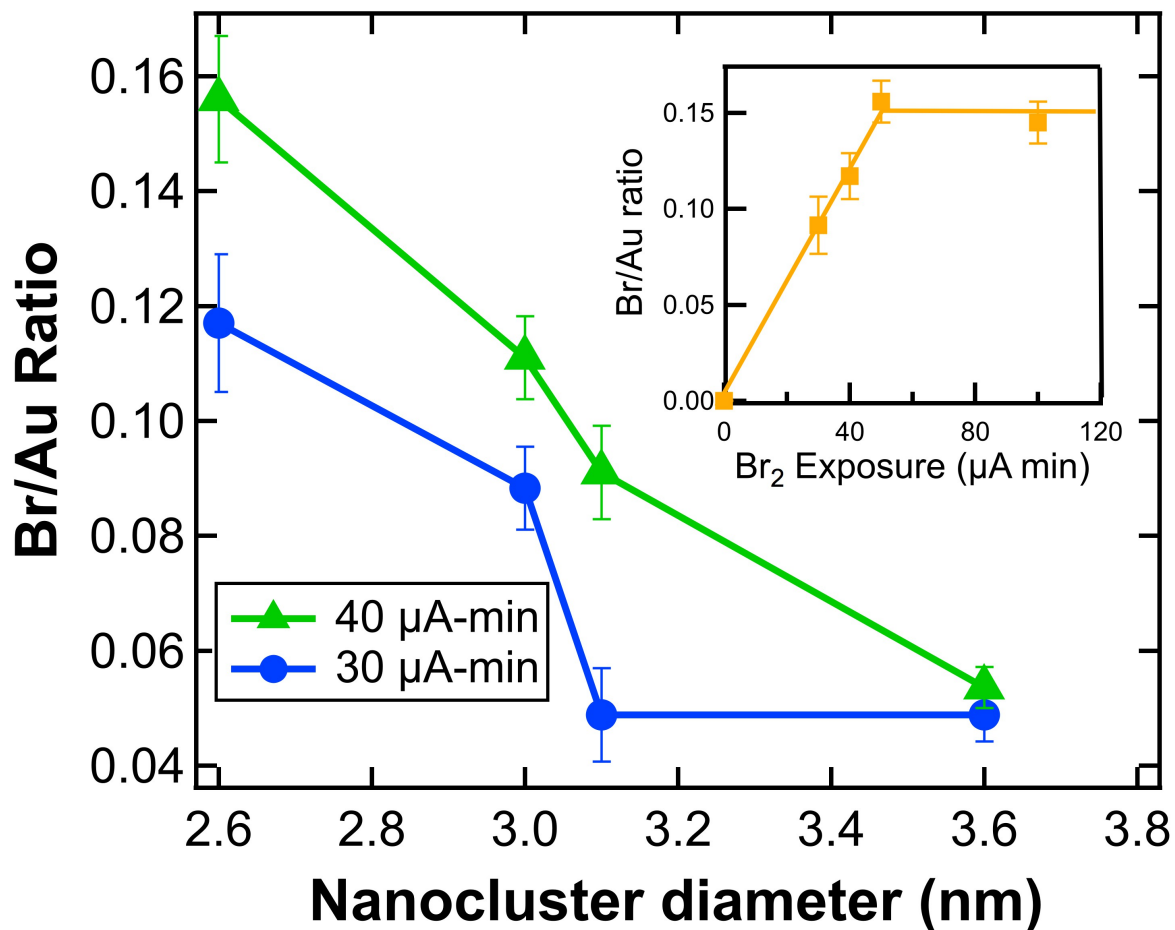
Figure 4.3 The ratio of the total yield Br and Au SSPs shown as a function of the average Au nanocluster diameter on SiO_2. The data were normalized by the sensitivity of the MCP and the scattering cross sections. Inset: The ratio of the Br and Au SSPs of scattered 1.5 keV Na^+ shown as a function of Br_2 exposure for 0.30 ML of Au on SiO_2, which forms 3.0 nm diameter Au clusters.

To determine the neutralization probability, i.e. the neutral fraction (NF), of Na^+ singly scattered from Au, the integrated SSP of the neutral yield spectrum is divided by that from the total yield spectrum. The neutralization probability depends on the LEP at a particular distance that the projectile is above the target atom along the exit trajectory, the ionization level of the projectile, and the kinetic energy and exit angle of the scattered particle [10, 13]. When a projectile approaches a surface, its ionization level shifts up as it sees its image charge in the surface. At the same time, the sharp s level in the alkali projectile begins to hybridize with orbitals in the surface causing the atomic level to broaden [12, 44]. The overlap between the broadened s level and the filled states in the surface allow electrons to tunnel back and forth once the projectile is close enough to the surface. Because the velocity of the projectile is large compared to the electron-tunneling rate, the interaction occurs non-adiabatically and the charge distribution of the scattered projectiles is determined along the exit trajectory at a "freezing" point that is typically a few Å above the surface [45, 46]. This distribution is measured as the NF of the scattered alkali projectiles, which increases as the LEP decreases and vice versa.

When scattering from a homogeneous surface, such as a clean metal, the LEP is the same everywhere so that alkali projectiles scattered from any surface site will have the same NF, and it can be calculated using the global surface work function [47]. If the surface LEP is inhomogeneous, however, then the NF for a particular scattering event depends on the LEP above the target atom, which is sometimes referred to as the local work function. This point is clearly illustrated in TOF LEIS measurements from metal surfaces with alkali adsorbates [8]. When an alkali atom adsorbs onto a metal it creates a

117

local upward pointing dipole at the adatom causing the LEP above that site to decrease from that of the surrounding surface. When using alkali LEIS, it is thus possible to explicitly differentiate the NF of the adsorbate and substrate by their scattered energies [8, 48]. It was found that alkali ions scattered from alkali adatoms have a larger NF than for scattering from the substrate when the coverage is small.

A recent report from this group [21] agrees with work from the literature in that the clusters contain positively charged Au atoms [49-53], although others have concluded that the clusters are overall negatively charged [54-57]. It was calculated from density functional theory (DFT) that the edge atoms of a nanocluster are positively charged [53, 58] and thus create upward pointing dipoles. These upward pointing dipoles create a lower LEP, as with alkali adatoms, which raises the NF of the scattered projectiles. The center atoms are near neutral so that alkali ions scattered from them have the low NF associated with scattering from Au metal. The average NF obtained from a LEIS spectrum is thus larger than for scattering from bulk Au due to reduced LEP above the edge atoms. Because the ratio of edge to center atoms decreases with cluster size, the NF also decreases with size. The reduction of the NF of the scattered alkali ions with cluster size is thus an indication that the edge atoms are positively charged.

Figure 4.4 shows the NF as a function of Br_2 exposure for different amounts of Au deposition. As expected, in the absence of Br the NF is highest for the smallest clusters, and goes down as the cluster size increases with further Au deposition [16, 18]. For all of the Au cluster sizes, the NF decreases as more Br_2 is adsorbed. Note that the actual Br coverage could not be calculated for a 0.19 ML coverage Au because the Br

SSP was too small. As seen in Fig. 4.4, however, the data show a significant drop in NF with Br_2 exposure, thus indicating that Br adsorbs even on these smallest nanoclusters. In addition, the NF does not decrease significantly beyond the limits set by the error bars after a Br_2 exposure of 40 μA min, indicating that such an exposure is close to saturation coverage.
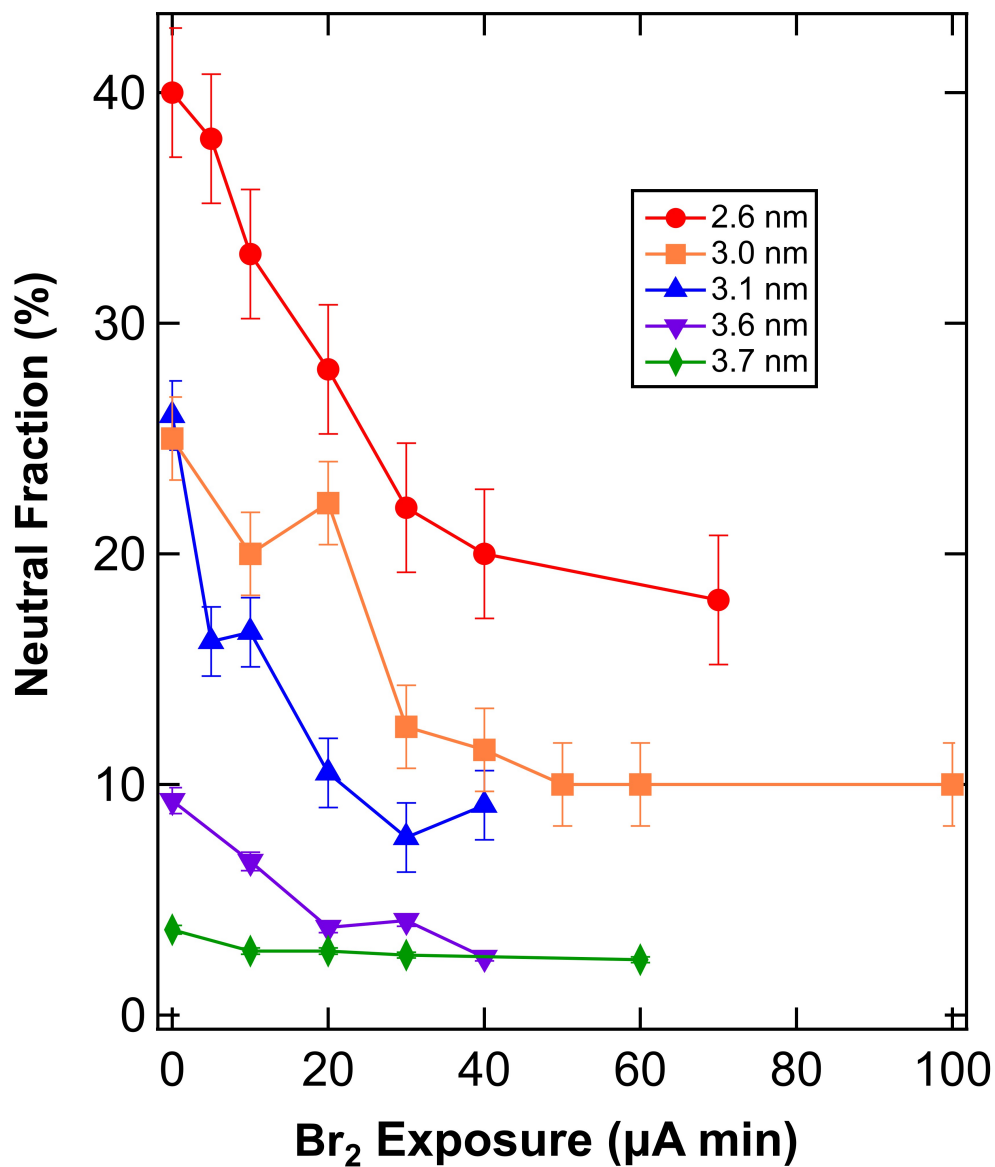
Figure 4.4 The neutral fractions of the singly scattered projectiles for 1.5 keV Na^+ scattered from Au nanoclusters on SiO_2 with the indicated average diameters shown as a function of Br_2 exposure.

4.4 Discussion

With the use of Fig. 4.3, estimates of the number of Br atoms per nanocluster and per edge atom are made and provided in Table 1. The accuracy of this calculation is limited by a few factors. For example, differences in the cluster formation process between the SiO_2 substrate used in the present experiment versus the TiO_2 substrate used by Lai *et al.* can affect the cluster sizes calculated here. Although the two substrates are different, however, it was shown that the average cluster size formed on SiO_2 and TiO_2 are very similar for 0.20 ML of deposited Au [59]. Also, the accuracy of the QCM calibration of the deposition rate can lead to a systematic error.

Table 4.1 shows that the number of Br adatoms is much smaller than the number of Au atoms at the surfaces of the nanoclusters. This implies that Br does not completely cover the nanoclusters in the same way that it covers a Si(111) surface exposed to Br_2 [23]. One explanation for the very small amount of Br adsorption is that the atoms only attach at the edges of the clusters, consistent with the current consensus that adsorption in catalytic reactions occurs at the edges [60-64].

The data in Table 4.1 shows that the total number of Br atoms adsorbed per cluster is relatively constant for clusters with average diameters in the range of 2.6 to 3.6 nm. Lemire *et al.* found that for 2 nm diameter Au nanoclusters on FeO(111), 5 CO molecules adsorb per nanocluster and do so at the low coordinated Au edge atoms [64]. As calculated in Table 1, between 7 and 10 Br atoms adsorb per nanocluster for 0.19 to 0.79 ML of Au. Since the number of CO molecules is comparable to that of Br atoms per nanocluster, it can be assumed that the Br atoms occupy the same edge sites as adsorbed

CO. A drop off in the dipole strength of the nanocluster edge atoms occurs with 1.10 ML

of Au due to inter-nanocluster effects that occur when the clusters are close to each other,

as discussed previously [21], thereby reducing the amount of Br that adsorbs.

Au deposited (ML)	0.19	0.30	0.53	0.79	1.10
Br exposure (µA min)	40	40	40	40	60
Average nanocluster diameter (nm)	2.6±0.2	3.0±0.2	3.1±0.2	3.6±0.2	3.7±0.2
Average outermost Au atoms per cluster	58.9±9.5	75.1±14.2	81.0±14.0	113±13.0	119±13.0
Average Br atoms per cluster	9.2±1.6	10.4±1.4	7.3±0.7	7.3±1.0	3.4±0.6
Average edge Au atoms	27.2±2.1	33.5±2.1	34.6±2.1	39.8±2.1	42.0±2.1
Average Au edge atom per Br atom	3.0±0.9	3.2±0.9	4.7±0.8	5.5±0.9	12±0.9
Au surface coverage	13±2%	20±2%	24±3%	40±4%	43±4%
Br surface coverage	2.0±0.2%	2.8±0.2%	2.4±0.3%	2.6±0.4%	1.2±0.1%

Table 4.1 The Au surface coverages, Br_2 exposures, cluster sizes, number of outermost Au and edge atoms per cluster and coverages of Br determined from the LEIS data. The cluster sizes and number of edge atoms were determined from Ref. [43] (see text). The average numbers of outermost Au atoms per cluster were calculated from the size of the Au SSP. The ratio of Br to Au from Fig. 3 was used to determine the average number of Br atoms per cluster and the Br surface coverage.

It has been shown that the nanoclusters' catalytic activity is a function of cluster

size with a maximum at a particular diameter [61, 63]. For example, Choudhary *et al*.

found that Au nanoclusters on TiO_2 with an average diameter of 3.2 nm on TiO_2 produce

the highest turnover frequency for the CO oxidation reaction [65]. Many ideas have been proposed to explain the catalytic activity of metal nanoclusters, but there is not a complete consensus among researchers that would accompany a full understanding of the underlying mechanisms [66-68]. For example, the charge state of the supported nanoclusters and the involvement of that charge in surface reactions are still under debate [61, 63].

The first step in a catalytic reaction is the adsorption of a precursor molecule onto a surface, such as CO adsorbing onto Au nanoclusters in the oxidation reaction, which has been extensively studied [64, 65, 69, 70]. Since it is likely that Br adatoms occupy the same sites when adsorbed on a nanocluster, it can be concluded that halogens poison nanocatalysts by blocking the active sites. Furthermore, it can be inferred the mechanisms responsible for the adsorption of the precursors and the poisons are similar and thus have comparable saturation coverages [71].

Poisoning can occur by a physical blockage preventing adsorption of the precursor molecule which can entail electronic modification of the nearest neighbor atoms by that adsorbate, restructuring of the adsorbent surface, or hindering of surface diffusion of the adsorbed reactants [72]. Zhu *et al.* tested the reactivity of Pt nanoclusters on TiO_2 by oxidizing formaldehyde both before and after exposure to halogens [6]. From testing of formaldehyde oxidation using Pt nanoclusters as a catalyst, they found that any of the four halogens causes the performance of the nanocatalyst to worsen. In addition Gracia *et al.* demonstrated the deactivation of Pt nanoclusters used for CO oxidation by Cl adsorption [73].

Br and CO have some similarities when adsorbing onto Au nanoclusters, as discussed above, making it reasonable to assume that the Br adsorbs at the edges of the nanoclusters. Once Br_2 is near enough to the edge of a nanocluster, it is possible that the positively charged edge atoms lead to a configuration of adsorbed Br atoms that is lower in energy than the Br_2 molecule, causing it to dissociate. This is analogous to the dissociative chemisorption of halogens on a solid surface, where charge is donated locally from the bonding atom to the halogen adatom to form a partially ionic bond [74]. Once a Br atom is near enough to the substrate it can gain an electron to form a filled shell negative ion with a charge of -1.0 e. Since the average charge of the edge atoms in a nanocluster on TiO_2 is calculated to be +0.4 e, it is possible that the Br ionically bonds in a bridge site between two edge atoms as the magnitude of the charge of two Au edge atoms is nearly equal to the magnitude of a single Br negative ion.

If the Br adatoms were to adsorb ionically, the reduction in the NF can be explained in terms of the LEP change induced by the adatoms. An additional downward dipole would be formed by the negative Br adatom and the positively charged Au edge atom, which would increase the LEP above the edge atoms and therefore decrease the neutralization probability of Na^+ when scattering from those edge atoms. Since the NF for the smaller clusters does not fully decrease to that of Au metal, the saturation Br coverage is not sufficient to cover every edge atom, consistent with the data in Table 1.

If the saturation coverage was determined solely by the availability of positive sites along the edge of the nanocluster, this would imply that the saturation coverage should correspond to one Br atom per two Au edge atoms. The actual ratios lie between

one Br per 3.0 and 5.5 Au edge atoms, however. This could be partially due to the fact that the 40 µA min exposures used for some of the data in Table 1 are below what is needed to obtain full saturation of Br. Because these exposures are so close to saturation, however, there is more likely an intrinsic limit to the coverage due to other effects. For example, repulsion between adsorbed neighboring Br negative ions could lead to a saturation coverage that is less than one Br atom per two Au edge atoms.

4.5 Conclusions

It is found that atomic Br readily adsorbs to small Au nanoclusters, implying that the Br-Br bond breaks because of the catalytic ability of the clusters. The Br atoms likely bond to the nanoclusters at the same sites as CO, which is at the positively charged edge atoms [21, 53, 58]. This suggests a dependence of the catalytic activity on both the edge atom charge and the nanocluster size [75]. It is further indicated that Br adsorbs onto the nanoclusters by forming an ionic bond with the edge atoms, causing a change in the LEP and a reduction in the NF for scattered Na^+. From previous chemical studies, the catalytic activity of the nanoclusters is known to be reduced by halogen adsorption [6, 73]. This is directly correlated with the addition of downward pointing dipoles due to the adsorbed Br ions that act to oppose the upward pointing dipoles generated by the positively charged edge atoms. This implies that the total charge associated with the individual Au edge atoms in each cluster plays a role in the first adsorption step of catalytic reactions. This work further suggests that the change in NF of scattered alkali ions with cluster size may be a good indicator of a nanocluster's possible catalytic activity.

125

Bibliography

[1] G.A. Somorjai, Y. Li, *Introduction to Surface Chemistry and Catalysis, Second Edition*, Wiley, Hoboken, NJ, 2010.

[2] Z. Huang, N. Geyer, P. Werner, J. de Boor, U. Gösele, Adv. Mater., **23** (2011) 285-308.

[3] H.F. Winters, J.W. Coburn, Surf. Sci. Rep., **14** (1992) 162-269.

[4] K.L. Choy, Prog. Mater Sci., **48** (2003) 57-170.

[5] M. Haruta, S. Tsubota, T. Kobayashi, H. Kageyama, M.J. Genet, B. Delmon, J. Catal., **144** (1993) 175-192.

[6] X. Zhu, B. Cheng, J. Yu, W. Ho, Appl. Surf. Sci., **364** (2016) 7.

[7] D.P. Smith, J. Appl. Phys., **38** (1967) 340-347.

[8] C.B. Weare, J.A. Yarmoff, Surf. Sci., **348** (1996) 359-369.

[9] G.A. Kimmel, B.H. Cooper, Phys. Rev. B, **48** (1993) 12164-12177.

[10] C.A. Keller, C.A. DiRubio, G.A. Kimmel, B.H. Cooper, Phys. Rev. Lett., **75** (1995) 1654-1657.

[11] H. Niehus, W. Heiland, E. Taglauer, Surf. Sci. Rep., **17** (1993) 91.

[12] J. Los, J.J.C. Geerlings, Phys. Rep., **190** (1990) 133-190.

[13] J.P. Gauyacq, A.G. Borisov, J. Phys.: Condens. Matter, **10** (1998) 6585-6619.

[14] C.B. Weare, J.A. Yarmoff, J. Vac. Sci. Technol. A, **13** (1995) 1421-1425.

[15] A.R. Canário, V.A. Esaulov, J. Chem. Phys., **124** (2006) 224710.

[16] G.F. Liu, Z. Sroubek, J.A. Yarmoff, Phys. Rev. Lett., **92** (2004) 216801.

[17] A.B. Arjad, J.A. Yarmoff, Phys. Chem. C, **116** (2012) 23377-23382.

[18] S. Balaz, J.A. Yarmoff, Surf. Sci., **605** (2011) 675-680.

[19] J. Shen, J. Jia, K. Bobrov, L. Guillemot, V.A. Esaulov, Gold Bull., **46** (2013) 343-347.

[20] J. Shen, J. Jia, K. Bobrov, L. Guillemot, V.A. Esaulov, J. Phys. Chem. C, **119** (2015) 15168-15176.

[21] C. Salvo, P. Karmakar, J. Yarmoff, to be published.

[22] C. Lemire, R. Meyer, S. Shaikhutdinov, H.J. Freund, Angew. Chem. Int. Ed., **43** (2004) 118-121.

[23] M. Tanaka, K. Shudo, M. Numata, Phys. Rev. B, **73** (2006).

[24] K. Takayanagi, Y. Tanishiro, M. Takahashi, S. Takahashi, J. Vac. Sci. Technol. A, **3** (1985) 1502.

[25] Y. Yang, J.A. Yarmoff, Surf. Sci., **573** (2004) 335-345.

[26] R. Tromp, G.W. Rubloff, P. Balk, F.K. LeGoues, E.J. van Loenen, Phys. Rev. Lett., **55** (1985) 2332-2335.

[27] L. Zhang, F. Cosandey, R. Persaud, T.E. Madey, Surf. Sci., **439** (1999) 73-85.

[28] P.R. Varekamp, M.C. Håkansson, J. Kanski, D.K. Shuh, M. Björkqvist, M. Gothelid, W.C. Simpson, U.O. Karlsson, J.A. Yarmoff, Phys. Rev. B, **54** (1996) 2101-2113.

[29] N.D. Spencer, P.J. Goddard, P.W. Davies, M. Kitson, R.M. Lambert, J. Vac. Sci. Technol. A, **1** (1983) 1554-1555.

[30] W.K. Wang, W.C. Simpson, J.A. Yarmoff, Phys. Rev. Lett., **81** (1998) 1465-1468.

[31] R.S. Gao, P.S. Gibner, J.H. Newman, K.A. Smith, R.F. Stebbings, Rev. Sci. Instrum., **55** (1984) 1756-1759.

[32] M.J. Bedzyk, W.M. Gibson, J.A. Golovchenko, J. Vac. Sci. Technol., **20** (1982) 634-637.

[33] B.K. Min, W.T. Wallace, A.K. Santra, D.W. Goodman, J. Phys. Chem. B, **108** (2004) 16339-16343.

[34] C.S. Chang, U. Knipping, I.S.T. Tsong, Nucl. Instrum. Methods B, **18** (1986) 11-15.

[35] O.S. Oen, Surf. Sci., **131** (1983) 407-411.

[36] W.J. Rabalais, Principles and applications of ion scattering spectrometry : surface chemical and structural analysis, Wiley, New York, 2003.

[37] R.G. Jones, Prog. Surf. Sci., **27** (1988) 25-160.

[38] T. Wandlowski, J.X. Wang, O.M. Magnussen, B.M. Ocko, J. Phys. Chem., **100** (1996) 10277-10287.

[39] E. Bertel, F.F. Netzer, Surf. Sci., **97** (1980) 409-424.

[40] Z.V. Zheleva, V.R. Dhanak, G. Held, Phys. Chem. Chem. Phys., **12** (2010) 10754-10758.

[41] S.A. Cochran, H.H. Farrell, Surf. Sci., **95** (1980) 359-366.

[42] E.S. Parilis, L.M. Kishinevsky, N.Y. Turaev, B.E. Baklitzky, F.F. Umarov, V.K. Verleger, S.L. Nizhnaya, I.S. Bitensky, *Atomic Collisions on Solid Surfaces*, North-Holland, Amsterdam, (1993).

[43] X. Lai, T.P.S. Clair, M. Valden, D.W. Goodman, Prog. Surf. Sci., **59** (1998) 25-52.

[44] P. Nordlander, J.C. Tully, Phys. Rev. B, **42** (1990) 5564-5578.

[45] R.D. Gann, J.X. Cao, R.Q. Wu, J. Wen, Z. Xu, G.D. Gu, J.A. Yarmoff, Phys. Rev. B, **81** (2010) 035418.

[46] G.A. Kimmel, B.H. Cooper, Phys. Rev. B, **48** (1993) 12164-12177.

[47] A.G. Borisov, D. Teillet-Billy, J.P. Gauyacq, H. Winter, G. Dierkes, Phys. Rev. B, **54** (1996) 17166-17174.

[48] C.B. Weare, K.A.H. German, J.A. Yarmoff, Phys. Rev. B, **52** (1995) 2066-2069.

[49] Z. Zhang, W. Tang, M. Neurock, J.T. Yates Jr., J. Phys. Chem. C, **115** (2011) 23848-23853.

[50] T. Okazawa, M. Fujiwara, T. Nishimura, T. Akita, M. Kohyama, Y. Kido, Surf. Sci., **600** (2006) 1331-1338.

[51] A. Visikovskiy, H. Matsumoto, K. Mitsuhara, T. Nakada, T. Akita, Y. Kido, Phys. Rev. B, **83** (2011) 165428.

[52] C. Zhang, A. Michaelides, D.A. King, S.J. Jenkins, J. Am. Chem. Soc., **132** (2010) 2175-2182.

[53] L.B. Vilhelmsen, B. Hammer, ACS Catalysis, **4** (2014) 1626-1631.

[54] W. Zhong, D. Zhang, Prog. React. Kinet. Mech, **38** (2013) 86-94.

[55] A. Sanchez, S. Abbet, U. Heiz, W.D. Schneider, H. Hakkinen, R.N. Barnett, U. Landman, J. Phys. Chem. A, **103** (1999) 9573-9578.

[56] X. Yu, L. Xu, W. Zhang, Z. Jiang, J. Zhu, W. Huang, Chin. J. Chem. Phys., **22** (2009) 339-345.

[57] M. Valden, X. Lai, D.W. Goodman, Science, **281** (1998) 1647-1650.

[58] S. Hong, T.S. Rahman, J. Am. Chem. Soc., **135** (2013) 7629-7635.

[59] B.K. Min, W.T. Wallace, D.W. Goodman, Surf. Sci., **600** (2006) L7-L11.

[60] Y.-G. Wang, D.C. Cantu, M.-S. Lee, J. Li, V.-A. Glezakou, R. Rousseau, J. Am. Chem. Soc., **138** (2016) 10467-10476.

[61] B. Roldan Cuenya, F. Behafarid, Surf. Sci. Rep., **70** (2015) 135-187.

[62] M.J. Walsh, P.L. Gai, E.E. Boyes, J. Phys. Conf. Ser., **371** (2012) 1-4.

[63] S. Arrii, F. Morfin, A.J. Renouprez, J.L. Rousset, J. Am. Chem. Soc., **126** (2004) 1199-1205.

[64] C. Lemire, R. Meyer, S.K. Shaikhutdinov, H.J. Freund, Surf. Sci., **552** (2004) 27-34.

[65] T.V. Choudhary, D.W. Goodman, Top. Catal., **21** (2002) 25-34.

[66] M. Flytzani-Stephanopoulos, Acc. Chem. Res., **47** (2014) 783-792.

[67] T. Risse, S. Shaikhutdinov, N. Nilius, M. Sterrer, H.J. Freund, Acc. Chem. Res., **41** (2008) 8.

[68] N. Nilius, T. Risse, S. Shaikhutdinov, M. Sterrer, H.J. Freund, **162** (2013) 91-138.

[69] V.A. Bondzie, S.C. Parker, C.T. Campbell, Catal. Lett., **63** (1999) 143–151.

[70] S.K. Shaikhutdinov, R. Meyer, M. Naschitzki, M. Bäumer, H.-J. Freund, Catal. Lett., **86** (2003) 211-219.

[71] P.C. Mørk, D. Norgård, J. Am. Oil Chem. Soc., **53** (1976) 506-510.

[72] C.H. Bartholomew, App. Catal. A: General, **212** (2001) 17-60.

[73] F.J. Gracia, J.T. Miller, A.J. Kropf, E.E. Wolf, J. Catal., **209** (2002) 341-354.

[74] L.G.M. Pettersson, P.S. Bagus, Phys. Rev. Lett., **56** (1986) 500-503.

[75] B.K. Min, X.Y. Deng, X.Y. Li, C.M. Friend, A.R. Alemozafar, Chemcatchem, **1** (2009) 116-121.